Norwegian University
of Life Sciences

**Master's Thesis 2019    30 ECTS**
Faculty of Science and Technology

# Hyperspectral Photoluminescence of Thermal Donors in two Czochralski Crystals Pulled at Different Velocities

Helene Eikaas Stalheim

Master of Science in Technology:
Environmental Physics and Renewable Energy

# Acknowledgements

With this master thesis I complete my degree in Master of Science in Technology: Environmental Physics and Renewable Energy at the Norwegian University of Life Sciences (NMBU). This work is a part of the Research Center for Sustainable Solar Cell Technology (FME Susoltech), sponsored by the Research Council of Norway. FME Susoltech is hosted by the Institute for Energy Technology (IFE), where NMBU is one of the partners.

I would like to thank my main supervisor associate professor Ingunn Burud for the good assistance and motivation during this work. I want to thank her for introducing me to the exciting field of hyperspectral imaging. I wish to express my thanks to my co-supervisor professor Espen Olsen who inspired me during the solar energy course and shared his great knowledge regarding the topics of my work. I thank postdoctoral fellow Torbjørn Mehl for helping me with the hyperspectral imaging setup and guidance related to the experimental work. I would like to thank Ph.D. candidate Marija Vukovic for useful advice regarding the data analysis. I have appreciated the weekly meetings with Ingunn, Espen, Torbjørn, Marija and the other master students.

I wish to express my great appreciation to senior scientist Rune Søndenå for welcoming me at IFE and for doing the etching and thermal annealing of the samples. I am grateful for his suggestions and the invaluable help with discussion related to my experimental results as well as the thesis outline.

I thank senior research scientist Mari Juel at SINTEF for providing me with the samples from PVA Tepla along with the oxygen and resistivity measurements. I am thankful for useful discussions on my results.

Further, I would like to give a big thank you to my parents Ingvei and Jostein for the continuous support during my studies. Last but not least, I thank my boyfriend Julius for his positive encouragement, care and proofreading through the last phase of this work.

Helene Eikaas Stalheim
Ås, May 14th, 2019

# Abstract

This study has shown that hyperspectral photoluminescence (HSPL) imaging may be used for connecting defect-related luminescence (DRL) signals to electrically active oxygen clusters of thermal donors (TDs). Thus, by using the fast and non-destructive method of HSPL imaging at an early stage of production may increase the yield of the Czochralski silicon (CZ-Si) material. The scanned vertical cross-section samples were extracted from two CZ-Si crystals pulled at different velocities. The crystal with the highest pull speed has been concluded to be cleanest with best outlooks for commercial use. The HSPL images show dominant DRL signals for the low pull speed crystal. The highest $[O_i]$ is found close to the seed end of the crystal, and it corresponds well with the strongest DRL signal detected at $0.767\,$eV, commonly known as the P-line. A spatial vacancy-interstitial dominating transition area has been observed for samples near the seed end. The transition area is concluded to be a denuded area, free of impurities. After the $450\,°$C heat treatment, the main emission lines for TD-dominated samples were $0.704\,$eV, $0.725\,$eV, $0.749\,$eV, the P-line, $0.789\,$eV (C-line) and $0.925\,$eV (H-line). The strongest DRL signals for TD-dominated samples are uniformly distributed as a function of crystal height. A statistical technique called Multivariate Curve Resolution is used within the Python environment to support the findings of the DRL signals. After the heat treatment at $650\,°$C, the band-to-band signal at 1.12 eV is greatly enhanced, at most for the high pull speed crystal with the lowest $[O_i]$. The seven DRL emission lines from $0.68\,$eV to $0.79\,$eV are replaced with one continuous broad P-line signal. The P-line is connected to TDs, but one hour of thermal annealing may have been too short for TD elimination. In order to confirm this hypothesis, further investigations would be natural to do with different time intervals of the $650\,°$C heat treatment.

# Sammendrag

Dette studiet har vist at hyperspektral fotoluminescens (HSPL) avbildning utgjør en metode for å knytte defektrelatert luminescens (DRL) signaler til elektriske aktive oksygensentre av termiske donorer (TDer). Derfor, ved å identifisere TDer i Czochralski silisium (CZ-Si) materiale ved hjelp av den raske og ikke-destruktive HSPL avbildningsmetoden ved et tidlig produksjonssteg, kan utbyttet fra den ferdige solcellen øke. De avbildede prøvene er vertikale skiver fra to CZ-Si krystaller med forskjellig trekkhastighet. Krystallen med høyest trekkhastighet fremstår som renest grunnet reduserte DRL signaler og dermed best til å benyttes i kommersiell bruk. Høyest $[O_i]$ er funnet sammen med DRL-signalet ved 0.767 eV (P-linje) nær toppen av krystallene. På samme område er det observert et romlig vakanse-interstitielldominert overgangsområde. Overgangsområdet er konkludert til å være fri for urenheter. Etter 450 °C varmebehandling ble DRL-linjene for TD-dominerte prøver observert ved 0.704 eV, 0.725 eV, 0.749 eV, P-linjen, 0.789 eV (C-linje) og 0.925 eV (H-linje). DRL-signalene for TD-dominerte prøver er uniformt fordelt som funksjon av krystallhøyde. En statistisk metode kalt Multivariate Curve Resolution er benyttet i Python programmeringsspråk for å bekrefte funnene knyttet til DRL-signaler. Etter TD-elimineringsbehandling ved 650 °C var bånd-til-bånd signalet ved 1.12 eV kraftigst for krystallen med høyest trekkhastighet. DRL-emisjonslinjene fra 0.68 eV til 0.79 eV er erstattet med ett kontinuerlig bredt P-linje signal som toppunkt for etsede prøver. P-linjen er konkludert til å være knyttet til TDer, men varmebehandling på én time kan ha vært for kort tid for å eliminere alle TDer. For å bekrefte denne hypotesen, vil det være naturlig å utføre flere 650 °C varmebehandlinger med forskjellige tidsintervaller.

# Contents

# Nomenclature

**Abbreviations**

ALS    **A**lternating **L**east **S**quares

BB     **B**and-to-**B**and

CB     **C**onduction **B**and

CCD   **C**harge **C**oupled **D**evice

CL      **C**athodo**l**uminescence

CZ      **Cz**ochralski

DI      **D**e-**i**onized

DRL   **D**efect-**r**elated **L**uminescence

eeh     **E**lectron **e**lectron **h**ole

ehh     **E**lectron **h**ole **h**ole

EL      **E**lectro**l**uminescence

FTIR   **F**ourier **T**ransform **I**nfra**r**ed

FZ      **F**loat **Z**one

HSPL   **H**yper**s**pectral **P**hoto**l**uminescence

IFE     **I**nstitute **f**or **E**nergy Technology

mc-Si   **M**ulti**c**rystalline **Si**licon

MCR   **M**ultivariate **C**urve **R**esolution

MGS   **M**etallurgical-**G**rade **S**ilicon

mono c-Si **Monoc**rystalline **Si**licon

NIR    **N**ear **I**nf**r**a**r**ed

NMBU The Norwegian University of Life sciences

O      **O**xygen

PL     **P**hoto**l**uminescence

PV     **P**hoto**V**oltaic

Si     **Si**licon

SRH    **S**hockley **R**ead **H**all

SWIR   **S**hort **W**avelength **I**nf**r**a**r**ed

TD     **T**hermal **D**onor

VB     **V**alence **B**and

**Constants**

$h = \hbar \times 2\pi$ Planck constant                          $6.626 \times 10^{-34}$ Js

$k$       Boltzmann constant                          $1.38 \times 10^{-23}$ J/K

$q$       Elementary charge                          $1.602 \times 10^{-19}$ C

**Operators**

$\Delta$      Difference

$\partial$      Partial derivative

**Sub- and superscripts**

$_0$       Thermal equilibrium

$_A$       Acceptor

$_C$       Conduction

$_D$       Donor

$_d$       Direct/Radiative

| | |
|---|---|
| $ed$ | Electron, direct |
| $e$ | Electron |
| $F$ | Fermi |
| $G$ | Bandgap |
| $hd$ | Hole, direct |
| $i$ | Intrinsic/interstitial |
| $p$ | Parallel |
| $sc$ | Short circuit |
| $s$ | Series |
| $th$ | Thermal |
| $T$ | Trap |
| $V$ | Valence |

**Variables**

| | |
|---|---|
| $\beta$ | Proportionality factor in radiative recombination |
| $\epsilon$ | Emission coefficient |
| $\gamma$ | Photon |
| $\lambda$ | Wavelength |
| $\nu$ | Photon frequency |
| $\sigma$ | Capture cross-section of charge carriers |
| $\tau$ | Minority charge carrier lifetime |
| $\mathbf{R}$ | Resistance |
| $\theta$ | Deflection angle |
| $C$ | Proportionality factor in Auger recombination |
| $c$ | Capture coefficient |

| | |
|---|---|
| $D$ | Diffusion coefficient |
| $d$ | Distance |
| $E$ | Energy |
| $e^-$ | Electron |
| $F$ | Free energy |
| $f$ | Fermi-Dirac distribution |
| $G$ | Generation rate |
| $h^+$ | Hole |
| $I$ | Electric current |
| $m$ | Diffraction coefficient |
| $N$ | Effective density state |
| $n$ | Concentration of electrons |
| $p$ | Concentration of holes |
| $R$ | Recombination rate |
| $r$ | Reaction |
| $S$ | Entropy |
| $T$ | Temperature |
| $t$ | Time |
| $V$ | Voltage |
| $v$ | Velocity of charge carriers |
| $\mathbf{p}$ | Crystal momentum |

# Chapter 1

# Introduction

## 1.1 Motivation

Solar energy is the most abundant renewable energy source accessible on Earth. The development of exploiting solar energy has been large over the past recent decades. It is a better alternative in generating electricity compared to fossil fuels, considering air and water pollution, global warming and threat to human health. Mankind needs a continuously increasing amount of energy, and electrical energy has shown to be one of the most useful energy forms.

There are three main solar energy technologies developed today. The first is concentrated solar power, which uses thermal energy from the sun to drive electric turbines. The second is heating and cooling systems which collect heat to provide hot and air conditioning water. The third technology is photovoltaic (PV) and will be the focus of this thesis. This technology converts radiative energy from the sun directly into electricity. PV systems consist of several solar cells and can be positioned through distributed generation, with the equipment placed on large fields or on rooftops close to the electricity-dependent location. The advantage with a PV system is that it does not contain any moving parts and it generally lasts for about thirty years with little maintenance work.

Cost and performance are the two most important factors when developing a PV system. The factors may be affected by the fabrication of solar cells, and by the application and configuration of the panel once installed. An important task for today's researches worldwide is to balance a reduced cost and improved energy conversion efficiency. In this way, solar cells may become price-competitive with other energy forms. In the current work, the growth process used for the mono-crystalline silicon crystals is called the Czochralski (CZ) method. If the CZ crystals are pulled at a faster velocity, the defects related to the production of solar cells can potentially be reduced. However, the overall cost must not be affected by the defect reduction. A PV system lasts for several decades, and a small increase in cost will be accumulated into giving a large impact on profitability.

It was found in 1956 that by heating oxygen-rich silicon up to 450 °C, electrical active defects were generated [26], later called thermal donors (TDs). Since then, numerous researchers have been trying to elucidate the detailed behavior of TDs. Sixty years later, the details of the processes by which the defects are generated and eliminated are still obscure. In the present work, the effect of TDs will be studied as a function of the height of two crystals pulled at different velocities. This will be carried out by hyperspectral photoluminescence (HSPL) imaging of etched and unetched Czochralski silicon (CZ-Si) cross-section samples. The samples are HSPL scanned before and after thermal annealing at 450 °C and at 650 °C.

In order to have an understanding of the oxygen in the CZ-Si material before entering the expensive process of high-efficiency solar cells, it is necessary to elucidate the TD formation for the material. HSPL measurements of CZ-Si cross-section samples may constitute an appropriate method for the characterization of TDs. The oxygen incorporation mechanisms and their interactions during processing are important to understand for uniformly distribute oxygen at the desired level during the CZ process. This can, in turn, lead to an increased yield of the CZ-Si material.

## 1.2   Aims for this work

The objectives of this work are to connect the oxygen-related TDs with the defect-related luminescence (DRL) signals and to detect the associated spatial distribution in the CZ-Si crystal. The difference in DRL signals between the two crystals will be clarified. The HSPL imaging method will be explored for studying thick vertical cross-sections, and the scanning performed at room temperature and at cryogenic conditions will be compared. Some of the samples have gone through a wet-chemical etching process, and the effects of this related to HSPL imaging will be discussed.

## 1.3   Thesis outline

The thesis is structured as follows: A brief introduction with motivation and aims of this research. Chapter 2 presents the theoretical part with some important concepts. This is followed by chapter 3 presenting literature studies. Next, the method and materials are presented, followed by the data analysis part. Chapter 6 contains the results and respective discussions. The final chapter contains the conclusions together with suggestions for further work.

# Chapter 2

# Theoretical Background

This chapter gives an insight into the theoretical background on which the experimental part, discussion, and conclusions are based. The theoretical background is divided into five parts. First, an introduction to the basics of semiconductor physics is given. This is followed by the production process of mono-crystalline silicon solar cells, with the Czochralski process in focus. Generation and recombination of excess charge carriers are explained in the third part, followed by different types of defects that can occur in CZ-Si crystals. Lastly, the theory of luminescence is explained, with a focus on hyperspectral photoluminescence imaging.

## 2.1 Basics of semiconductor physics

Solar cells generate electricity using the electronic properties of materials known as semiconductors. The semiconductor material used for in solar cells is divided into two layers with opposite charges [20]. When the sun is shining on the solar panels, electrons in the material are excited from their initial position to a higher energy level position. The electrons flow from the negative (n-type) layer of the material to the positive (p-type) part. With an external circuit, there is an open path for electrons in the n-type layer to be excited to the p-type layer. The opposite process happens for holes, and this will create a charge imbalance in both n-type and p-type regions. These exposed charges will set up an electric field between themselves, which will oppose the diffusion tendency of electrons. As electrons flow through the cell and the external circuit connected to the panel, they generate an electrical current. This was discovered in 1839 by Edmond Becquerel when he observed that certain materials give off sparks when struck by photons [9].

Electrons in a single silicon atom can possess different discrete energy levels. The distribution of the electrons in a solid material must fulfill three conditions [69]:

1. Pauli exclusion principle explains that there can never be more than one electron/proton (with spin 1/2) in the same quantum state.

2. The occupation of a state is only energy dependent and not affected by momentum.

3. The minimum energy of the occupied state is expressed as $E = F - TS$.

The energy is expressed as $E$, the free energy as $F$, the temperature is $T$, and the entropy is denoted $S$. As a result of the Pauli exclusion principle, the closely separated atoms give rise to two allowed energy bands that differ energy amount. The band with the lowest energy is called the valence band (VB), with energy $E_V$. The highest energy band is called the conduction band (CB), with energy $E_C$. The energy band in between the VB and the CB is called the bandgap, with energy, $E_G$, see Figure 2.1. The bandgap energy describes the conductive properties of the semiconductor material [2].
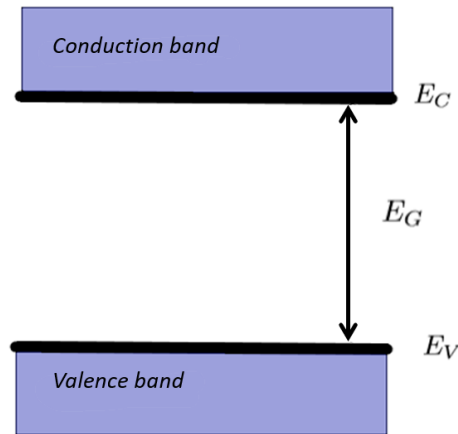


Figure 2.1: The allowed energy states for an atom. The bandgap energy $E_G$ is the difference between the conduction energy $E_C$ and the valence energy $E_V$. Adapted from: Smets et al. 2016 [2].

At temperatures approaching $0\,\mathrm{K}$, all electrons in the atom are found in the minimum energy state (VB). All temperatures above $0\,\mathrm{K}$ involve breaking a bond due to the absorption of thermal energy [2]. This leads to electrons $e^-$ leaving their place to move freely within the lattice, and thereby leave holes $h^+$ behind, i.e. positive charges representing the empty position. As electrons get excited with a rising temperature above $0\,\mathrm{K}$, the energy $E$ and entropy $S$ in condition number three both increase, while the free energy $F$ decreases [69].

### 2.1.1 Crystalline silicon

Silicon (Si) is the second most spread out chemical element on Earth's crust and is well suited for PV technology. Nowadays, 90% of all solar cells fabricated are made by crystalline silicon [45]. Si of high purity is a semiconductor material which has a crystalline lattice structure [2]. Si is a chemical element of group XIV in the periodic system. The atom consists of 14 electrons in its three shells surrounding the nucleus, which gives silicon the form of a tetravalent metalloid. Thus, Si has four electrons in the outer shell, the so-called valence electrons. The Si atom can form a covalent bond to four other Si atoms.

From nature, silicon appears connected with oxygen and other chemical compounds, resulting in silicates [2]. Silicon dioxide, $SiO_2$, also known as silica, can be found in sand and this is known as the main extraction source of silicon [20].

### 2.1.2 Intrinsic semiconductor

Intrinsic semiconductors are undoped, which means that the thermal excitation of electrons only can happen from the VB to the CB [45]. Hence, the density of electrons ($n_0$) in the CB equals the density of holes ($p_0$) in VB. Their common value, the intrinsic charge carrier concentration, is defined as $n_i = p_0 = n_0$ [2].

According to the Pauli exclusion principle, the Fermi-Dirac distribution function denotes the occupation probability of the allowed electron energies, $E_e$, and is expressed in equation 2.1 [14], [10].

$$f_e(E_e) = \frac{1}{\exp\left[(E_e - E_F)/kT\right] + 1}.$$  (2.1)

In Eq. 2.1, $T$ is the absolute temperature and $k$ denotes Boltzmann's constant. The Fermi energy $E_F$ is defined as the difference between the highest and lowest occupied energy state of a particle at $T \approx 0\,K$ in an intrinsic material. The expression often used in semiconductor physics is the Fermi level, which denotes the energy level of the highest occupied particle state for any temperature [69]. As the temperature increases, the Fermi-Dirac distribution shows that energies above $E_F$ have a finite probability of occupation, whereas energies below $E_F$ have a finite probability of being empty of charge carriers [20].

According to Boltzmann approximation, the Fermi-Dirac notation can be abbreviated into $f_e(E_e) \approx \exp\left[-(E_e - E_F)/kT\right]$ when $(E_e - E_F) \gg 3kT$. From this, the $n_0$ and $p_0$ can be expressed in equation 2.2 and 2.3, respectively [45].

$$p_0 = N_V \exp\left(-\frac{E_F - E_V}{kT}\right),$$  (2.2)

$$n_0 = N_C \exp\left(-\frac{E_C - E_F}{kT}\right),$$  (2.3)

where $N_V$ and $N_C$ describe the effective density state of the VB and the CB, respectively [45]. The independent position of the Fermi level can be found by multiplying Eqs. 2.2 and 2.3:

$$n_0 p_0 = n_i^2 = N_C N_V \exp\left(\frac{E_V - E_C}{kT}\right) = N_C N_V \exp\left(-\frac{E_G}{kT}\right). \tag{2.4}$$

The Fermi level in the intrinsic semiconductor $E_{F,i}$ lies close to the midgap of silicon, as shown in equation 2.5.

$$E_{F,i} = \frac{E_C - E_V}{2} + \frac{kT}{2} \ln \frac{N_V}{N_C} = E_C - \frac{E_G}{2} + \frac{kT}{2} \ln \frac{N_V}{N_C}. \tag{2.5}$$

### 2.1.3   Extrinsic semiconductor

In the case of an extrinsic semiconductor, impurity atoms from other chemical elements are intentionally added to the crystal structure to improve the conductivity [2]. This is referred to as doping, and these atoms replace the silicon atoms of the semiconductor at their lattice site. The concentration of holes in the VB and the concentration of electrons in the CB are not of the same size. Hence, the Fermi level is slightly shifted towards either of the bands, depending on how the material is doped. Silicon is not a very good electrically conductor on its own, but when other chemical elements are added to the silicon during the growth of a crystal, the efficiency of creating electrical current increases.

In an n-type material, some of the silicon atoms in the lattice are replaced by impurity atoms of group XV (such as phosphorus). The fifth valence electron in a phosphorus atom does not form covalent bonds with other electrons, but is rather weakly bound to the atom and can easily escape. Therefore, the Fermi level is situated close to the CB, where the energy of the liberated electron is found. Holes are denoted as minority charge carrier concentration in the n-type material and is expressed in Eq. 2.6. For further interest, the derivation of Eq. 2.6 can be found in Appendix B.

$$p = \frac{n_i^2}{n} \approx \frac{n_i^2}{N_D} \ll n, \tag{2.6}$$

where $N_D$ denotes the effective density state of donors. Donors have thereby more valence electrons than is necessary for chemical bonding with adjacent atoms [69]. According to Coulomb law, a donor is electrically bound to its atom by Coulomb forces in the vacuum. However, in a semiconductor, the electric field bounding is weakened by the polarization of neighboring atoms. Therefore, electrons donate easily to the conduction band, as a result of the weak Coulomb bond [69].

In the case of p-type material, a chemical element from group XIII, e.g. boron, is added. Boron impurity atoms are acceptors that have one valence electron less than the rest of the atoms in the semiconductor lattice. The atom has a missing Coulomb bond, and the electron

filling the hole does not have an attraction to the impurity atom. Therefore, the acceptor atoms easily accept an electron from the valence band and introduce an allowed Fermi level close to the VB [69]. The minority charge carrier concentration, $n$, can be expressed as in equation 2.7.

$$n = \frac{n_i^2}{p} \approx \frac{n_i^2}{N_A} \ll p,$$
(2.7)

where $N_A$ is the concentration of acceptors in the material. The derivation of Eq. 2.7 is the same as for Eq. 2.6, found in Appendix B.

By contaminating the crystalline silicon structure with donor or acceptor atoms, additional Fermi levels in the bandgap are introduced. Equilibrium will thus be achieved for a p-n junction [20]. Eqs. 2.2 and 2.3 also apply for a doped semiconductor and expressions for Fermi level can thus be derived for n-type in Eq. 2.8 and for p-type in Eq. 2.9:

$$E_C - E_F = kT \ln \frac{N_C}{N_D},$$
(2.8)

$$E_F - E_V = kT \ln \frac{N_V}{N_A}.$$
(2.9)

## 2.2 Production of mono-crystalline silicon solar cells

Production of mono-crystalline silicon (mono c-Si) solar cells consists of complex and expensive techniques. Mono-crystalline differs from multi-crystalline in a way that there is a single crystalline solid within the continuous crystal lattice, instead of various crystal grains with mismatches and different orientations [2]. As a result, multi-crystalline material contains more defects and the charge carrier lifetime is much shorter than for mono-crystalline material. The silicon goes through many steps to remove most of the impurities and to increase the resulting efficiency of the solar cell material [2]. The standard technology of fabricating mono c-Si solar cells will be given in this section, to provide a base for discussing improvements in the production steps for the future.

### 2.2.1 Quartz to metallurgical-grade silicon

Silica $SiO_2$ is chemically extracted in sands and quartz, by using carbon. This results in metallurgical-grade silicon (MGS), i.e. 98 % low purity silicon. MGS is the first step of creating semiconductor-grade, single crystal silicon that can be used in a commercial context. Silica is reduced in arc furnaces to produce silicon according to reaction 2.10.

$$SiO_2 + 2\,C \rightarrow Si + 2\,CO$$
(2.10)

Silicon is poured from the furnace and blown with oxygen to higher the purity [20]. This is followed by pouring the silicon through shallow troughs, to solidify it and break it into chunks.

### 2.2.2 Metallurgical-grade silicon to semiconductor-grade silicon

To obtain higher purity to use as a semiconductor material, the MGS chunks are mixed with hydrogen chloride (HCl) which results in trichlorosilane ($HSiCl_3$) [13], according to reaction 2.11.

$$Si + 3\,HCl \rightarrow HSiCl_3 + H_2 \tag{2.11}$$

This process is called the Siemens process, where silicon of extremely high purity can be extracted [20]. Reaction 2.11 happens at high temperature in a reaction chamber, usually between $900\,°C$ to $1100\,°C$ [13]. The MGS is converted into a volatile compound that is condensed and distilled. Through distillation, impurities with a boiling point that differs from the one for $HSiCl_3$, are removed. This is followed by evaporation of the $HSiCl_3$ in another reactor, as well as mixing with hydrogen gas [2], according to reaction 2.12.

$$HSiCl_3 + H_2 \rightarrow Si + 3\,HCl \tag{2.12}$$

$HSiCl_3$ is decomposed into hot rods of pure Si. The heated rod works as a nucleation point for the deposition of silicon, and it is, therefore, crucial to maintain the correct temperature during the reaction. The Siemens process leads to a decrease in the rod's resistance, and it is thus simpler to keep the desired elevated temperature inside the chamber [13]. The Si atoms are deposited on the rod, whereas other atoms such as chlorine and hydrogen are evaporated back into the gas phase. The chlorine and the hydrogen are subsequently cleaned and reused in the reaction chamber [2].

Mono c-Si is obtained, and this part of the process is very energy demanding, which explains why mono c-Si has a much more expensive production process than mc-Si material [13]. The Siemens process has got a low yield at about 37% [20].

### 2.2.3 Semiconductor-grade silicon to single-crystal wafers

When the silicon is deposited on an electrically heated silicon rod, it results in many silicon pieces. To obtain single-crystal wafers, there are two main methods that can be used. The methods are the Czochralski (CZ) and the float zone (FZ) process [20]. The two techniques vary in cost and slightly in purity [13].

The FZ method is based on a zone-melting process and was invented by Theuerer in 1962 [60]. The FZ silicon can easily achieve higher purity and resistivity (ranges from few tens to thousands $\Omega$cm) than for CZ silicon (resistivity usually lower than $50\,\Omega$cm) [31]. The oxygen level is also significantly lower in FZ silicon than in CZ silicon, with a concentration of $10 \times 10^{16}$ atoms/cm$^3$, one to two orders of magnitude lower than in CZ silicon [31]. The FZ process is out of the scope of this work and can be read more about in *Solar Energy, The Physics and Engineering of Photovoltaic conversion, technologies, and systems* by Smets et al. [2].

Since the residual level of oxygen is lower than that of silicon, it can lead to lower mechanical strength in terms of withstanding thermal stress and suppress slips. Oxygen is sometimes added intentionally by increasing the melt-crucible contact surface [31]. The presence of interstitial oxygen in the silicon lattice can enhance the strength of bonds between the atoms and it has a hardening effect on the lattice. This can prevent plastic deformation and slip for further fabrication steps, as well as obstacles for dislocation initiation and generation [31]. For the most part, oxygen causes defects in the c-Si material, which will be presented in section 2.4. Since oxygen can have positive and negative consequences for the final material, it is essential to have an understanding of the process thermal sequence and matching the oxygen level in CZ-Si material [31]. As CZ-Si cross-sections are used in this study, the CZ process will be presented below.

The Czochralski method was invented in the years 1916-1924 by Jan Czochralski [63]. First, he invented a method for measuring the velocity of metal crystallization, and from this, he developed a technique for obtaining single crystals. In the CZ-Si process, highly purified silicon pieces along with the dopant are melted in a quartz crucible at a high temperature of $1500\,°C$. As explained in the previous subsection, boron or phosphorous can be added to make p-type or n-type material, respectively [2]. The dopant mixes well with the silicon, given the high temperature (the melting point of silicon is at $1412\,°C$) [13]. Once the melted silicon and the dopant are well mixed together, the temperature is stabilized at $1417\,°C$. A seed crystal is placed on a rod and dipped in a crucible of molten high-purity silicon. The rod is pulled upwards and rotates in the opposite direction of the crucible. This is done to minimize the effects of convection in the melt manufacturing of the single-crystal. A cylindrical crystal is extracted from the melt in an inert atmosphere, by controlled pressure, temperature and pull speed. Different pull speeds result in different qualities for the finished crystal. $80-90\%$ of the silicon single crystals used for integrated circuit fabrication are produced by the CZ process [13]. This is due to the CZ process' great ability to create large-diameter cylindrical crystals. Crystals of diameter $12.5\,cm$ and length $1\,m$ to $2\,m$ are routinely CZ-grown [20]. The components in the CZ crystal growth technique are the seed, single-crystal silicon, quartz crucible, water-cooled chamber, heat shield, carbon heater, graphite crucible, crucible support, spill tray, and electrodes [13].

The CZ process has its limitations, which are mainly due to impurities of other chemical elements in the resulting crystal. Oxygen and carbon are the two most usual compounds found in the silicon crystal after the growth process. The crucible containing the molten silicon is made by quartz and is, therefore, the main reason why oxygen takes place in the resulting crystal rod [13].

During the CZ process, several motions and forces are included. The fluid motion has its origin from the crystal and the crucible rotation, i.e. from forced convection [32]. The density differences are causing a buoyancy force, and shear surface stress is a result of the surface tension gradient. In the melt, heat is transferred by conduction and free convection. In the solid, the heat is only due to conduction. Eddy currents are found in a previous research by

Stefani et al. [53] to be related to the changing electrical conductivity of the crystal. The surface of the crystal will become hotter than the inside. Since the electrical conductivity of silicon is a function of temperature, it causes changes in conductivity through the resulting crystal.

The crystal used for further production steps is a cut part of the whole crystal body, as there are too many impurities in the outer parts. The top of the crystal, called the crown, consists of crystal defects, whereas the other tail end of the cylinder contains unintentional impurities. Hence, only the mid-part of the crystal can be used for integrated circuit fabrication, and the rest is wasted as kerf or cutting loss [13]. Silicon solar cells only need to be around $100\,\mu$m thick to be able to absorb photons from the sun [20]. The single silicon crystal is, therefore, cut into thin wafers.

## 2.2.4 Silicon single-crystal wafers to mono-crystalline solar cells

There are several processes for making solar cells from wafers. First, the wafers go through etching process where their optical and electrical properties are elevated by chemicals. The etching reduces the level of impurities from the sawing process. This is followed by doping the material and putting together a p- and n-type material, creating a p-n junction. This sets up an electric field between the two regions. Further, anti-reflective coating layers are added to reduce the reflection losses, and lastly, electrical contacts are added for completing the solar cell [20].

Figure 2.2 shows the equivalent circuit of a finished solar cell, extended with a diode of direct recombination. The shunt resistance in parallel $R_p$ represents the impurities near the p-n junction and the existence of alternate current pathways through the PV cell. It is desired to have $R_p$ as high as possible in order to keep the open circuit voltage high and prevent leakage current through these pathways. The series resistance $R_s$ shows the internal resistance that arises from energetic barriers, i.e. the losses of the solar cell. $R_s$ is desired to be kept as low as possible.
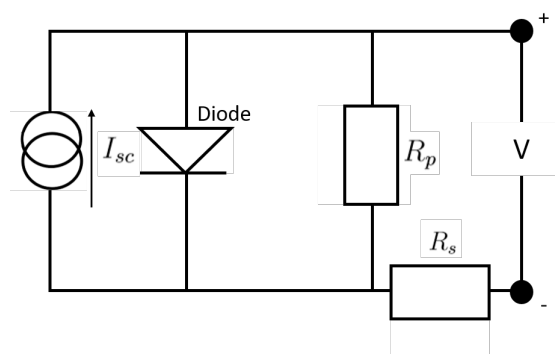


Figure 2.2: Equivalent circuit for a solar cell consisting of a diode with direct recombination, short circuit current $I_{sc}$, parallel resistance $R_p$ and series resistance $R_s$.

## 2.3 Generation and recombination of excess charge carriers

The generation of excess charge carriers in semiconductors refers to the process where electron-hole pairs are created, and the concentrations of carriers in illuminated material differ from their values in the dark [20]. Recombination refers to the process where electron-hole pairs are lost due to a spontaneous transition of an electron from the CB to a hole in the VB [45], i.e. light is turned off. Unwanted recombination activity is connected to reduced minority charge carrier lifetime in the silicon material.

The semiconductor can have so-called direct or indirect bandgap. Figure 2.3 shows the energy-momentum space of the electrons, known as the electronic dispersion diagram. Photons shown in the figure are vibrational quanta. The absorption of photons happens through excitation of an atom into a higher energy level state. Phonons in Fig. 2.3 are atomic oscillations of a solid, i.e. change in momentum [69]. A phonon can be understood as a wave and as a particle, where the waves are vibrations in the lattice [2].

In a direct bandgap semiconductor, the electron only needs a change in energy $E$ (photon) in order to be excited from the VB to the CB, see figure 2.3a. Hence, the minimum of the CB and the maximum of the VB possess the same crystal momentum value $\mathbf{p}$ [2]. In an indirect semiconductor, the top of VB and the bottom of the CB are not aligned in momentum or energy transfer, see figure 2.3b. Thus, both a photon and a phonon are needed in order to excite an electron from the VB to the CB.



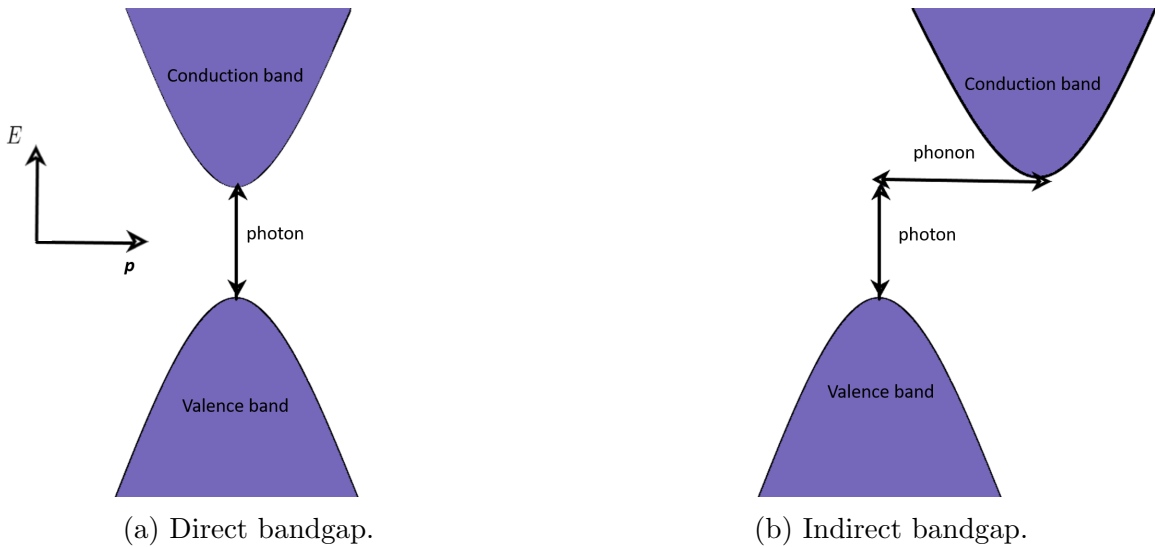(a) Direct bandgap.                    (b) Indirect bandgap.

Figure 2.3: Electronic dispersion diagram. Adapted from: Smets et al. 2016 [2].

Depending on whether the semiconductor has a direct or indirect bandgap, different recombination types occur. They can occur in parallel, in which case their recombination rates are

summed up to express the total recombination rate [20]. Recombination can affect the solar cell badly, by reducing the electric current that can be carried out of the cell [2]. Crystalline silicon is an indirect bandgap material, which means that it is more difficult for electrons to be excited than for a direct bandgap. In this section, the band-to-band generation of excess charge carriers, as well as the direct, the Shockley Read Hall, the Auger, and the surface recombination mechanisms will be explained. At last, the total minority charge carrier lifetime will be presented.

### 2.3.1 Radiative generation

In an ideal semiconductor, i.e. does not contain impurities, electrons can have energy levels below the valence band edge, $E_V$, and above the CB edge, $E_C$. When light hits a material, it is partially absorbed as it travels through the material. The photon is only absorbed if the photon energy is higher or equal to the bandgap energy, see equation 2.13 [2].

$$h\nu \geq E_G = E_C - E_V. \tag{2.13}$$

Planck constant is denoted by $h$ and $\nu$ is the photon frequency. In Fig. 2.4, a photon hits a material at a temperature above $0\,\mathrm{K}$. The energy of this photon, $E = h\nu$, is used to excite an electron from an initial energy level to a higher energy level. The bandgap energy defines the minimum energy an electron must possess in order to be excited from the VB to the CB. Electrons excited to the conduction band are in a free state, and the semiconductor is no longer in thermal equilibrium. In the CB, there is now an excess electron concentration ($n > n_0$). In the VB, there is an excess concentration of holes ($p > p_0$). The generation of electron-hole pairs that occur from bandgap to bandgap, is called direct generation.
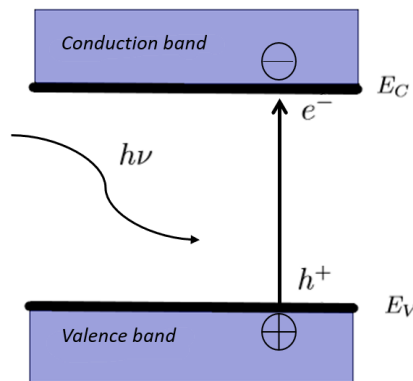


Figure 2.4: Schematic illustration of the generation of an electron-hole pair by photon excitation. The negative atom denotes the electron $e^-$, while the positive atom is the unoccupied state, hole $h^+$. Adapted from: Smets et al. 2016 [2].

The direct generation of excess charge carriers in Fig. 2.4 applies for an ideal semiconductor. For the case of a real semiconductor, the VB and the CB are not flat but vary depending on the momentum of an electron in the semiconductor. The breaking of a covalent bond leads to the formation of an electron-hole pair, and demands for minimum energy of $1.12\,\text{eV}$ for silicon. When the pulse from the photon stops, the electron recombines with a hole until equilibrium is reached [2].

### 2.3.2 Direct recombination

Direct recombination is an intrinsic mechanism, dominant in a direct bandgap. In Fig. 2.5, a hole reacts with an electron and emits a photon expressed in equation 2.14, which is exactly the reverse process of radiative generation of electron-hole pairs [69].

$$e^- + h^+ \to \gamma. \tag{2.14}$$

The emitted photon $\gamma$ has an energy level higher or equal to the bandgap energy. This is due to the fact that the initialization of excess carrier energy is lost before the recombination happens, caused by thermalization. The photon can be absorbed a second time before leaving the crystal lattice [2].
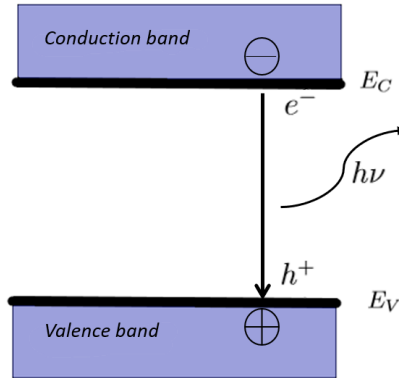


Figure 2.5: Schematic illustration of the direct recombination mechanism using the energy band diagram. Adapted from: Smets et al. 2016 [2].

As explained in subsection 2.1.2, the concentration of electrons and holes are equal to the square of intrinsic charge carrier concentration in thermal equilibrium; $np = n_i^2$. The generation rate $G_{th}$ is therefore equal to the recombination rate $R_{th}$, where $th$ stands for thermal [2].

$$R_{th} = G_{th}. \tag{2.15}$$

A free electron and a free hole must find each other for direct recombination, so the rate $R_{th}$ at which electrons and holes are annihilated and photons are generated increases with the concentration of electrons and holes [69], viewed in equation 2.16.

$$R_{th} = \beta n_0 p_0, \tag{2.16}$$

where $\beta$ is a proportionality factor which relates the recombination rate with the concentrations of electrons and holes. $\beta$ increases as the temperature decreases [2]. The total recombination rate is given by

$$R^* = \beta np = \beta(n_0 + \Delta n)(p_0 + \Delta p), \tag{2.17}$$

where $\Delta n$ and $\Delta p$ are the excess carrier concentrations [2].

The net direct recombination rate of $R_d$ is the difference between the total recombination and the thermal generation of excess charge carriers.

$$R_d = R^* - G_{th}. \tag{2.18}$$

By substituting Eqs. 2.15, 2.16 and 2.17 into equation 2.18, the following equation is obtained.

$$R_d = \beta(np - n_0 p_0). \tag{2.19}$$

The average distance a charge carrier can travel in the material before recombination is called the diffusion length, connected to the lifetime of minority charge carriers. It is a standard metric used for describing the yield of a solar cell. In n-type material, $\Delta n \ll n$ and $p \ll n$, and the recombination rate takes form as in equation 2.20.

$$R_d \approx \beta n_0(p - p_0) = \frac{p - p_0}{\tau_{pd}}, \tag{2.20}$$

where the minority carrier lifetime is defined as

$$\tau_{pd} = \frac{1}{\beta n_0}. \tag{2.21}$$

For p-type material it is expressed as $R_d \approx \beta p_0(n - n_0) = \frac{n - n_0}{\tau_{ed}}$ and thus the minority carrier lifetime can be described as

$$\tau_{ed} = \frac{1}{\beta p_0}. \tag{2.22}$$

The minority carrier diffusion length for n-type material is expressed as:

$$L_p = \sqrt{D_p \tau_{pd}}, \tag{2.23}$$

and for electrons in p-type material, it is expressed as

14

$$L_e = \sqrt{D_e \tau_{ed}}. \tag{2.24}$$

$D_e$ and $D_p$ are the diffusion coefficients in [m$^2$/s] [2]. The derivation of Eqs. 2.23 and 2.24 can be found in Appendix A.

### 2.3.3 Shockley Read Hall recombination

William B. Shockley, William T. Read and Robert N. Hall published in 1952 the theory of the recombination mechanism named after them: Shockley Read Hall (SRH) recombination [47]. SRH recombination is an extrinsic mechanism, i.e. a step-wise process where the electron transition happens via energy levels within the bandgap. The recombination process is facilitated by an impurity atom which introduces so-called trap-states, with energy $E_T$. The lattice defects allow the electron and hole to recombine before reaching the VB [47]. The SRH recombination is normally radiative, and has been stated as the most occurred recombination mechanism in semiconductors at operational conditions [2]. It is built upon four processes for a single-atom donor-type trap, shown in figure 2.6.
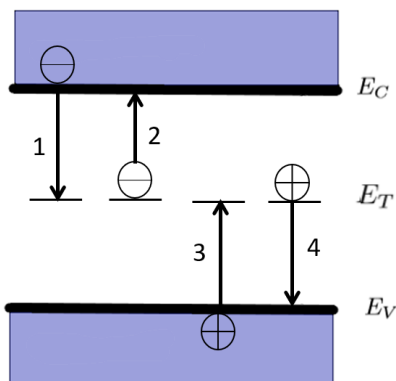


Figure 2.6: Schematic illustration of the processes involved with SRH recombination. Reaction 1 is the capture of an electron from the CB, reaction 2 is the emission of an electron to the CB, reaction 3 is the capture of a hole from the VB, reaction 4 is the emission of a hole to the VB. Adapted from: Smets et al. 2016 [2].

In thermal equilibrium, reaction number 1 and 2 in figure 2.6 are equal, and number 3 and 4 are equal: $r_1 = r_2$ and $r_3 = r_4$. According to equation 2.1, the occupation function in thermal equilibrium can be expressed as

$$f_e(E_T) = \frac{1}{\exp\left[(E_T - E_F)/kT\right] + 1}. \tag{2.25}$$

From Table 7.1 in *Solar Energy, The Physics and Engineering of Photovoltaic conversion, technologies, and systems* by Smets et al. [2], the emission coefficients in the four different processes in SRH recombination can be expressed.

$$\epsilon_e = v_{th}\sigma_e N_C \exp\frac{E_T - E_C}{kT} = v_{th}\sigma_e n_i \exp\frac{E_T - E_{F,i}}{kT}, \tag{2.26}$$

$$\epsilon_p = v_{th}\sigma_p N_V \exp\frac{E_V - E_T}{kT} = v_{th}\sigma_p n_i \exp\frac{E_{F,i} - E_T}{kT}. \tag{2.27}$$

$v_{th}$ denotes the thermal speed of charge carriers, and $\sigma$ is the capture cross-section [2].

Given a non-equilibrium case, the SRH recombination rate will vary with time, and since the process involves exactly one electron/hole, the rate for n-type material will take form as

$$R_{SRH} = \frac{dn}{dt} = r_1 - r_2 = r_3 - r_4. \tag{2.28}$$

The Fermi-Dirac distribution for a steady-state occupation function can thereby be expressed as

$$f_e(E_T) = \frac{v_{th}\sigma_e n + \epsilon_p}{V_{th}\sigma_e n + v_{th}\sigma_p p + \epsilon_e + \epsilon_p}. \tag{2.29}$$

Finally, the SRH recombination rate can be expressed based on equation 2.28 and 2.29, assuming electrons and holes have the same capture cross-section $\sigma_e = \sigma_p = \sigma$:

$$R_{SRH} = v_{th}^2 \sigma N_T \frac{np - n_i^2}{n + p + 2n_i \cosh(\frac{E_T - E_{F,i}}{kT})}, \tag{2.30}$$

where $N_T$ is the trap density. The minority charge carrier lifetime of n-type and p-type are expressed in Eqs. 2.31 and 2.32, respectively.

$$\tau_{p,SRH} = \frac{1}{c_p N_T}, \tag{2.31}$$

$$\tau_{n,SRH} = \frac{1}{c_e N_T}. \tag{2.32}$$

The lifetime of minority charge carriers due to SRH recombination is indirectly proportional to the trap density $N_T$ and the hole capture coefficient $c_{e/p}$. Therefore, it is crucial to keep both $N_T$ and $c_{e/p}$ low, in order to have a good semiconductor [2].

## 2.3.4 Auger recombination

Auger recombination is an intrinsic mechanism, where either two electrons and one hole, or two holes and one electron are included in the process. Auger recombination is important for

indirect bandgap semiconductors because both momentum and energy are transferred from one electron/hole to another. If the third particle is a hole in the VB, it will be excited to a lower energy level. If the third particle is an electron in the CB, it is excited to a higher level [2]. The third electron/hole relaxes again after this and transfers its energy to vibrational energy of the lattice, i.e. phonon modes. This is known as thermalization. The process of Auger recombination can be seen in figure 2.7.
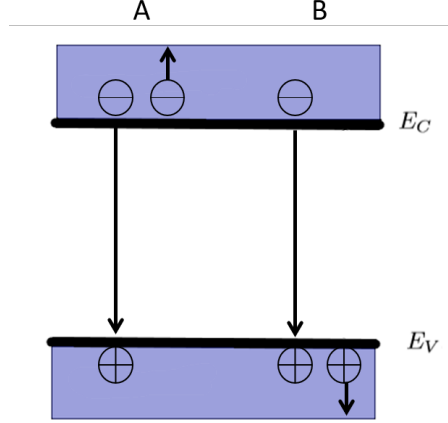


Figure 2.7: Schematic illustration of the Auger recombination mechanism. Case A has two electrons (eeh) and case B has two holes (ehh). Adapted from: Smets et al. 2016 [2].

The Auger recombination rate with two electrons (eeh) or two holes (ehh) is dependent on the charge carrier densities for the electrons and holes. They are given by

$$R_{eeh} = C_e n^2 p, \tag{2.33}$$

$$R_{ehh} = C_p n p^2, \tag{2.34}$$

where $C_e$ and $C_p$ are the proportionality constants dependent on temperature. $R_{eeh}$ dominates in n-type material, and $R_{ehh}$ dominates in p-type material [2]. The net Auger recombination rate is obtained by adding Eqs. 2.33 and 2.34 together.

$$R_{Aug} = R_{eeh} + R_{ehh} = C_e n^2 p + C_p n p^2. \tag{2.35}$$

The minority charge carrier lifetime can also be calculated as a sum of n-type silicon with a donor concentration $N_D \approx n$ and p-type silicon with an acceptor concentration $N_A \approx p$.

$$\tau_{Aug} = \tau_{eeh} + \tau_{ehh} = \frac{1}{C_e N_D^2} + \frac{1}{C_p N_A^2} = \frac{1}{(C_e + C_p)\Delta n^2}. \tag{2.36}$$

The excess carrier density is expressed as $\Delta n = n - n_0 = p - p_0$. The Auger recombination mechanism dominates the direct recombination under high-level doping [2].

17

### 2.3.5 Surface recombination

The three previously explained recombination mechanisms are inside the bulk of a semiconductor. Surface recombination happens at the surface of the lattice [2]. In silicon, there are four valence electrons which do not form covalent bonds due to the absence of other atoms. This results in loose-hanging electrons on the surface also called dangling bonds. Due to this defect, many trap states can be formed in the forbidden bandgap of silicon, and cause SRH recombination, see figure 2.8.
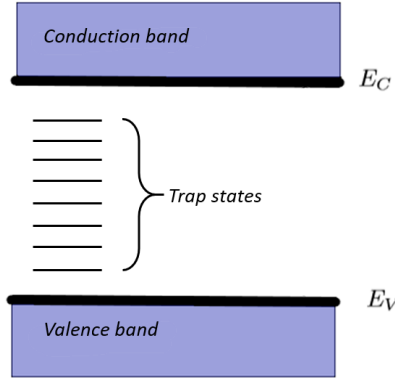


Figure 2.8: Schematic illustration of the trap states within the bandgap created by surface defects. Adapted from: Smets et al. 2016 [2].

The surface recombination rate $R_{sur}$ for n-type material can be expressed as

$$R_{sur} \approx v_{th}\sigma_p N_{s,T}(p_{sur} - p_0). \tag{2.37}$$

$N_{s,T}$ denotes the surface trap density and $p_{sur}$ is the concentration of holes at the surface. $p_0$ is the equilibrium hole concentration in n-type semiconductor [2]. To express the surface recombination for p-type material, every subscript and variable $p$ is changed to $n$.

In order to keep the solar cell of high performance, a surface recombination velocity $S_r = v_{th}\sigma N_{s,T}$ must be kept at a low value. This can be achieved by reducing the surface trap density with a passivation layer (thin layer of a suitable material put onto the semiconductor surface). With the passivation layer, the valence electrons on the surface of the semiconductor material can form covalent bonds, such that the surface trap density is reduced [2]. When studying a wafer before the solar cell production, the passivation layer can be neglected, if the sample still will be heated and such. The overall performance of the solar cell can also be kept high by reducing the excess minority charge carrier concentration at the surface. This can be done by high doping just underneath the surface in order to create a wall, so that $p_{sur}/n_{sur}$ and hence the surface recombination rate are reduced [2].

### 2.3.6 The total minority charge carrier lifetime

The four recombination mechanisms explained in this section can occur simultaneously. The total recombination rate is expressed in 2.38.

$$R_{total} = R_d + R_{SRH} + R_{Aug} + R_{sur}. \tag{2.38}$$

The recombination rate is inversely proportional to the minority charge carrier lifetime, thereby the total lifetime can be expressed as

$$(\tau_{total})^{-1} = (\tau_d)^{-1} + (\tau_{SRH})^{-1} + (\tau_{Aug})^{-1} + (\tau_{sur})^{-1}, \tag{2.39}$$

where the lifetime of surface recombination can be neglected due to a passivation layer [2].

## 2.4 Defects in Czochralski-grown silicon crystals

Although the CZ process results in high purity silicon, the growth of single crystal silicon still introduces the formation of oxidation-induced stacking faults, crystallographic defects, as well as oxygen precipitates [13]. They decrease the minority carrier lifetime, thereby encourage to a lower quality of mono c-Si material.

Non-silicon atoms are considered to be impurities, some of them added intentionally, others by a mistake. The crystal lattice of silicon is not very dense, which results in a lot of scopes to occupy in the interstitial areas [13]. Vacancies are created when a silicon atom is missing from the lattice. In the presence of vacancies, there are other spots for unwanted atoms to choose, resulting in chemical bonding with the silicon atoms [13].

Unintentionally introduced metals create defect levels in the bandgap, which are difficult to remove [13]. In order to reduce the metal impurities and defects in the future, it is of great importance to know from where these originate and how to eventually remove them. The main sources of metal impurities are the polysilicon, the dopant, the quartz crucible, the carbon parts of the furnace, the purity of argon gas, the crystal puller and the seed holder [13].

### 2.4.1 Point defects

Through an agglomeration of intrinsic point defects in the crystal matrix, there are two main types in silicon: self-interstitials and vacancies. Self-interstitials are atoms not bonded with silicon atoms in the structure. This defect type cannot be removed by increasing the level of crystal purity. Though the electrical conductivity is enhanced, the additional energy levels in the bandgap possibly increase the recombination rate [13]. This leads to a reducing resistivity in regions with better conductivity, shown in a study by Cazcarra et al. [7].

An example of an extrinsic point defect in CZ-Si is interstitial oxygen $O_i$, that occurs between the Si atoms in the lattice. $O_i$ is the most predominant defect in CZ-grown silicon crystals [33]. The relevance of $O_i$ to integrated electrical circuit fabrication is caused primarily

to oxygen's behavior in the device processing. Oxygen enters the silicon melt via dissolution of the quartz, where 95% of the oxygen disappears into the free melt surface, leaving less than 5% to the growing crystal [13]. The disappearing oxygen is carried away by an argon gas outside the crucible area. In the silicon lattice, the formation of vacancy-oxygen pairs contributes to the silicon interstitial saturation, which in turn gives rise to interstitial-type defects [13]. Hence, the concentration of dissolved interstitial oxygen plays an important role in the aggregation process of point defects.

### 2.4.2 Line defects

The presence of line defects in single crystalline silicon is considered to be of large size and importance to the efficiency limiting in silicon solar cells. Line defects are dislocations normally located at the lattice edges [6]. The dislocations can also be formed by a shift of an atom in the lattice, thereby called screw dislocations. The line defects (normally a mixture between edge and screw dislocations) are not easy to detect at the beginning of crystal growth. As the temperature rises, the line defects become visible due to their size [13].

### 2.4.3 Bulk defects

Bulk defects are vacancies and oxygen interstitials grown-in the crystal created from the CZ process. According to a study by Fujimori [18], the morphology of oxygen precipitates in CZ-Si crystals is dependent on the annealing temperature and the oxygen supersaturation due to out-diffusion[1]. The exposure to higher temperature leads to atoms/ions moving more freely in the lattice, leading to solid-state reactions. This mobilization initiates bulk defects like precipitates. They are observed as clusters in the lattice during the growth of a silicon crystal and are a serious threat to the performance of the resulting solar cell [13]. The non-uniformity metallic ion precipitates give rise to excess charge carriers. As a result, metal impurities are incorporated in the lattice. The impurities can readily affect the electrical and optical properties of the bulk silicon.

### 2.4.4 Oxygen-related defects: Thermal donors

Thermal donors (TDs) are formed by polymerization of silicon and oxygen in the temperature range of $400\,°C$ to $550\,°C$, concluded in 1956 by Fuller and Logan [19]. The electrical conductivity was found to increase due to increased donor concentration. Kaiser et al. [26] confirmed the findings of Fuller and Logan in 1958. They were the first to establish the correlation between interstitial oxygen and TDs in silicon. Since Kaiser et al. published their results, extensive studies have confirmed that TD formation is affected by $O_i$ [25]. TDs are thus concluded to be self-interstitial agglomerates around a core of oxygen atoms and vacancies. Oxygen precipitates

---

[1]Undesired diffusion occurring when dopant atoms diffuse from high-dopant material to low-dopant material.

SiO$_2$ are swirl defects from the CZ process and they act as recombination centers [22]. The oxygen precipitates can possibly lead to an efficiency loss of more than 1 % for an industrial solar cell [21], [62]. The TDs are recombination-active and they introduce several energy levels in the silicon bandgap. This creates recombination pathways for the photoexcited charge carriers. The TDs act as double donors to the conduction band. TD concentration is found to decrease for long annealing time ($t \sim 24$h). However, in a recent study, it was shown that the maximum donor generation happens somewhere between 66 h to 99 h at 450 °C annealing temperature [22].

## 2.5 Luminescence in crystalline silicon

Luminescence in c-Si material can happen in three different forms. The first is called electroluminescence (EL), which involves the excitement of electrons due to an electric current, i.e. generating light [30]. The second phenomenon of luminescence is called cathodoluminescence (CL), where electromagnetic radiation (light) in the ultraviolet to the near-infrared (NIR) electromagnetic spectrum is generated by fast-moving electrons (cathode rays) in a beam. The last phenomenon is called photoluminescence (PL) and will be the focus of this thesis. It is defined as direct recombination achieved by illuminating electrons, explained in subsection 2.3.2.

### 2.5.1 Band-to-band photoluminescence

Band-to-band photoluminescence (BB PL) is referred to the highest photon energy peak in the PL spectrum. The bandgap in c-Si varies from 1.12 eV at 90 K to 1.08 eV at 300 K [64], [36], due to the thermal expansion and available phonons in the silicon material. As stated in subsection 2.3.3, SRH recombination causes the electrons to be trapped in energy levels in the silicon bandgap. By elevating the temperature, the electrons can thermally be excited from the SRH traps. The lattice is thermally expanded, and there is a change in bond lengths. The second reason for the temperature dependence of bandgap is related to the electron-phonon interaction in the silicon lattice. At low temperatures, there are only a few allowed phonon energies, and the concentration of available phonon decreases. The charge carriers in the silicon material will find the lowest energy level to occupy, i.e. in the VB. This will result in BB signals with sharp peaks in the PL spectrum. At higher temperatures, the charge carriers will occupy states further away from the edges. Hence, the recombination rate increases and the sharp peaks will be less distinct.

On a lower-energy side of the BB signal, a phonon replica of the BB transition is present. The energy has been released from the recombining electron-hole-pair and transmitted to a phonon instead of being emitted as a photon. The phonon replica changes its energy level based on which temperature the c-Si material has.

### 2.5.2   Defect-related luminescence

Defect-related luminescence (DRL) is defined as radiative emissions from crystal imperfections, such as low-energy emitted during charge carrier injection [57]. DRL is caused by SRH recombination of electrons and holes within the bandgap of silicon. In an ideal semiconductor, there are understandably no DRL signals, because there are no defect levels in the bandgap. DRL associated with oxygen in CZ-Si has been an important research topic since the 1980s. Minaev and Mudryi [37] first presented the relation by investigating thermally induced oxygen defects in silicon. Several DRL emission lines were found between $0.75\,\text{eV}$ to $1.2\,\text{eV}$.

### 2.5.3   Hyperspectral photoluminescence imaging

Hyperspectral photoluminescence (HSPL) cameras collect image data simultaneously in hundreds of narrow spectral bands over a wide wavelength range, typically from visible through middle infrared ranges [49]. HSPL imaging makes it possible to derive a full continuous spectrum for each pixel in the image. Mehl established in 2018 that HSPL imaging can be used as a characterization method for studying defects in wafers and solar cells [35]. The advantage with the method is that it is fast and non-destructive for defect investigation in silicon wafers [24], [16], [5], [15], [21]. The HSPL method can be used in any stage of solar cell processing, from the pure absorber material to the finished solar cell [69]. In order to interpret the HSPL images, an understanding of what properties of materials measured is required [49].

There are two main types of hyperspectral cameras: filter wheel camera and line scan camera [29]. The former is a filter based system which records the entire sample at once. The latter is referred to as a push-broom camera and scans the sample line-by-line [29]. An optical dispersing component in the line scan camera splits the light into many wavelength bands, while the energy is measured separately in a detector.

The line scan camera will be in focus for this work and it will, therefore, be given a thorough description of the working principle. The line scan camera moves slowly across the sample, recording the signal from one row of pixels simultaneously. Subsequently, the camera moves to the next row of pixels and records them. It projects a slit and disperses it with a grating. The incoming light lands on the diffraction grating for each pixel, which causes the light to deflect. The diffraction angle depends on the incoming photon's wavelength, as can be seen in equation 2.40 [61].

$$\sin\theta_m = \frac{m\lambda}{d},\tag{2.40}$$

where $\theta_m$ is the deflection angle for any given wavelength $\lambda$ for maximum diffraction $m$, and $d$ denotes the distance between the splits.

To the left in Fig. 2.9, there is a c-Si sample and the direction in which it is scanned. At normal operation of the HSPL camera, 1st order maximum of diffracted light will be detected. This means that a two-dimensional image is made from each row of spatial pixels. The first

dimension is the spatial dimension, and the second dimension corresponds to the wavelengths. An additional spatial dimension is obtained by assembling the scanned cells while the camera is moving. The resulting data file is a 3D hypercube with two spatial dimensions in the $x$- and $y$-plane and one spectral resolution in the $z$-plane, visualized to the right in figure 2.9.
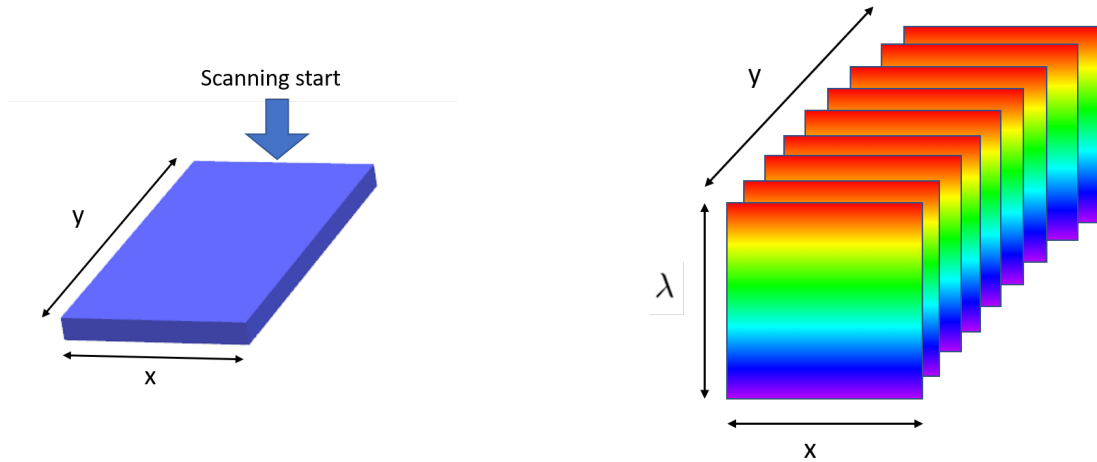


Figure 2.9: A c-Si sample and the hypercube with a 2D image on each wavelength value.

## 2.5.4   Laser penetration depth

For detecting the DRL signal, a laser can be used as an excitation source. The laser sends out photons with energy higher than the silicon bandgap and causes the electrons to be excited to a higher energy level. When electrons subsequently recombine and return to a lower energy state, they emit photons that are detected by an HSPL imaging camera [49]. If the samples are unpassivated (see 2.3.5), the HSPL measurements will be influenced by non-radiative surface recombination [17]. The absorption of light in c-Si material is dependent on energy. Therefore, the penetration depth of the laser in the HSPL camera depends on the wavelength of the incoming light and on the temperature. By lowering the temperature to $90\,\mathrm{K}$, the penetration depth gets longer, thereby causing higher PL signals for the HSPL camera. Jerpetjøn stated in 2011 that temperature is a crucial parameter to control when performing HSPL imaging, due to the large difference in outcomes [24]. The saw damage can go as far as $6.5\,\mu\mathrm{m}$ into the material [52], so when performing HSPL imaging at room temperature, the saw damage will play a big role in the scattering of the laser beam.

23

# Chapter 3

# Literature Study

The purpose of this chapter is to present a selection of published articles regarding the incorporation of interstitial oxygen in the silicon material, and the main spectral emission lines obtained with HSPL imaging. The premises in the extensive articles deviate from the ones used in this study, but the main trends may be compared. The spatial distribution of TDs and the origin of DRL in c-Si material have been discussed subjects since the 1970s. There are still unresolved queries related to the mechanisms behind the DRL emission lines caused by impurities, but some of the established researches will be presented in this chapter.

## 3.1  Spatial distribution of oxygen in the silicon crystal

During Czochralski crystal growth process, there are differences in silicon density and temperature along the crystal height [31]. Oxygen is an unintended dopant in the melting process that enters by dissolving the quartz crucible. The concentration of interstitial oxygen in the silicon crystal is determined by the initial oxygen distribution in the melt, at the crystal-melt interface, and in the bulk silicon. It is difficult to measure the low concentrations of possible impurities and divide them from the rest of the intentionally added silicon or dopant atoms. There is only one oxygen atom in about ten thousand silicon atoms, thereby difficult to concretely decide what happens during the early stages of oxygen precipitation [25]. The concentration of oxygen is not homogeneous in the melt, unlike the normal dopants [31].

The most dominant trait of oxygen distribution is that the highest concentration is situated at the top of the seed, and decreases towards the tail end [31]. The dissolution of the crucible is highest at the side walls as these are closest to the graphite. The dissolution subsequently absorbs oxygen and is, therefore, a big source of adding undesired oxygen in the crystal. As a result of complex interaction between chemical compounds, the oxygen concentration incorporated in the crystal becomes a part of the crystal [31].

The CZ process happens at a slow tempo, allowing the molten silicon to crystallize in the same orientation as the seed crystal [2]. This reduces the thermal stress by the diameter

change. The diffusion boundary layer will be thinner in the center than at the edge of the crystal [31]. As a consequence of this, more oxygen will be incorporated in the center than at the edge of the crystal. If the crystal is being rotated fast enough, it suppresses the effect of crucible rotation and thermal convection flows. This results in a thinner diffusion boundary layer [31]. By rotating the crucible and the crystal, the transportation of oxygen in the melt is decided by crucible dissolution rate, thermal/natural convection, forced convection and surface evaporation. The contact with the quartz crucible wall, the wall temperature, crucible rotation speed, the pull speed and fluid-flow instabilities are factors that affect the amount of oxygen incorporated in the crystal [13].

Søndenå et al. [50] showed in 2017 with minority charge carrier lifetime measurements that the degraded lifetime in the mono c-Si samples depend mostly on oxygen concentration. Towards the tail of the crystal and towards the edge of each wafer (closest to the crucible wall), it is observed increasing lifetimes with decreasing oxygen concentration. As for self-interstitials and vacancies, there is not found a visible boundary across the observed regions of the wafers [50]. Low resistivity suffers from a thermally induced degradation of the charge carrier lifetime. If the crystal has elevated pull speed, there will be less oxygen in the silicon lattice, leading to more vacancies [51]. The lifetime should be higher towards the edge of the crystal given the lower resistivity, expecting a high BB emission line. TDs are electrically active and, thereby, reduce the resistivity considerably [7], [55].

It has been shown that oxygen stacking faults occur in high density in the silicon lattice if the single crystal is being pulled with a speed between $0.5\,\mathrm{mm/min}$ to $1.0\,\mathrm{mm/min}$ [54]. As the crystal grows, the inside temperature drops with distance from the melt-point [13]. This leads to a decrease in equilibrium concentrations for point defects such as oxygen and carbon interstitials. The Frenkel reaction [3] explains why both concentrations of defects decrease from the middle of the crystal. An ion is displaced from the lattice structure to an interstitial position, leaving a vacancy and an interstitial defect between the atoms [13]. This happens without any impact on the chemical properties in the lattice. The point defect concentration, therefore, decreases due to the Frenkel reaction and drives the diffusion of the point defects into the crystal. They are thus incorporated during crystallization, and as the crystal cools down after CZ process, $O_i$, self-interstitials and vacancies may diffuse into the lattice, recombine and agglomerate to form defects [13]. The high oxygen concentration appears in the silicon crystal when there is an agglomeration of vacancies and oxygen species.

During the CZ process of crystal growth, there is an area above the quartz crucible called the cold zone. In this area, there is unintended interstitial oxygen incorporated into the silicon lattice [26]. Matsushita [34] found out that the point defect density increases exponentially as the temperature in the annealing process decreases, hence a dependence is found during crystal growth. The density of point defects differs from one cell to another, even though the initial oxygen concentration is the same [34]. This means that the formation of point defects not only depends on oxygen concentration, but also on thermal history during crystal growth. The seed end will stay in the cold zone of CZ process for a prolonged time, and the thermal history will

thereby vary as a function of crystal height with deviations in impurity distribution.

A study by Nakanishi et al. [39] showed that if two different cooling profiles are used for two crystals, the fastest cooling crystal will have much less supersaturated oxygen precipitates after 12 h heat treatment. The quenched crystal was cooled almost directly from 1000 °C to room temperature, whereas the other crystal was cooled normally according to the CZ process [39]. The former is though more energy demanding and expensive.

Oxygen concentrations can be detected at the edges of the crystal, also due to surface evaporation. Accelerated SiO evaporation from the melt will enhance the oxygen level in the final crystal. When the crystal is growing and solidifies, the oxygen out-diffuses and there is a drastic decrease in oxygen concentration in CZ material near the periphery region [43].

Niewelt et al. [40] have shown that the defects created by interstitial oxygen and other impurities are distributed in a swirl, circle pattern. Swirl defects occur in a circular pattern and arise during crystal pulling. When a wafer is cut, the spiral-like defects are present in the wafer in each layer [13], [21]. The spatial distribution of the rings can thus be connected directly to the concentration of oxygen in the lattice. If the c-Si material is thermally annealed at 450 °C, the distribution of the ring pattern changes and increased TD concentrations are observed in the same spots [40]. These rings are troublesome in the region of the silicon sample into which electrical components are connected to create an external circuit [65].

Voronkov et al. [66] [67] have reported that higher concentrations of interstitials in the material enhance the thermal donor generation rate. As interstitial oxygen is situated between the silicon atoms, it will react with vacancies during crystal cooling. Some of the vacancies are agglomerated into voids (empty spaces) [66]. Oxygen will assist the void formation or extended defects during cooling, by generating vacancy-oxygen clusters and oxygen precipitates. In the vacancy dominated area, the defects will diffuse from the front and into the bulk of the crystal. The diffusivity of self-interstitials is larger than that of vacancies, and will, therefore, dominate in the crystal [66], while the vacancies will dominate at the edges. A spatial transition area has been discovered between the vacancy ($V$) and self-interstitial dominating ($I$) area. The $V/I$ boundary has been called the P-band [66] (must not be confused with the P-line signal at 0.767 eV). HSPL imaging can allow for a more detailed analysis of the P-band structure of the oxygen stacking fault area.

## 3.2  Spectral response for mono- and multi-crystalline silicon materials

Since mono-crystalline silicon (mono c-Si) samples are studied in this work, a clarification of the previously studied spectral emission lines is given in Fig. 3.1. The five indications found in literature studies are 0.725 eV, 0.767 eV, 0.789 eV, 0.925 eV and 1.12 eV for the mono c-Si material. The spectrum is expressed as a spatial mean of the entire silicon sample.
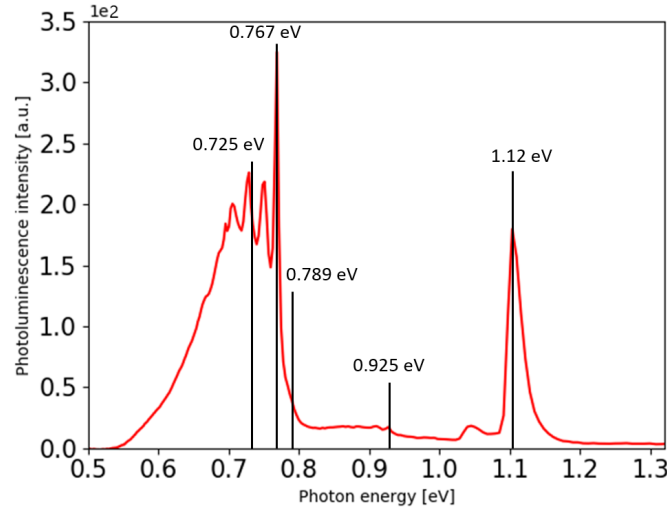


Figure 3.1: PL spectrum of a mono c-Si sample scanned at 90 K with indication of previously studied spectral emission lines.

Starting from right in the plot in Fig. 3.1, a BB emission line at 1.12 eV is seen. The BB signal is generally stated that a high PL intensity correlates with good solar cell performance [16]. Further, a typical luminescence spectrum of a sample shows a P-line at 0.767 eV, and three weaker signals called C-line at 0.789 eV, H-line 0.925 eV and 0.725 eV emission line. Mudryi et al. [38] found in 2002 that the C-line was attributed to the formation of oxygen-related centers. This was again confirmed by Tajima et al. [58] [59]. Kleverman et al. [27] concluded that the C-line was connected to donors in CZ-Si material. The P-line and H-line have been described by Helander to be connected to TDs [22]. Mehl et al. established in 2017 that the oxygen-related TDs give rise to two PL emissions at 0.767 eV at 90 K and 0.72 eV at 300 K, by the use of HSPL imaging [36].

Minaev et al. [37] showed in 1981 that some of the spectral bands from 0.75 eV to 1.20 eV were caused by the thermally-induced oxygen defects. They established the 0.767 eV emission line to be due to the oxygen-related TDs. The H-line at 0.925 eV appeared as sharp as the 0.767 eV line [37]. Based on this discovery, Tajima et al. [57] confirmed in 1983 that the

origin of the deep-level[1] luminescence in CZ-Si crystals at 0.767 eV with temperature 4.2 K and 77 K are the oxygen agglomerates responsible for the TDs. Tajima et al. [57] concluded that the TD concentration increases with both oxygen concentration and annealing time. In a study from 1995 by Maddalon-Vinante et al. [33], it was established that TDs are made of self-interstitial agglomerates. The shape of oxide precipitates changes with the duration of the annealing process. The study also showed that at 450 °C annealing treatment, TD formation is enhanced. Introducing differences in pressure, a study by Antonova et al. [1] showed that oxygen atoms participate in the formation of TDs, and the high pressure will lead to a removal of the interstitial oxygen. A study by Wijarankula and Matlock [68] showed that elimination of the oxygen TDs happens at annealing temperature 1050 °C.

Further, Pizzini et al. [44] stated in 2000 that the optical activity of TDs are correlated to a transition from a shallow donor state in the bandgap to a deep state of interstitial oxygen. The PL signals from oxygen precipitates occurred in the same region as the 0.767 eV emission line [44]. The DRL signals were also stated to be associated with the properties of the oxide precipitate interface, hence with frustrated oxygen centers, stacking faults and self-interstitial oxygen clusters [44].

In further studies of the origin of TDs, Emtsev et al. [12] established in 2003 that TDs introduce an extra energy level in silicon bandgap, and act as a double donor of electrons to the conduction band. Later on, Simoen et al. [48] showed that TD formation is a function of not only hydrogen and oxygen concentration, but also of the doping amount and -type. Hence, the Fermi-level position during the thermal anneal plays a role in the introduction rate of TDs. The charge state, i.e. the diffusion of oxygen in the lattice, is what leads to the formation of TDs. In a recent study of CZ-Si wafers it was found that thermal annealing at 450 °C gives spectral response introduced by TDs, and at temperature 650 °C the respective TDs are eliminated as the defect luminescence signal disappears to a large extent [22].

Before investigating the mono c-Si material for this work, some mc-Si wafers were scanned with the HSPL camera. Emission lines related to mc-Si defects was first discovered by Drozdov et al. in 1976 [11]. Due to the assumption that the lines are created by dislocations in the silicon lattice, they were called D-lines (D1-D4 according to their photon energy value). The five radiative emission energy levels in mc-silicon in addition to BB recombination, are called D07 (0.70 eV), D1 (0.81 eV), D2 (0.88 eV), VID3 (0.94 eV) and D4 (0.94 eV to 1 eV). The study by Drozdov et al. was confirmed by Sauer et al. [46] in 1985 when they established that the origin of D-lines is dislocations and that their emission intensity depends on the dislocation density. Further, they stated that the D-lines appear in pairs: D1/D2 and D3/D4. Figure 3.2 shows the five most common PL signals used for characterization of mc-Si solar cells, where D2 appears together with D1. The outcome corresponds well with extensive studies [35], [4], [16], [28]. The BB signal and the photon energy range of DRL signals are the same for mono- and multi-crystalline silicon (compare Figs. 3.1 and 3.2), but the specific photon energy levels differ somewhat from the two cases.

---

[1]Deep-level means that the signal appears near the mid-bandgap, instead of a shallow donor level [57].
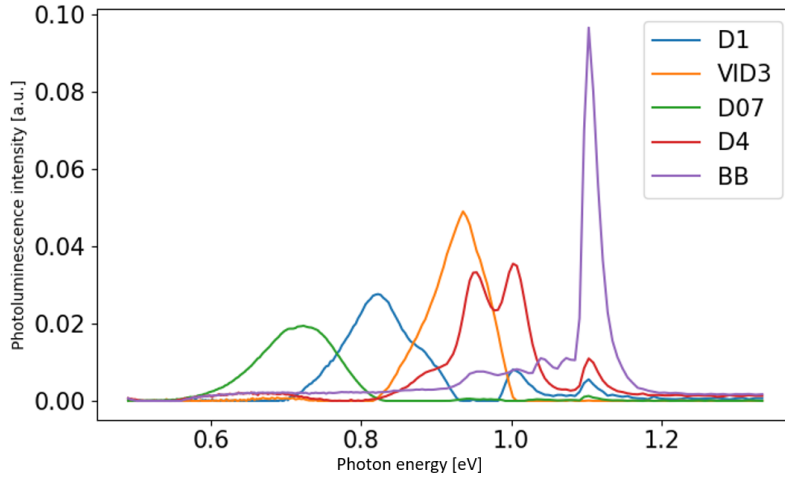
Figure 3.2: Typical photoluminescence signals [a.u.] for a mc-Si wafer sample scanned at 90 K.

Although a lot of research has been performed on the four D-lines, there is still left some unresolved aspects. Higgs et al. [23] concluded in 1992 that transition metals are sources for the emission lines. They contaminated the silicon wafer with copper, and after annealing at 900 °C for 1 h, especially D1-band luminescence showed a large PL intensity [23]. Higgs et al. tried a different concentration of transition metals (Cu, Fe, Ni, Ag, Au) and established that the level of doping is an important parameter in considering the resulting DRL signals. They suggested that increasing contamination leads to increasing DRL signals. Small precipitates are formed and they absorb the centers responsible for the radiative recombination [23]. Later on, Ostapenko et al. [42] suggested that oxygen influences the intensity of defect D1. They showed that a high sensitivity NIR camera makes it possible to obtain both spatially and spectrally separated images of sub-bandgap wavelengths. Thus, the four emissions D-lines in figure 3.2 could be obtained. In the paper by Ostapenko et al. [42], they suggested that the 0.8 eV emission line is due to electrically active dislocation networks in the silicon lattice. The clusters interact with point defects and impurities, which may be carbon, oxygen precipitates and transition metals. Wyller [70] found in 2019 that the spectral shape of mc-Si wafers is determined by the recombination mechanism with a high concentration of iron and other compounds. This leads to a decrease in the minority charge carrier lifetime [70].

The D-lines have been observed in Czochralski-grown silicon as well, by Tajima and Mathsustia [56]. This was done after thermal annealing at 1000 °C, and because CZ-Si material contains interstitial oxygen at a higher level than its solubility, the thermal annealing at such a high temperature will lead to the precipitation of oxygen. The precipitates lead to strain fields that may cause dislocations in the silicon crystal [56]. This finding will not be studied in this work, though it is interesting to study how the silicon material behaves at high temperatures.

## 3.3   Expected outcomes of this study

Table 3.1 gives an overview of the expected results for this work with a possible explanation, based on previous studies. The PVA Tepla crystals used in this study will be presented in the chapter 4. For now, it is sufficient to know that there are two crystals A and B studied. They will be compared in regards to variations of interstitial oxygen concentration, resistivity values, etching, and scanning temperature. The HSPL imaging will generate differences in the spectral and spatial dimension during processing steps of heat treatment. The wafers 1, 2, 3, 4 and 5 in Table 3.1 refer to the wafers cut between the blocks, see chapter 4 for an explanation. The values of resistivity from center to edge are shown, e.g. center value for wafer one is $1.00\,\Omega$cm, while $7\,$mm from the edge, the value for wafer one is $3.07\,\Omega$cm.

Table 3.1: Expected outputs and possible explanations based on extensive studies.

| PVA Tepla Crystals | | | | | | |
|---|---|---|---|---|---|---|
| Crystals | A | | B | | Possible explanation of outcome | |
| Blocks | A1 | A2 | B1 | B2 | | Reference |
| Pull speed [mm/min] | 0.9 | | 1.3 | | Crystal B has less time in the cold zone and may contain less oxygen but more vacancies. | [54], [50], [51], [66], [67] |
| FTIR oxygen measurements [ppma] | 17-24 | 16-21 | 14-21 | 12-16 | Higher [Oi] towards the seed end and center because of the crucible rotation, contact with the crucible walls. | [30], [24], [42], [12], [39] |
| Resistivity measurements [Ωcm] | Wafer 1: 1.00-3.07. Wafer 2: 1.29-2.46. Wafer 3: 1.85-2.41. | | Wafer 1: 1.33-2.97. Wafer 2: 2.08-2.47. Wafer 3: 1.99-2.32. | | Resistivity decreases with increased DRL signals. | [7], [55] |
| Etching process | Half of the samples are etched. | | Half of the samples are etched. | | Etching gives higher PL intensity. | [2] |
| Scanning temperature [K] | All samples are scanned at 295 K and 90 K. | | | | Lower temperature gives higher penetration depth of the laser beam. | [23], [19], [15], [52] |
| DRL signals of as-received, etched and unetched | Emission lines between 0.7-0.95 eV are previously found. | | | | Due to SRH recombination. The DRL signals increases along with [Oi]. | [13], [33], [30], [48], [41], [21], [4], [36] |
| Thermal annealing 450 ˚C: TD-dominated | Oxygen-related thermal donors will be generated. Emission lines: H-line 0.925 eV, C-line 0.789 eV, P-line 0.767 eV, 0.72 eV. | | | | The oxygen creates larger clusters in the silicon lattice and changes the electrical conductivity. | [18], [34], [43], [36], [56], [39], [67], [36], [32], [12], [48] |
| Thermal annealing 650 ˚C: TD-free | Elimination of thermal donors, i.e. all DRL lines. BB signal is enhanced for crystal B. | | | | The oxygen precipitates will out-diffuse from their centers. | [21], [56], [68], [1] |
| Multivariate Curve Resolution (MCR) analysis | It will reveal possible unseen signals and falsify/support the signals found in raw images. | | | | The MCR algorithm resolves the mixed data and returns info regarding the HSPL images. | [34], [16] |

# Chapter 4

# Experimental

Figure 4.1 is an overview of the steps included in this work. There are sixteen samples studied in this work, where eight of them are etched. The blue writing in the figure indicates the steps only the etched samples went through. All samples went through the steps in black writing. First, two CZ crystals were pulled with different velocities. This was followed by Fourier Transform Infrared (FTIR) measurements performed on the vertical cross-section samples cut from the crystals. The eight samples were put through a wet-chemical etching process, and subsequently hyperspectral photoluminescence (HSPL) imaging was done at "as-received" stage. They were etched a second time, and the "etched" and "unetched" samples were HSPL scanned. All samples were exposed to a heat treatment at $450\,°C$ to generate the TDs, followed by HSPL imaging at the "TD-dominated" stage. In the end, the samples went through a TD kill heat treatment at $650\,°C$, before performing the last HSPL imaging of the "TD-free" samples. Though it is not certain if the samples will be free of thermal donors at the last stage, they have been given this name for the case of simplicity.
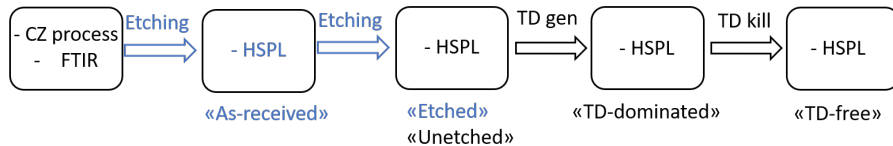


Figure 4.1: An overview of the processing steps included in this work.

## 4.1 The mono-crystalline silicon cross-section samples

The samples used in this study are n-type mono-crystalline Czochralski silicon vertical cross-section samples. Since the crystals are cut as cross-sections, a 90° deviation from the cut of wafers, it is more convenient to investigate the variation in PL signals directly as a function of crystal height. The samples were cut from two 1.1 m long crystals, shown in Fig. 4.2. Wafer 1

to 5 are slices of 2 mm thickness used to do the resistivity measurements. The cylindrical parts 1 and 2 are blocks from where the cross-section samples are cut, used for HSPL imaging and heat treatment.
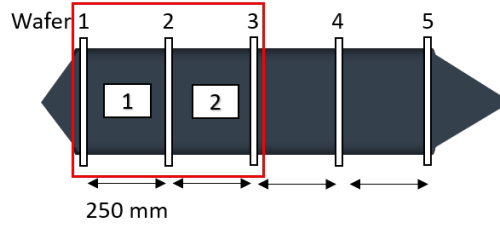


Figure 4.2: 1.1 m long CZ-Si crystal cut in three blocks of size 250 mm. Adapted from: FME SuSolTech.

The crystals were divided into blocks , shown in Fig. 4.3. Blocks A1, A2, B1, and B2 are analyzed.
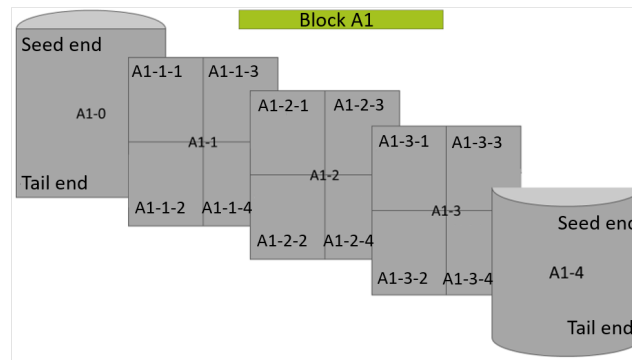


Figure 4.3: Block A1. The same cut applies for block A2, B1 and B2. Image credit: FME SuSolTech.

Table 4.1 is an overview of the samples used in this study, see Fig. 4.3 for the placement of the samples. For the sake of simplicity, the samples are referred to block name A1, A2, B1 or B2, in addition to if they are etched or not.

Table 4.1: An overview of mono c-Si samples used in this study.

| Crystal | A | | B | |
|---|---|---|---|---|
| Block | A1 | A2 | B1 | B2 |
| Etched | A1-2-1, A1-2-2 | A2-2-1, A2-2-2 | B1-2-1, B1-2-2 | B2-2-1, B2-2-2 |
| Unetched | A1-3-1, A1-3-2 | A2-3-1, A2-3-2 | B1-3-1, B1-3-2 | B2-3-1, B2-3-2 |
| FTIR | A1-2-3, A1-2-4 | A2-2-3, A2-2-4 | B1-2-3, B1-2-4 | B2-2-3, B2-2-4 |
| Names used in this work | Etched/Unetched A1 | Etched/Unetched A2 | Etched/Unetched B1 | Etched/Unetched B2 |

33

The etched samples are 2.45 mm thick, while the unetched samples are 2.65 mm thick. All samples are 125.3 mm long and 102.5 mm wide. Images of an etched and an unetched sample is shown in figure 4.4.
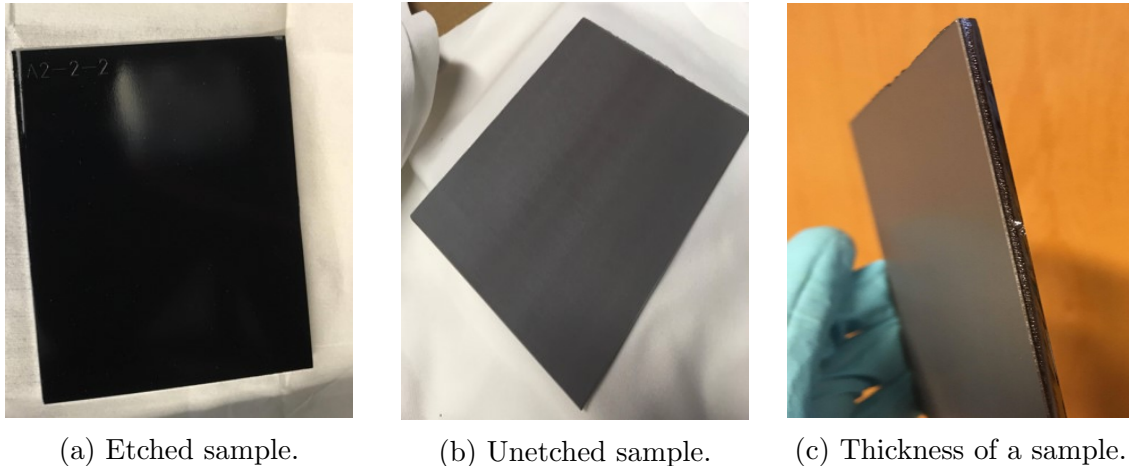


(a) Etched sample.　　　(b) Unetched sample.　　　(c) Thickness of a sample.

Figure 4.4: The etched and unetched mono c-Si cross-section samples.

## 4.2　Wet-chemical etching process

Four samples from crystal A together with four samples from crystal B were etched in order to smoothen the sample surface and remove saw damages. In this etching process, approximately 0.2 mm of the silicon material was removed. The samples were etched with Chemical Polish 5 (CP5)-solution, where 5 indicates the ratio between $HNO_3$ and HF. The process contains $HNO_3$ (65 %):$CH_3COOH$ (100 %):HF (48 %), ratio 10:5:2. This was first done at 75 °C, and the samples obtained strange markings, with a frame pattern around the edge, which will be shown in subsection 6.2.1. Therefore, they were re-etched in a CP5-solution at 25 °C to 35 °C for ten minutes. The samples were put in two different cassettes to ensure comparable etching of the cassettes. After the etching process, the samples were put in de-ionized (DI) water and HF-dip for two minutes, followed by dipping them in DI-water one more time before blow-drying them with a $N_2$-gun. For simplicity, the samples after the second etch are called "etched".

## 4.3　Oxygen concentration measurements

The Fourier Transform Infrared (FTIR) Spectroscopy measurements were performed to obtain interstitial oxygen concentration for the samples. The FTIR measurements of the neighbor samples were used for this work's samples, because it is assumed that the oxygen level is symmetrical from the center of the crystal towards the edge. There are FTIR instruments

that can measure complexes of oxygen, but the one used in this study measures free oxygen atoms. That means that when oxygen atoms cluster together, the net concentration of oxygen decreases.

The measurements were taken 10 mm, 20 mm and 90 mm from the center of crystal A. There were only taken FTIR measurements 10 mm and 90 mm from the center of crystal B, which makes it a bit more difficult to estimate the exact distribution of interstitial oxygen in the crystal. However, the focus of this study is to look at the oxygen level as a function of the height of crystal. The FTIR measurements are collected from 10 mm to 110 mm of both the crystals' height, with a 10 mm distance between every measurements.

The concentrations of oxygen were measured to $4.6 \times 10^{17}\,\mathrm{cm^{-3}}$ to $10.8 \times 10^{17}\,\mathrm{cm^{-3}}$ for crystal A, and $1.6 \times 10^{17}\,\mathrm{cm^{-3}}$ to $9.5 \times 10^{17}\,\mathrm{cm^{-3}}$ for crystal B. The oxygen concentration is understandably lower than the silicon concentration, which makes it convenient to use the unit [ppma] when describing the oxygen level in the silicon material.

## 4.4 Thermal annealing: Thermal donor generation and elimination

By exposing the wafers to thermal annealing at 450 °C for 66 hours, the formation of TDs was done. Subsequently, they were annealed at 650 °C for 1 h to perform donor elimination process.

Before every heat treatment, the samples were cleaned with 5 % HF- solution for two minutes. This was followed by rinsing them in DI-water, subsequently putting them through the Piranha solution for eight minutes. The Piranha solution consists of $H_2SO_4$: $H_2O_2$ with ratio 4:1 and is performed at a temperature between 115 °C to 120 °C. During this process, the organic material is removed quite effectively. An exothermic reaction starts when mixing the Piranha solution, and the temperature increases to above 100 °C. The solution is usable for 30 to 40 minutes, so the samples have to be put through the Piranha solution within this time. The $H_2SO_4$ has a high viscosity (relative to water) and can be difficult to completely rinse off. The samples were again rinsed in DI-water. An oxide layer will form due to the Piranha solution, but the layer is later removed in a HF-dip. This implies that the metallic impurities on the surface were removed to a certain degree. Before putting the samples into the oven, they were again rinsed in DI-water. The rinsing process can be seen in Fig. 4.5a and the oven used for thermal annealing is shown in Fig. 4.5b.
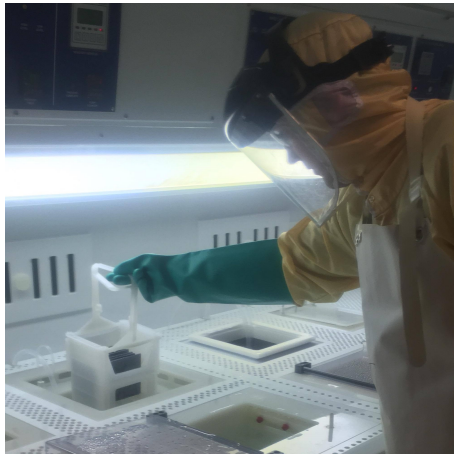
<div align="center">(a)        (b)</div>

Figure 4.5: The rinsing process and the annealing oven.

The heat treatments were done in a Tempress quartz tube furnace. One tube is dedicated to oxidation, and the heat treatment happens without dopant sources present. The heat chamber is clean, and the temperature of the thermal annealing is measured in the chamber. Therefore, it is assumed that the samples will have the same temperature as for the chamber. The samples were $N_2$-flushed during the processing to reduce oxidation. Since the samples were exposed to air before and after the heat treatment, it is assumed that an oxide layer has been formed on the samples.

## 4.5   Hyperspectral photoluminescence imaging

This section describes the laboratory work carried out with hyperspectral photoluminescence (HSPL) imaging. By using HSPL imaging, an analysis of the vacancy, oxygen, and vacancy-oxygen complexes can be done, in addition to comparing the oxygen level to the DRL signals. TDs can be investigated from these results. The BB signal from the HSPL imaging may reveal information about the minority charge carrier lifetime in the samples.

### 4.5.1   Experimental setup

Fig. 4.6 shows the experimental setup for this work. The Faculty of Science and Technology at The Norwegian University of Life Sciences (NMBU), established the imaging laboratory in 2005 [16].

<div align="center">36</div>
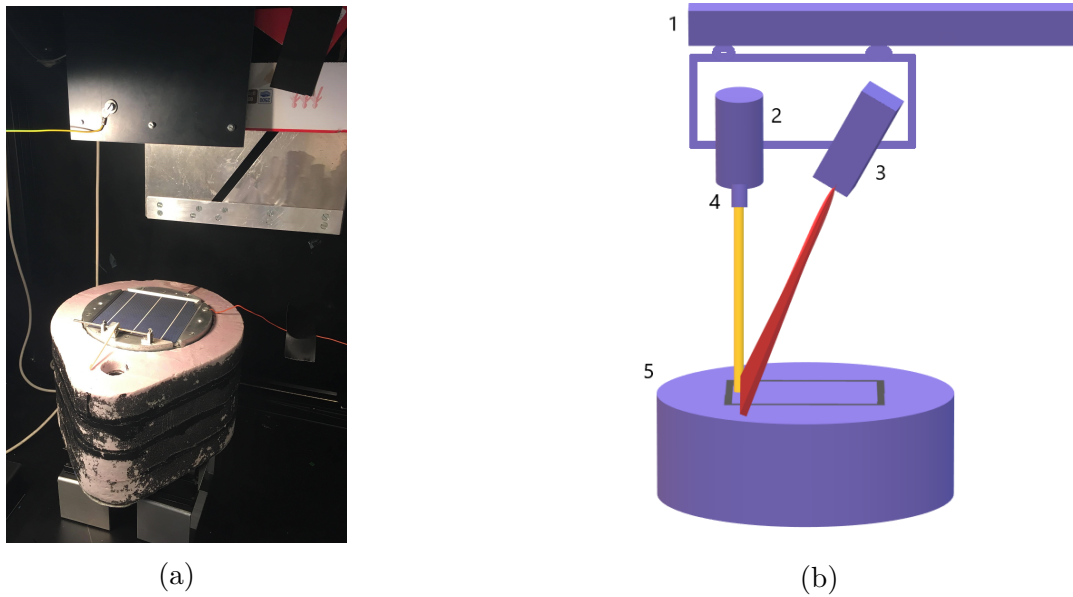
(a)                  (b)

Figure 4.6: Current hyperspectral imaging setup. 1) translation stage, 2) push broom camera, 3) line laser, 4) long pass filter, 5) cryogenic cooler.

The translation stage (no. 1 in figure 4.6b) is used for moving the camera and the laser. The laboratory at NMBU consists of several spectral cameras, and the one used in this study is a push-broom hyperspectral camera, called Short Wavelength Infrared (SWIR) Specim, Finland, with a mercury cadmium telluride detector (HgCdTe) (no. 2 in Fig. 4.6b). The camera has a wavelength range of 929.11 nm to 2530.70 nm, corresponding energy level range 1.334 eV down to 0.4899 eV. The camera records a 14 bits 2D cell, with one 320 pixels spatial- and one 256 bands spectral dimension, meaning that 256 sensors measure the light intensity for each scanning period.

The scanning speed of the linear translation stage depends on the pixel width and the frame rate. The frame rate for this study is 25 Hz, corresponding to the time between two subsequent frames as $1/25\,\text{Hz} = 0.04\,\text{s}$. The exposure was set to 20 ms. The surface onto which the sample is put can cover a $156 \times 156\text{mm}^2$ area. The scanning width is chosen to be 11 cm given the sample width of 10.3 cm. For scanning the samples, a margin of 3.5 mm is needed on each side of the width to be sure that the whole sample is included in the scan. In order to obtain quadratic pixels, the scanning speed is set to 8.2 mm/s. The spatial resolution of the scanned images is 11 cm/320 pixels= 343 $\mu$m/pixel. At higher resolution, the pixel width is reduced, leading to the lower scanning speed.

Next to the push broom camera, the line laser is placed, used as an excitation source (no. 3 in Fig. 4.6b). The laser employed in this work is named Coherent, Lasiris Magnum II, Gamatada Instrument AB, Uppsala, Sweden [8]. It illuminates (red beam in Fig. 4.6b) downwards on a wider line segment than the capture area of the camera. The laser is mounted on the same

translation stage as the camera, meaning that when the camera records the sample, the laser illuminates the line scanned by the camera. The laser needs to have shorter wavelengths than the BB emission at 1127 nm (1.12 eV) in order to excite an electron. As mentioned in chapter 2, the penetration depth of the laser is important to keep in control in order to capture characteristics from the bulk silicon material. The wavelength peak is at 808 nm for the line laser, leading to a penetration depth of 12.5 μm at 300 K and 68.5 μm at 90 K. The laser has an irradiated power density of 2 W/cm². The maximum beam power is 5600 mW and the bias voltage which can be regulated manually stays at 5.0 V.

The long pass filter (no. 4 in Fig. 4.6b) is placed in front of the camera lens, facing the sample. It blocks short wavelengths and allows longer wavelengths to be transmitted. As previously mentioned, the laser beam has shorter wavelengths than the detection range of the camera. The reflections from the laser light were therefore blocked from entering the optics. The diffraction of the laser beam due to the grating in the camera will be less than that of the incoming light. A close-up picture of the filter is shown in Fig. 4.7.
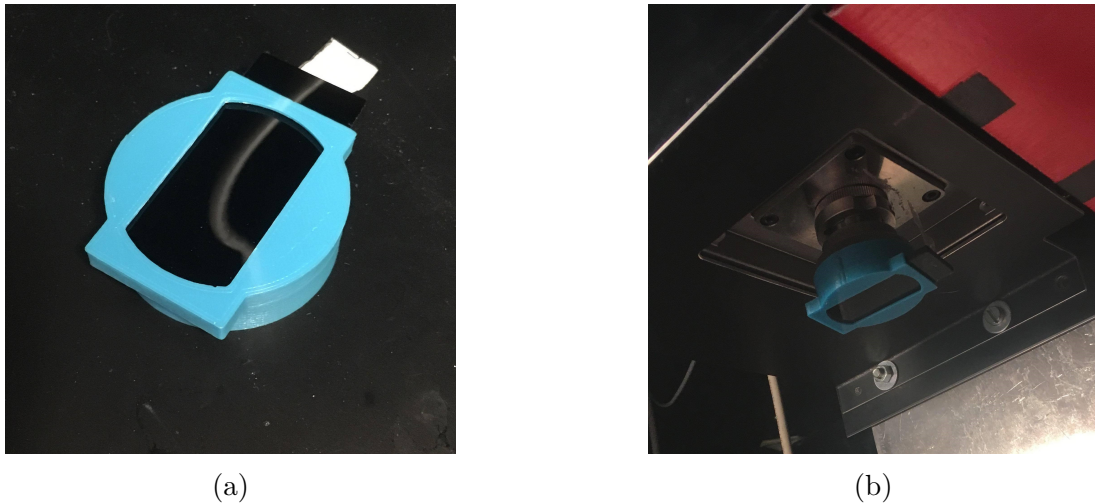


(a)            (b)

Figure 4.7: Close-up of the filter used for the HSPL imaging.

To make proper detection of DRL signals, the samples need to be cooled off to 90 K to increase the radiative recombination through traps. For this purpose, the hyperspectral imaging setup is mounted in a closed anodized aluminum cryogenic cooler, made locally at NMBU (no. 5 in figure 4.6b). On top of the container, a polished aluminum plate is placed. The outside of the container is covered with extruded polystyrene foam. The cooler must be closed to keep the liquid nitrogen from evaporating. The cryogenic cabinet is covered with a matte black layer, and all four walls surrounding the setup are black. This is important for keeping the surroundings free of reflections while the camera scans.

The cooler is filled with 2 liters of liquid nitrogen, which cools down the entire aluminum body to a temperature of −183 °C. There are small nozzles on the top to provide cold nitrogen

vapor to the sample. Thermal equilibrium is therefore quickly achieved. The small pinholes also prevent a layer of frost creating on the sample. The temperature remains constant as long as there is liquid nitrogen inside the cooler, controlled by a digital thermometer attached. If the temperature rises above $-180\,°\mathrm{C}$, the cooler needs to be refilled with liquid nitrogen, see Fig. 4.8.



Figure 4.8: Filling the cryogenic cooler with liquid nitrogen.

## 4.5.2 Calibrating the hyperspectral camera and the laser

The cryogenic cooler is put on movable blocks, which together had to be rotated manually until the camera scans the sample correctly. A reference solar cell with 0.2 mm thickness was used to calibrate the camera. Since the etched cross-section samples are 2.45 mm thick, 23 A4-papers each with thickness 0.1 mm were put under the steel plate to obtain the same thickness as the cross-section samples. The camera scanned the reference cell back and forth while adjusting the cryogenic cooler setup. When scanning the 2.65 mm thick unetched samples, two extra A4 papers were added.

The laser beam is supposed to give an evenly illuminated line on the sample, with a slight decrease towards the ends of the line [8]. This had to be calibrated by pointing the laser towards a busbar on the reference cell. Simultaneously, a wheel on the laser was rotated while inspecting the thickness of a line on the computer, as the camera recorded a reference cell. The filter was removed in order to calibrate the laser precisely.

### 4.5.3 Hyperspectral measurements

The hyperspectral imaging measurements were performed for as-received, etched/unetched, TD-dominated and TD-free samples. The samples were first scanned at 295 K, followed by cooling them down to 90 K in order to repeat the same imaging process. Each sample was scanned three times to be able to take the median of these measurements, thereby obtaining an improved image to noise ratio.

Since the etched samples are 2.45 mm thick, it was uncertain how long it would take to cool them down. After some tests, the conclusion was that they should be cooled for 4 minutes before scanning. The unetched samples with thickness 2.65 mm were cooled down for 5 minutes before scanning. The frost under the sample was removed between every scanning.

## 4.6 Band-to-band photoluminescence imaging at the Institute For Energy Technology

For TD-dominated and TD-free samples, PL imaging was done with a LIS-R1 from BTimaging. The camera is a charge coupled detector (CCD), with a 808 nm laser. The setup is equipped with a 1000 nm long pass filter and a 1050 nm short pass filter in order to avoid reflections of the laser. The whole sample was illuminated at the same time, and it may be assumed that the uniformity of the laser is well calibrated.

# Chapter 5

# Data Analysis

The hyperspectral camera scans one sample three times, and the resulting data file for each sample consists of three .RAW files, with their respective .HDR files. The samples are put in separate files in order to analyze one sample at a time in Python 3.7. Python is a multipurpose programming language and it allows for visualization and analysis of data. In this study, Multivariate Curve Resolution (MCR) is used in Python to obtain a spectrum with the most important signals from an unresolved data set. The algorithm can obtain plots that distinguish between the intensity signals at different levels of photon energy.

A collection of Python scripts have been used in the data analysis part. Some of the codes are translated by Marija Vukovic from MATLAB, and they were originally created by Mehl [35] and Flø [16]. Nofima research center has developed a package in Matlab for an evolving factor analysis used in the MCR method [41]. The Python scripts created by Marija Vukovic (author in code *mavu*) and the script personally made for this work (author in code *helstalh*) are added in a private GitHub repository.

## 5.1    Preprocessing of the hyperspectral data

The code *ReadImages.py* reads the .RAW files and takes an average of the three recorded scans in order to remove noise, i.e. strong unwanted signals. The resolution of the images is not diminished when averaging. Impulse noise in 3D HSPL images is caused by dead pixels and can appear as stripes in the scanning direction (y-plane) on the digital image. The resulting hypercube is a collection of images recorded over a period of time, and it will show variations in the noise level caused by the thermal oscillation in the camera. The background noise is removed by *LoadSubtractCorrect.py*. The impulse noise appears temporarily, so the stripe often occurs only in one of the scans of a sample. Therefore, when taking the average of three samples, the impulse noise bar is removed. The new HSPL image is saved in a new hypercube which is used for further analysis.

The scanner registers a larger area than the sample, which means that a part of the image

must be cropped away. If the three scans are not of the same 3D-size, the images must be cropped before taking the average of all three. In this case, the code *MedianHyperspectral.py* together with *RawImageSpectrum.py* performs the cropping. Often, the extra frames on some of the scans occur in the corner, i.e. outside of the actual cell. Therefore, it can easily be removed without affecting the target sample.

The cropping of the average image is subsequently performed using k-means classification in code *ExtractFrame.py*. K-means algorithm searches for the mean value in every pixel column from left and right, and does the same with every row from left and right. Sometimes, it has to search for the maximum value when the border of the cell does not have enough distinct signals, and the row/column is dominated by background signals.

The number of classes is an attribute in k-means classification. When choosing two classes for the algorithm, it does not always succeed in finding back- and foreground, where the foreground denotes the solar cell. However, when choosing, for example, six classes, the algorithm manages to separate and thus find the column/row where the cell starts. The other attribute to the k-means classifications is the number of iterations. By choosing too many iterations, the algorithm can fail to crop the image correctly. Therefore, this is a parameter which has to be regulated, normally between 5 and 20.

## 5.2 Various methods of analyzing hyperspectral images

The data in the hypercube obtained with HSPL imaging can be analyzed and presented in different ways. In this section, the data analysis performed for obtaining the results for this work are presented, in addition to discussing their reliability.

### 5.2.1 Mean spectrum of an entire sample

A practical way of extracting information from a hypercube is by plotting the mean spectrum, see Fig. 5.1a. The mean spectrum is denoted by a mean of the pixel value in each wavelength band of the hyperspectral image. The values are plotted against the photon energy of each wavelength band. The code for obtaining such plots and images is called *rawspectrum.py*. In Fig. 5.1b, the spatially integrated raw image of the photon energy range 1.08 eV to 1.15 eV (indicated in Fig. 5.1a) is shown. The colors in the image are artificial and are used to visualize the difference in signals according to the color bar to the right of the plot. More about the spatially resolved images can be read in subsection 5.2.2.
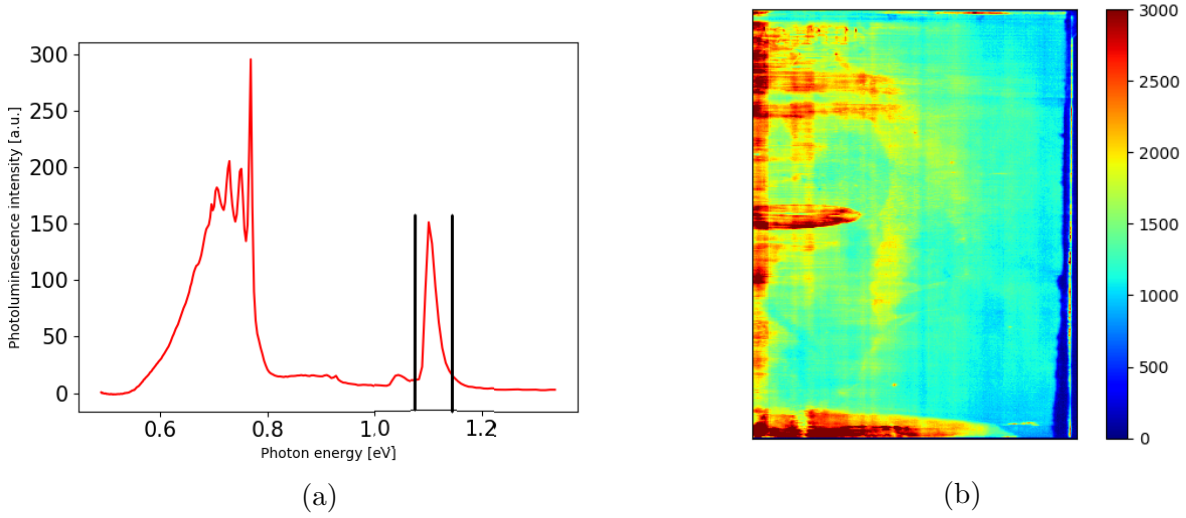
Figure 5.1: The mean photoluminescence spectrum and a spatially BB signal integrated image of a mono c-Si sample used in this study.

The laser may be in-homogeneous at some parts of the measured sample. By taking the mean spatially across the whole sample, the contribution of the strongly illuminated regions of the sample will be larger than the regions which are not as much illuminated. The sample was 180° rotated to see if the laser captures the signals correctly. Some of the same signals towards the edges were similar. The main PL signal changed as the sample was rotated, which confirms that the images can be used for analysis.

Saturation of the laser may also occur, meaning that the camera chip pixels are saturated and cause lateral diffusion of charge carriers to neighboring pixels, often called bleeding. This causes artificially high counts in the adjacent pixels. Since this work consists of the use of an HSPL camera, the two spatial dimensions may cause the saturated camera pixel to bleed not only to adjacent spatial areas but also to neighboring energy levels. The signals appearing close to each other may therefore spectrally overlap, and cause more intense signals than they should. The saturation can be avoided by reducing the laser intensity, or by analyzing as-received samples instead of processed ones, because of the reduced injection level.

Extensive researches have been solved by using Gaussian fit algorithms to resolve the individual emission lines [42]. Such methods are not included in this work. However, there are both etched and unetched samples, which will be helpful for comparison regarding the possible bleeding.

## 5.2.2 Spatially resolved images integrated over certain wavelengths

The main spectral emission lines previously discovered for the mono c-Si samples are presented in chapter 3, but now it will be given a description of how the data processing has been done

and over which energy levels the images are integrated. Each signal can be studied separately by integrating over certain wavelengths. In this way, the saturation from other signals will be avoided. Figure 5.2 is an overview of the main emission lines, together with the names used in this work and the energy band integration lower and upper limits. The integration limits have been chosen for HSPL imaging at $90\,\mathrm{K}$, by inspecting a plot of PL intensity as a function of wavelength spectral bands.



| Number | Name | Lower integration limit [eV] Chosen for this work | Upper integration limit [eV] Chosen for this work | Emission line [eV] |
|---|---|---|---|---|
| 1 | 0.67 eV | 0.66 | 0.68 | 0.667 |
| 2 | 0.68 eV | 0.68 | 0.69 | 0.685 |
| 3 | 0.70 eV | 0.70 | 0.71 | 0.705 |
| 4 | 0.72 eV | 0.72 | 0.73 | 0.725 |
| 5 | 0.75 eV | 0.74 | 0.75 | 0.749 |
| 6 | P-line | 0.76 | 0.77 | 0.767 |
| 7 | C-line | 0.78 | 0.79 | 0.789 |
| 8 | H-line | 0.92 | 0.93 | 0.925 |
| 9 | BB | 1.08 | 1.15 | 1.12 |
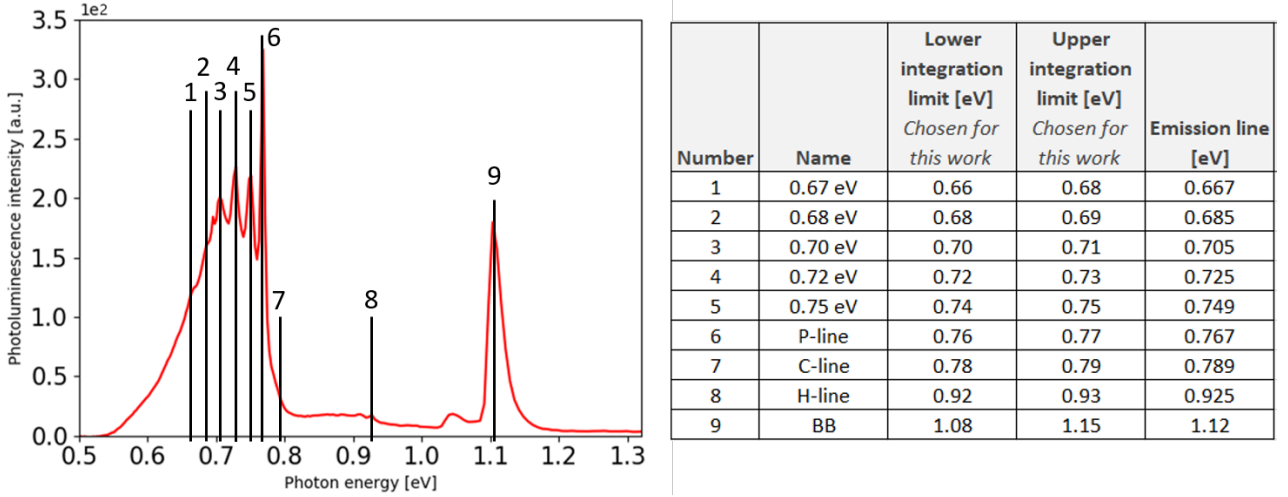
Figure 5.2: Overview of the spectral emission lines with their respective energy intervals.

For investigating specific areas of the spatially integrated images by doing line scans and comparing them with oxygen values, the codes *linescandenuded.py* and *linescanvertical.py* are used.

### 5.2.3 Multivariate statistical analysis

Multivariate Curve Resolution (MCR) is a multivariate statistical analysis method which is applicable to data sets where there is little or no prior information about the mixture of constituents. Flø [16] introduced in 2014 the use of MCR algorithm as a technique to improve the analysis of HSPL images. MCR helps resolve the mixed data by returning information about the spectral resolution in an HSPL image. Based on the assumption of Lambert-Beer's Law, MCR decomposes the dose $D$ into two matrices, one loading matrix $S^T$ for the spatial distribution of each defect, and one score matrix $C$ of their corresponding spectrum profile. By decomposing the experimental data, an error term denotes the difference between the scanned and the simulated signal, see Eq. 5.1.

$$D = CS^T + E. \tag{5.1}$$

The score matrix $C$ is optimized with an Alternating Least Squares (ALS) algorithm. The ALS also seeks to diminish the error term in Eq. 5.1. and an initial estimate of $C$ has to be provided to the algorithm. This is done with the help of code *EvolvingFactorAnalysisMultiple.py*. Three parts of the cell are chosen in order to make an estimate for the $C$-matrix. The fragments are distributed corresponding to the size of the sample.

Before analyzing the averaged cell, the hypercube must be unfolded to a two-dimensional frame. The two spatial dimensions are therefore multiplied and in return, a $(430, 320, 256)$ image is converted to a $(430 \times 320, 256) = (137600, 256)$ image. With an estimated image and a 2D image as input, the MCR algorithm can run.

From the module *pymcr.mcr*, MCR-ALS can be imported and applied to the HSPL image. For twenty iterations, the mean squared error is calculated for both $C$- and $S^T$-matrix. The code for running the MCR analysis is called *RunMCR.py*. The number of components can be user-defined between 1 and 20, which has to be chosen carefully. This depends on how many separate signals of radiative defects desired to appear. Usually, this number varies between three and seven, which is based on experience from previous studies [35], [16]. An example of two of the score plots with their loading curves is given in Figure 5.3. In the example, the $C$-matrix is folded from a 2D with seven components (of size $(137600, 7)$ in this case) to a 3D array, and the scores and loadings are plotted in different figures. The code used to obtain such plots is called *FoldingPlottingMCR.py*.
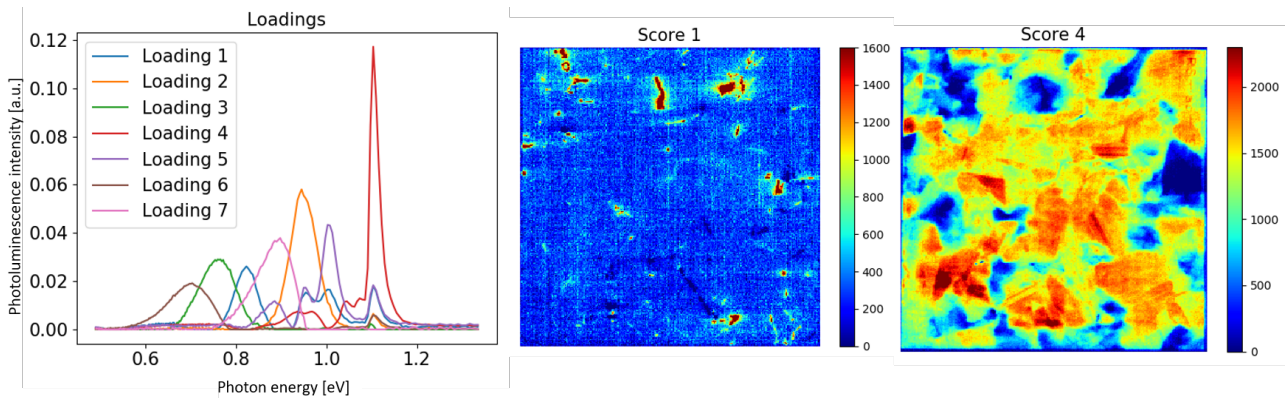


Figure 5.3: MCR analysis of a mc-Si sample with two out of seven score plots that corresponds to the loadings plot to the left.

The MCR algorithm has a weakness of possibly dividing the data set into too many or too few defect signals. Therefore, it is important to interpret the results physically, since the MCR is a mathematical approach and can be difficult to relate to physical properties in the material. It appears that in MCR algorithm, the noise is assumed to be uncorrelated of the

other data, which is not true. Therefore, it is important to do the preprocessing by removing the background noise from the sample and averaging over three scans for every cell. The MCR is not very effective at room temperature [17], thereby only images taken at 90 K have been investigated.

It should be kept in mind that MCR exhaustively extracts the most possible information of the data set. Values that deviate from each other will be featured. For instance, if there is a background energy level stretched spatially over the entire sample or spectrally over all wavelengths, the MCR algorithm will quantify the components according to the deviation from this background signal. This will lead to an increase in the total number of counts in areas with strong signals. For this purpose, the background noise is subtracted from each image.

The example in Fig. 5.3 is from mc-Si solar cells, which was used for investigation before receiving the mono c-Si cross-section samples for this work. In Fig. 5.4, the loadings, and scores 1, 4 and 5 are shown from an MCR analysis with five components for the mono c-si cross-section samples. In this example, the MCR algorithm has not achieved in separating the scores into different signals. The number of components should be lowered in order to obtain better plots.
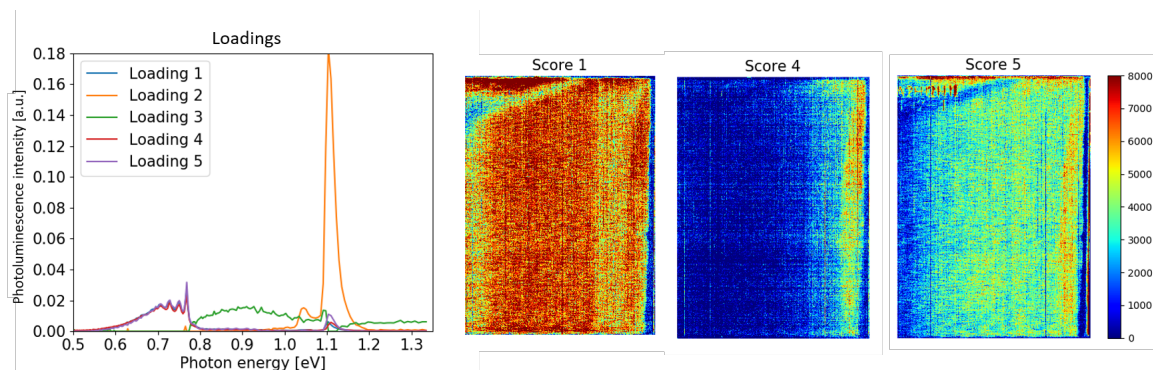


Figure 5.4: The loadings and scores 1, 4 and 5 from MCR analysis with five components for the mono c-Si samples.

A disadvantage with the MCR method is that it may plot a curve which both has peaks at DRL energy range and at BB energy range. An example of this can be seen in Fig. 5.4, where the five loadings are difficult to distinguish from each other. Score plots 1, 4 and 5 shown in 5.4 corresponds to the same PL peaks at $0.68\,\text{eV}$ to $0.79\,\text{eV}$. Scores 4 and 5 contain the BB signals, or the phonon replica (described in subsection 2.5.1), which will enhance the overall signal of the score plot. Therefore, it is crucial to compare the loadings and the corresponding scores, in order to know which spatially resolved images (score plots) can be used for analysis. Due to these queries, the MCR method is used as a supplement to the analysis for assuring that there are no other signals to investigate than found from the raw images and spectra. The raw images and the MCR created images cannot, however, be directly compared.

# Chapter 6

# Results and discussion

The objective of this work was to investigate the variation in DRL signals and oxygen-related TDs as a function of crystal height, for two crystals pulled at different velocities. The samples went through thermal annealing in order to generate and eliminate the TDs. The work is based on the established method of HSPL imaging [35], [15].

The first section in this chapter shows the spectral response at both 295 K and 90 K, during thermal annealing steps of the etched samples. Secondly, the spatially integrated images for etched/unetched, TD-dominated and TD-free samples at 90 K are presented. The variation in PL signal is shown as a function of crystal height divided into two different sections: BB signal at 1.12 eV and P-line signal at 0.767 eV. The two sections compare the FTIR measurements of interstitial oxygen and the resistivity measurements directly to the spatial distribution of the PL signals. Next, a comparison between PL measurements from two different detectors is given. There are vertical line scans for comparing the interstitial oxygen concentration and the P-line signal at particular sites of the sample. A spatial transition area has also been investigated. Further, the results from the multivariate image analysis is presented. At the end of every section, there is a discussion relating the topic in question based on the theoretical background (chapter 2), the literature study (chapter 3), and the present results. At the end of this chapter, the main findings are shortly summarized.

## 6.1 Spectral response during thermal annealing steps

In this section, the spectral response of etched and unetched samples is shown during thermal annealing steps. The etched samples constitute of four curves in one plot representing the conditions: as-received, etched, TD-dominated and TD-free. The second wet-chemical etching process counts as the condition "etched" because the first etch gave a strange frame-like pattern which will be shown in section 6.2. The unetched samples naturally contain three curves representing the conditions: unetched, TD-dominated, and TD-free. The differences in the PL intensity range [a.u.] throughout the section are made intentionally to make the variation in curves visible.

Figure 6.1 shows the spectral response for block A1 and B2 at 295 K and is chosen to be added in order to show the difference between samples scanned at room temperature and at cryogenic conditions for both crystals.



(a) A1 – Pull speed 0.9 mm/min.      (b) B2 – Pull speed 1.3 mm/min.
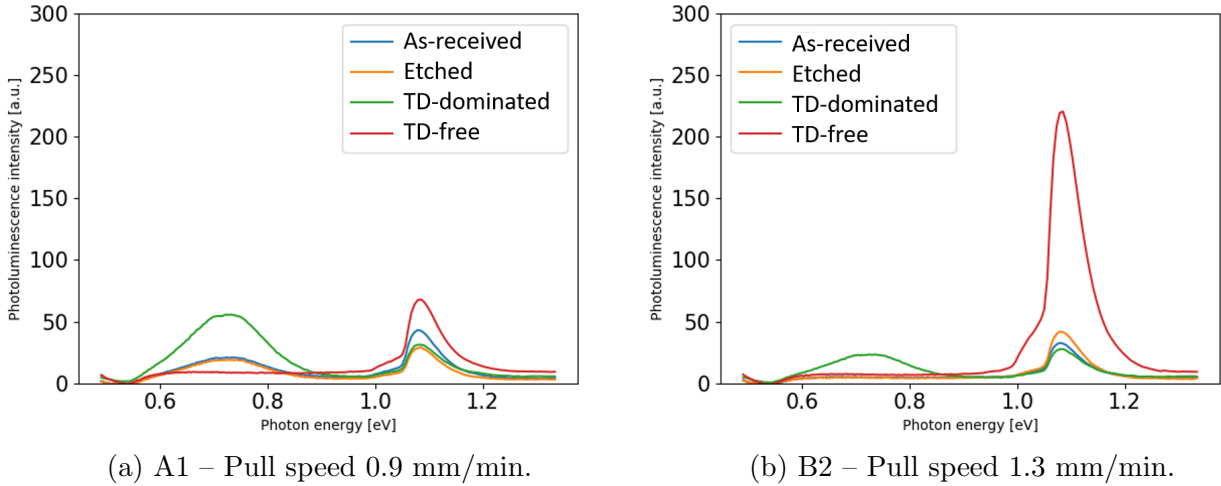
Figure 6.1: Etched samples: PL spectrum at 295 K of crystals A and B.

The mean spectra at 295 K in Fig. 6.1 show a peak in BB PL at 1.08 eV. A peak at 0.767 eV is detected at TD-dominated condition for both crystal A and B. This contradicts the findings of Mehl et al. [36]. However, they found a peak at 0.72 eV, which is previously observed by Tajima et al. [55]. The same peak is not detected in Fig. 6.1.

The mean PL spectra at 90 K of the etched samples are presented in Figs. 6.2 and 6.3. The same plots for the unetched samples are presented in Figs. 6.4 and 6.5.
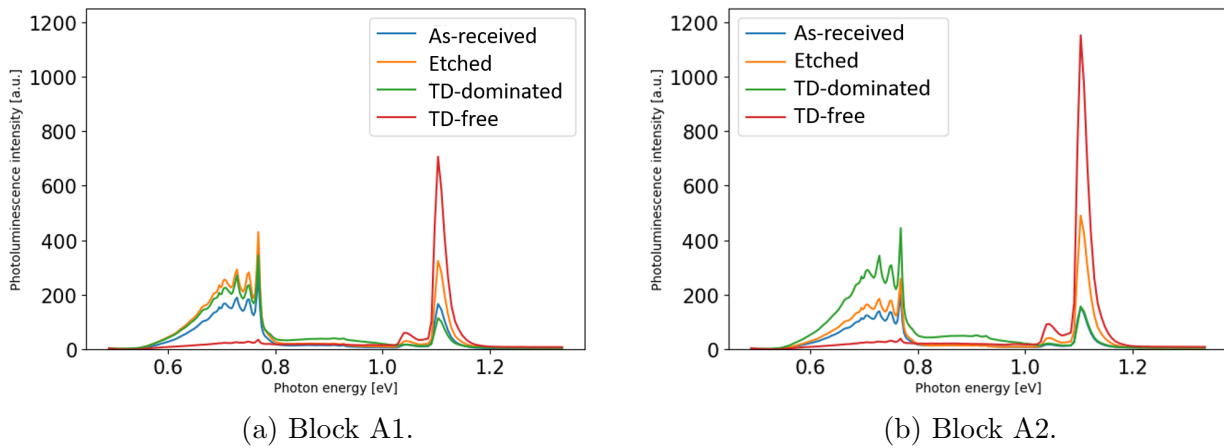


(a) Block A1.



(b) Block A2.

Figure 6.2: Etched samples: PL spectrum at 90 K of crystal A – Pull speed 0.9 mm/min.
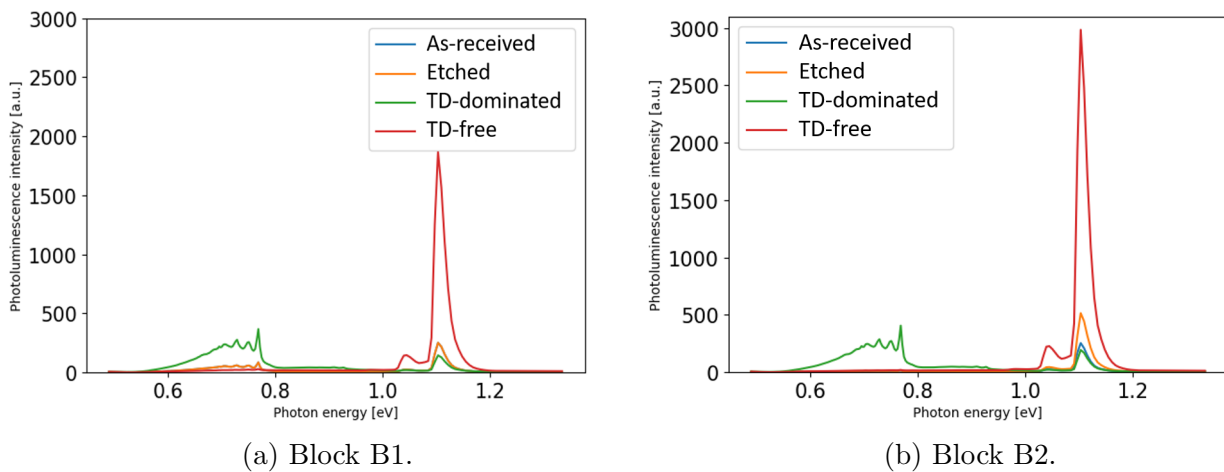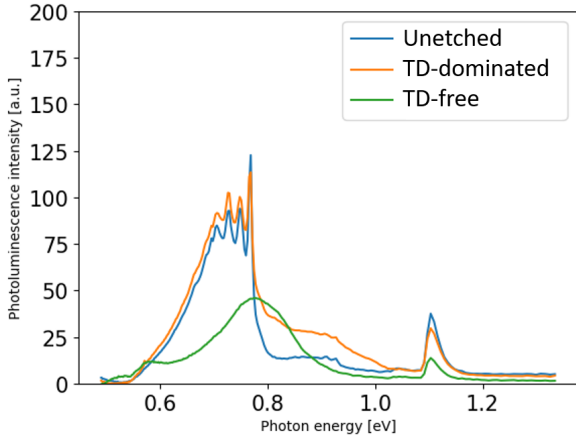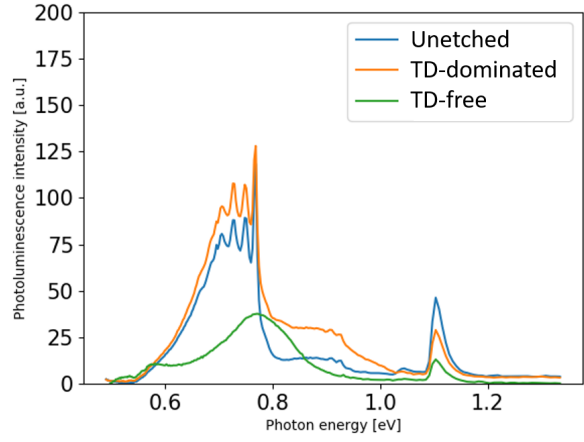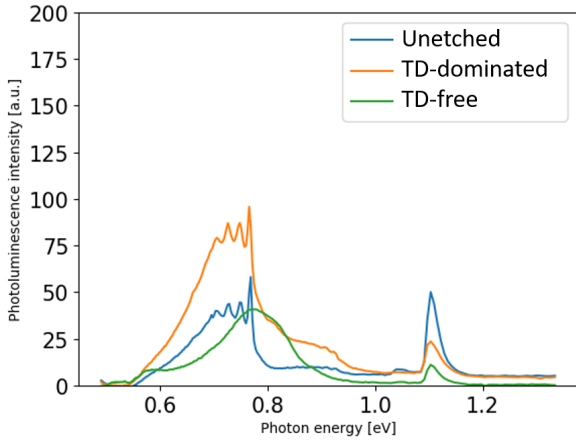


(a) Block B1.



(b) Block B2.

Figure 6.3: Etched samples: PL spectrum at 90 K of crystal B – Pull speed 1.3 mm/min.
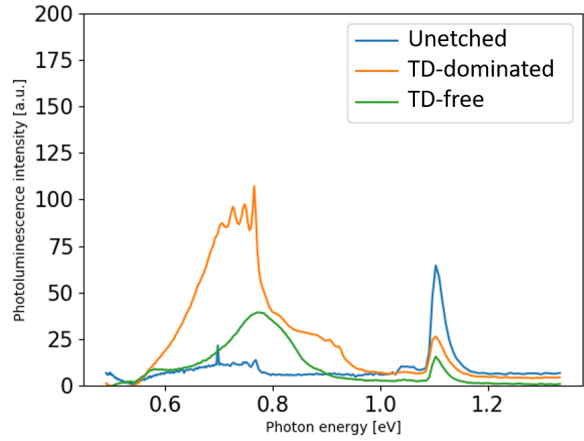
(a) Block A1.



(b) Block A2.

Figure 6.4: Unetched samples: PL spectrum at 90 K of crystal A – Pull speed 0.9 mm/min.



(a) Block B1.



(b) Block B2.

Figure 6.5: Unetched samples: PL spectrum at 90 K of crystal B – Pull speed 1.3 mm/min.

The mean spectra for samples cooled down to 90 K have considerably stronger signals than the samples scanned at room temperature, also showed by Flø [16] and Jerpetjøn [24]. The phenomenon is also discussed in chapter 2, where the penetration depth of the laser is proved to be larger for cryogenic conditions [52]. As explained in subsection 2.5.1, the phonon concentration decreases at low temperatures and the charge carriers occupy the lowest energy levels (the VB), leading to more distinct emission lines. The BB signal is shifted to a peak at 1.12 eV for the mean spectrum at 90 K. This was also shown by Mehl et al. [36] in 2017. The

50

nine indications in section 5.2.2 can be seen in Figs. 6.2, 6.3, 6.4 and 6.5: $0.704\,\text{eV}$, $0.725\,\text{eV}$, $0.749\,\text{eV}$ and $0.767\,\text{eV}$, and emission shoulders at $0.667\,\text{eV}$, $0.685\,\text{eV}$, $0.789\,\text{eV}$ and $0.925\,\text{eV}$.

In Figure 6.2, the difference between the as-received and etched is not significant, but the overall PL signal is slightly increased for the etched samples, because the surface has become even more smooth after the second wet-chemical process. The HSPL laser absorbs the etched surface more easily than for the unetched surface, which can be seen by comparing the BB signal in Figs. 6.2 and 6.4. The roughness at the surface of unetched samples may have caused more scattering in different directions of the laser beam and thereby increased the diffuse scattering. In Fig. 6.3 for crystal B, the difference between the as-received and the etched cannot be seen. The BB signal intensity is so high that the difference between other signals are reduced.

Crystal A (Figures 6.2 and 6.4) has almost the same PL intensity for DRL signals corresponding to the photon energy range $0.68\,\text{eV}$ to $0.79\,\text{eV}$ for the conditions etched and TD-dominated. Crystal B (Figures 6.3 and 6.5), on the other side, has higher DRL signals for the TD-dominated condition. Crystal A is affected by the low pull speed, obtaining almost as high PL signals as for the TD-dominated condition. The most oxygen stacking faults are created when the pull speed is below $1.0\,\text{mm/min}$ [54], which correlates well with the present results. Block B2 in Fig. 6.3b differs from block A1 in Fig. 6.2a the most due to the placement of B2 further down towards the tail end with less impurities.

After the $450\,°\text{C}$ heat treatment at TD-dominated condition, a single interstitial oxygen atom will agglomerate into larger electrically active clusters of TDs [26], [33]. It is hypothesized that the defects causing the DRL emissions in this study could be caused by TDs, which can be observed in Figs. 6.1, 6.2, 6.3, 6.4 and 6.5. The increase of the DRL emissions for block A1 in Fig. 6.2a is higher than for block B2 in Fig. 6.3b, and this phenomenon reflects back to the difference in interstitial oxygen level. The H-line appeared stronger at TD-dominated condition for all samples, most clearly viewed for the unetched samples in Fig. 6.4. The shoulder lying at $0.789\,\text{eV}$, known as the C-line, is also enhanced for TD-dominated condition. The C- and H-line appear as noise before donor generation. This can be explained by previously performed studies, which in great scale show that the C- and H-line have a relation to the TDs in CZ-Si material [36].

In a study by Mehl et al. [36], the $0.72\,\text{eV}$ emission line appeared as strong as the BB signal, whereas in this study, all DRL signals are higher than the BB signal for the unetched samples. The only sample where the $0.72\,\text{eV}$ emission line could be comparable to the BB signal is in Fig. 6.2a, which is an etched sample. The spatially resolved images of $0.72\,\text{eV}$ emission line has been investigated and can be found in Appendix C. Silicon is an indirect bandgap semiconductor (see subsection 2.3), the diffusion length of the charge carriers is substantially long, especially at cryogenic conditions. This enables the enhanced BB signal due to a strong impact from the surface recombination.

Further, the P-line at $0.767\,\text{eV}$ can be compared for TD-dominated condition between etched and unetched samples in Figs. 6.2a and 6.4a. The P-line peak for the etched sample is at 400 a.u. versus a top at 125 a.u. for the neighbor unetched sample. The unetched samples had

not been exposed to any preparation steps that may have changed the surface further than the sawing process. The rugged surface, i.e. the variations in the surface condition, could cause the optical properties to differ between the cross-section samples. At TD-dominated stage, the unetched samples have though been through a cleaning process before the heat treatment. The pre-anneal cleaning has an etching effect on the surface of the sample and reduces some of the roughness. The Piranha solution removes most of the organic material, due to the mixture of sulfuric acid and hydrogen peroxide. However, the thickness of the sample was not reduced after Piranha clean, which was checked by measuring each time before scanning the samples. Thereby, the spectral response of the TD-dominated samples may not have been affected by the cleaning process.

Figures 6.4 and 6.5 look alike the results of Helander's master thesis [22], with large DRL signals, and distinctive peaks between $0.68\,\text{eV}$ to $0.79\,\text{eV}$ for condition TD-dominated. As described in chapter 2, Helander [22] stated that DRL signals reached a peak when annealing $66\,\text{h}$ to $99\,\text{h}$, which was the reason for why the samples were annealed for $66\,\text{h}$ in this study, resulting in high emission line peaks. The reduced BB signal for thermally annealed samples at $450\,°\text{C}$ for $66$ h, corresponding to decreased bulk lifetime, is probably caused by precipitate growth in the entire sample.

Helander obtained higher DRL signals at the mean spectrum, almost as high as 800 a.u., but in this research, the etched samples only reach a top of 400 a.u. There is hence more appearance of TDs for Helander's samples than the present samples. This is an unexpected result given the differences in interstitial oxygen concentration between Helander's and the current study. The maximum value in Helander's work is $17.67\,\text{ppma}$, while in this study, values as high as $24.72\,\text{ppma}$ are found. The highest resistivity for the extensive study is measured to be $11.8\,\Omega\text{cm}$, but in this study, a maximum value is found to be $3.07\,\Omega\text{cm}$. The higher DRL signals in Helander's work may be due to other processing steps of the samples, and other impurities incorporated in the samples. It would be natural to assume that the DRL signals are lower for the samples containing less oxygen because fewer impurities are incorporated in the silicon material. It is thus concluded that the samples used in Helander's study are different regarding other properties, which may have enhanced the DRL signals.

The BB signal is enhanced for both crystals at TD-free condition, see Figs. 6.2 and 6.3. At TD-free condition, the oxygen clusters become even bigger, and the connection made with the silicon atoms in the lattice is decreased. This leads to more silicon atoms available to form covalent bonds, and the BB signal intensity is therefore increased for all the samples. This corresponds well with the findings of Antonova et al. [1], where oxygen often out-diffuse from their centers, leading to even larger clusters of oxygen in the silicon lattice.

Crystal B in Fig. 6.3 has a larger difference between the BB signal than the difference between the DRL signals, comparing TD-dominated and TD-free condition. This may be due to the fact that the laser is more sensitive or better calibrated for the longer wavelengths than the BB range. The laser may thereby absorb the DRL signals better than the BB signal. Crystal A in Fig. 6.2 contain fewer differences in BB signal when comparing the TD-dominated to the

TD-free condition. The DRL signals have a larger difference in Fig. 6.2, but not as high as for crystal B in Fig. 6.3. This may be explained by the lower pull rate of crystal A, thereby more contaminated material.

Block A1 has the highest value of P-line signal throughout the processing steps. The recombination rate is proportional to the number of empty traps in the bandgap of silicon, and the concentration of electrons in the conduction band, found by Shockley et al. in 1958 [47]. Therefore, the DRL signals are visibly higher in block A1 than the others.

The unetched samples in Figs. 6.4 and 6.5 do not show enhanced BB signal at TD-free condition, which can be due to the less clean samples surfaces. As already discussed for the unetched and TD-dominated conditions, the generally low BB PL signal for unetched samples may be due to a high level of surface recombination and scattering at the surface by the laser, as they have a rugged surface compared to the etched samples. In contrast to Helander's results [22], it was found in this study that the BB signal decreases as a response to the annealing at $450\,°C$. One may assume that the decrease of the BB signal is expected since the increase in DRL signals normally decreases the lifetime of the minority charge carriers.

At TD-free condition for etched samples in Fig. 6.2 have a maximum peak value for DRL range at $0.767\,eV$. For the unetched samples in Fig. 6.4, the P-line peak at $0.767\,eV$ is shifted to higher energy value at $0.789\,eV$, called the C-line in extensive studies [38], [27]. The shift of the emission band for unetched samples may probably be due to the attribution of temperature to the silicon material, but the reason for the difference between etched and unetched samples cannot be concluded based on these results.

### 6.1.1 Summarizing discussion of section results

The spectral response of PL intensity as a function of photon energy ranging from $0.5\,eV$ to $1.3\,eV$ does show repetitive trends. The spectral response at $295\,K$ showed weak signals for both crystals, and the DRL emission lines could not be distinguishable from each other, in contrast to the spectral response at $90\,K$. Therefore, the samples scanned at cryogenic conditions are more useful for studying the changes in DRL and BB signals during processing steps.

The heat treatment process at $450\,°C$ introduced some extra emission lines into the mean spectra, as can be seen particularly in Figs. 6.2, 6.3, 6.4 and 6.5 for $90\,K$. These are the C-line ([59], [58], [44]) and the H-line ([22], [44]). Pizzini et al. [44] obtained C- and H-line peaks after $470\,°C$ annealing, which suits well with the results from this study. They also discovered that the intensities of the C- and H-lines remain uninfluenced by the duration of the thermal annealing. It was from this concluded that choosing the annealing time would not depend on these two lines, only on $1.12\,eV$ and $0.767\,eV$ emission lines.

Short-time donor killing with annealing at $650\,°C$ resulted in enhancement of the BB signal for all the four blocks, especially for block B2. As expected, the process led to the disappearance of several DRL peaks, leaving a broad signal with peak at the C-line for unetched samples and the P-line for etched samples. The reason for this may be due to one large cluster of $SiO_2$, also found by Helander in 2018 [22]. It might be a superposition of several signals with midpoint

at 0.767 eV since the signal is broad. The exposure to high temperature leads to a nucleation in the CZ-Si material at higher recombination paths than the TD clusters. The difference in peaks after donor killing may be due to the differences in interstitial oxygen concentration, but as there has not been made new FTIR measurements of the samples after the heat treatments, this remains to be quantitatively proven.

Further, the DRL energy range $0.68\,\mathrm{eV}$ to $0.79\,\mathrm{eV}$ for TD-free samples shows the lowest PL intensity strength, whereas the BB signal takes the largest PL intensity value valid for all process steps. The short anneal of one hour may be not sufficient to eliminate all electrically active clusters of TDs. By focusing on the etched samples with the strongest PL signals, block A1 showed a clearly dominating PL intensity value in the DRL signals range. Thus, it can be assumed that the defect from which the DRL emission lines originates is present to a high extent at the crystal top. The concentration due to vacancies and interstitials decreases towards the crystal bottom. That explains the difference in DRL signals for crystals A and B. The lifetime of minority charge carriers is shown to occur at the highest level for block B2, shown by the BB signal in spectral response Fig. 6.3b. Hence, crystal B is assumed to have the highest minority charge carrier lifetime containing few defects, due to the elevated pull speed.
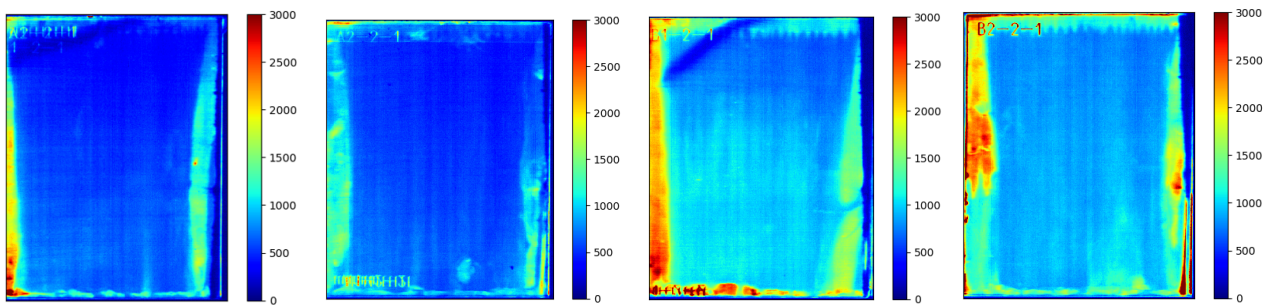
## 6.2 Spatial distribution of the band-to-band signal as a function of crystal height

The spatially distributed images taken at room temperature show weak PL signals in comparison to the PL signals at 90 K. The unetched samples have lower PL intensity values than the etched samples, see section 6.1. The etched samples are therefore better to use for the analysis of BB signal at 90 K. Thereby, the raw images for etched samples scanned at 90 K are in focus of this section, even though the images of unetched samples will be shown.

In this section, the band-to-band images taken with the HSPL camera are presented. Firstly, the as-received images are shown, which led to the decision of etching the samples a second time, called the etched condition. Secondly, the etched and unetched samples are compared with the interstitial oxygen concentration. The etched samples are subsequently compared with the resistivity values. Further, the TD-dominated after the 450 °C heat treatment for etched and unetched samples are shown. This is followed by the TD-free condition after the 650 °C condition for the etched samples. The variation in crystal height can clearly be seen in the spatially integrated images. Next, two PL detectors are compared for images taken at room temperature. Lastly, the general trends of the BB signal varying as a function of crystal height are summarized. The numerical differences in color bars to the right of the images is done on purpose to enhance the differences in BB signal for each sample.

### 6.2.1 As-received condition

In Figure 6.6, the one-time etched samples scanned at 90 K can be seen. The BB signal is distributed as a frame pattern around the whole sample. Since extensive studies do not contain the same spatial distribution of the 1.12 eV signal, it is concluded that the signals captured by the camera are due to the etching process.



(a) Block A1.      (b) Block A2.      (c) Block B1.      (d) Block B2.

Figure 6.6: As-received condition: Spatial distribution of the band-to-band signal.

## 6.2.2 Etched/unetched condition compared with the oxygen level

In Figs. 6.7 and 6.8, the spatial distribution of BB signal for the etched and unetched samples is shown. The integration range of the BB signal for plotting the spatially distributed images is 1.08 eV to 1.15 eV. The interstitial oxygen concentration is placed to the left of the respective spatially integrated image. $[O_i]$ measurements are taken 10 mm, 20 mm and 90 mm from the crystal center of A. For crystal B, oxygen measurements are done 10 mm and 90 mm from the crystal center. Moreover, images from crystal A with pull speed 0.9 mm/min are placed to the left of images from crystal B with pull speed 1.3 mm/min. The spatial distribution as a function of crystal height can be seen, as block A2 is placed beneath A1, and block B2 beneath B1. In this way, the BB signal can directly be interpreted and analyzed as a function of crystal height. The arrow to the left shows in which direction the crystal is being pulled, with the seed end on the top.
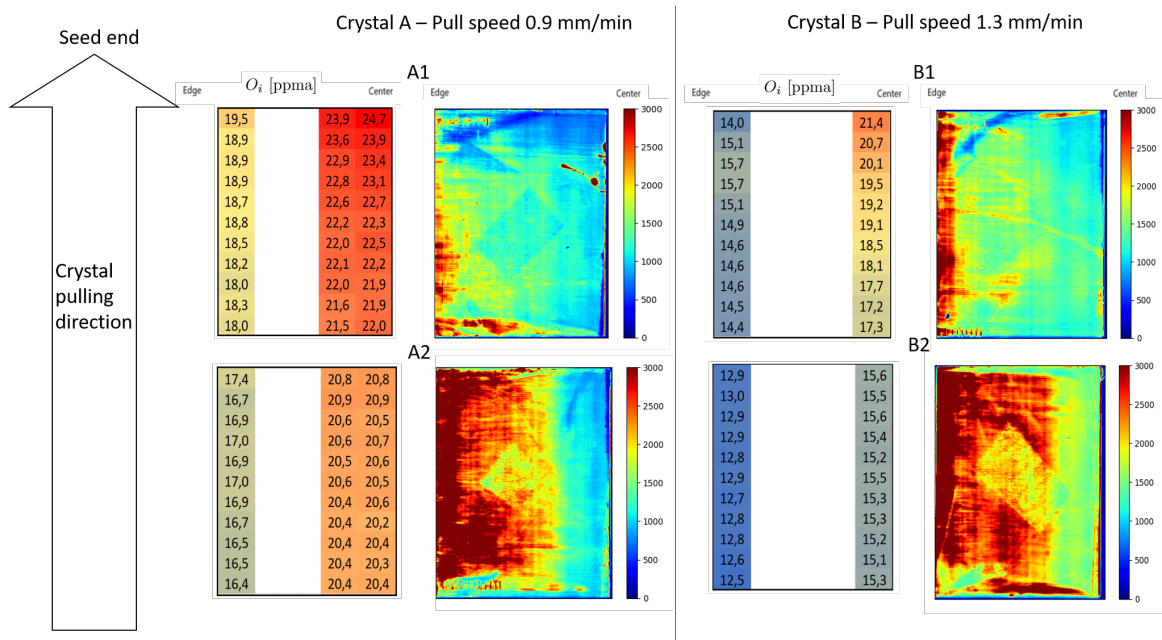


Figure 6.7: Etched condition: Spatial distribution of the band-to-band signal compared with the interstitial oxygen concentration.
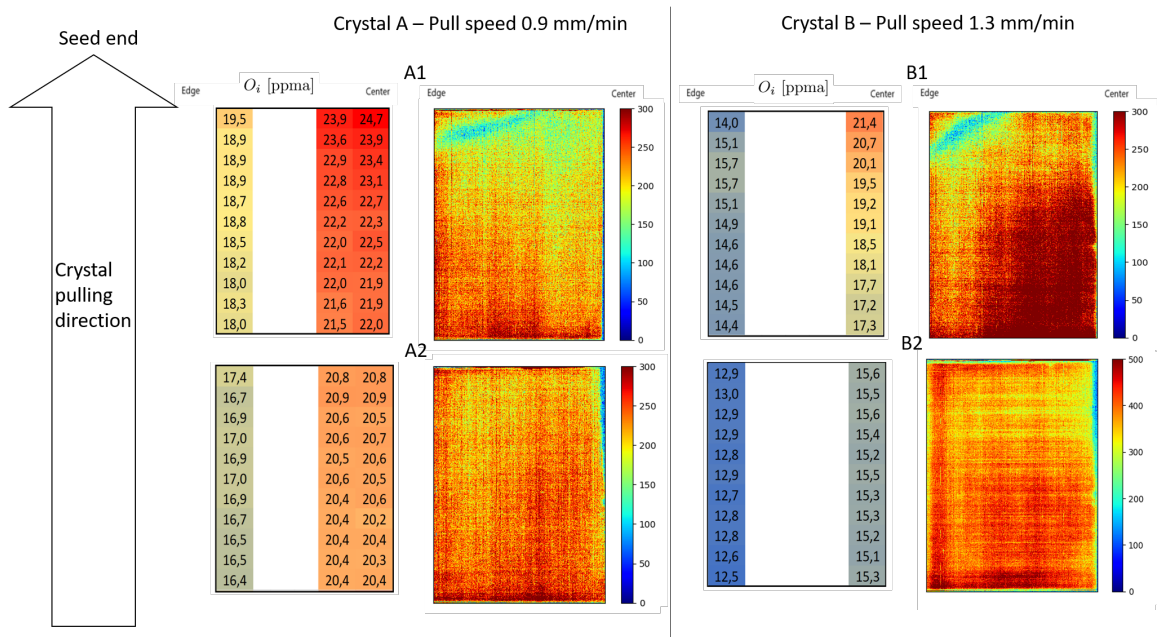
Figure 6.8: Unetched condition: Spatial distribution of the band-to-band signal compared with the interstitial oxygen concentration.

In Fig. 6.7, a rectangle has appeared in the middle of the etched samples. It may be a result of when the samples were sent between NMBU, SINTEF, and IFE. It looks like something has been lying on top of the samples, which is unfortunate for the resulting image. However, the main trends can be well understood even though the rectangular brick is present. It can thus be overseen for the analysis in focus here. The marking in the lower left corner of block A2 is due to wrongly marked sample name and can be overlooked for the analysis.

The strongest BB signal in Fig. 6.7 appears in the outer edge of the samples, indicated with the dominant red color. The BB signal for crystal B is stronger in the middle of the sample than for crystal A. This can be explained by the reduced interstitial oxygen level in crystal B, resulting in an overall cleaner sample. Also, at the bottom of the sample, there is a strong BB signal. This may be explained by the lowered oxygen concentration towards the tail end.

Stated by Søndenå et al. [51] in 2013, it could be assumed that increasing pull speed creates more vacancies in the silicon material. Moreover, the vacancies and self-interstitials created during cooling of the finished-made crystal, play an important role in enhancing the DRL signals. In this study, crystal B with the highest pulling speed at 1.3 mm/min, contain fewer excess interstitial oxygen atoms. Thereby, the DRL signals are not enhanced for crystal B, see section 6.1. The vacancies are not quantified in this study, so it could be assumed based on the study of Søndenå et al. [51], that there are more vacancies in crystal B than in crystal A. This is due to the lowered oxygen level, leaving more vacancies without being filled with atoms in the silicon lattice. If crystal B contains the most vacancies, they may not be luminescence

detectable defects. The other hypothesis may be that there are not most vacancies in crystal B.

In Fig. 6.8 for the unetched samples, the BB signal is more evenly distributed over the whole sample. The reason why the BB signal is weak and equal across the unetched samples could be due to surface recombination. The saw damage is almost not visible for the unetched samples, which means that the laser in the HSPL imaging setup does not catch the distinct BB signal.

### 6.2.3 Etched condition compared with the resistivity values

In Fig. 6.9, the spatial distribution of the BB signal for the etched samples is shown. The resistivity values are placed to the left of the respective spatially integrated image. Resistivity measurements are taken from wafers cut between the vertical cross-sections, see chapter 4. Hence, there are resistivity measurements in the top and bottom of every block. There are three measurements from each wafer, from the center and towards the edge.
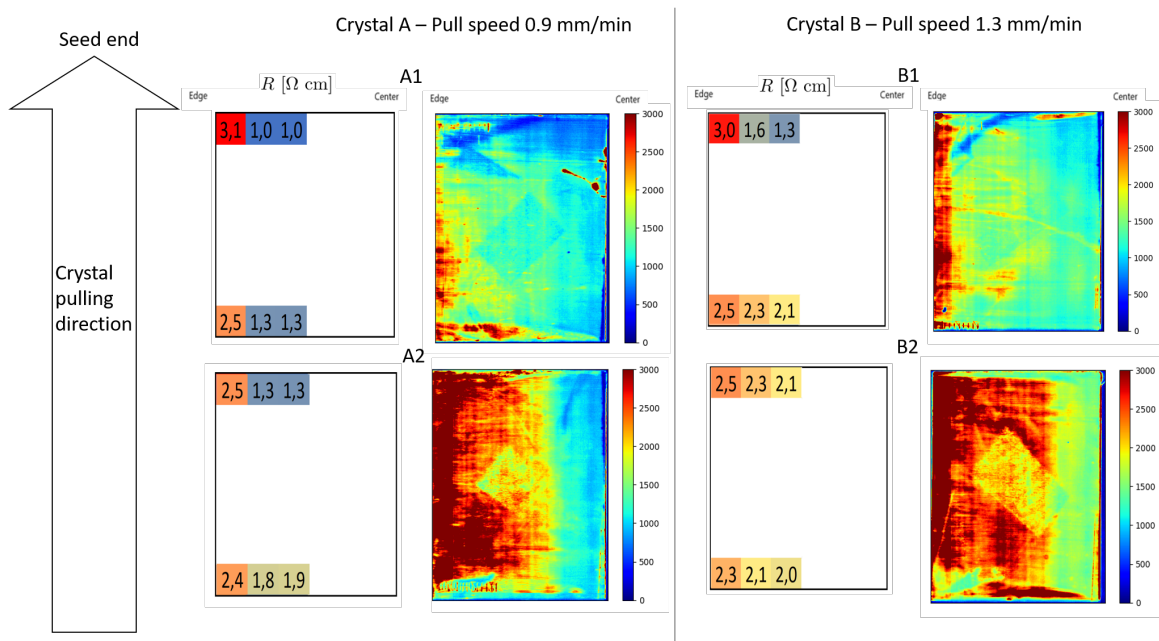


Figure 6.9: Etched condition: Spatial distribution of the band-to-band signal compared with the resistivity values.

Based on all four blocks, block A1 have the highest resistivity value at $3.1\,\Omega$cm, and the lowest value further towards the center of the crystal at $1.0\,\Omega$cm. This can be related to the big difference in $[O_i]$ for this sample. The same difference can be found in block B1, for the same reasons as for block A1.

Block A2 and B2 have the highest intensity of the BB signal, which is expected from the high resistivity, hence possibly a low recombination rate. The BB signal is enhanced in the middle of the A2 and B2 samples. This correlates well with the smaller difference in resistivity from the edge towards the center of the crystal. Block A1 and B1 are found higher up in the crystal, which results in higher resistivity values at the edge. As discussed before, blocks A1 and B1 have been in touch with the quartz crucible for a longer period of time than blocks A2 and B2. A greater deal of impurities is, therefore, found in blocks A1 and B1.

### 6.2.4   Thermal donor-dominated condition

In Figs. 6.10 and 6.11, the BB signals for TD-dominated etched and unetched samples are shown, respectively.
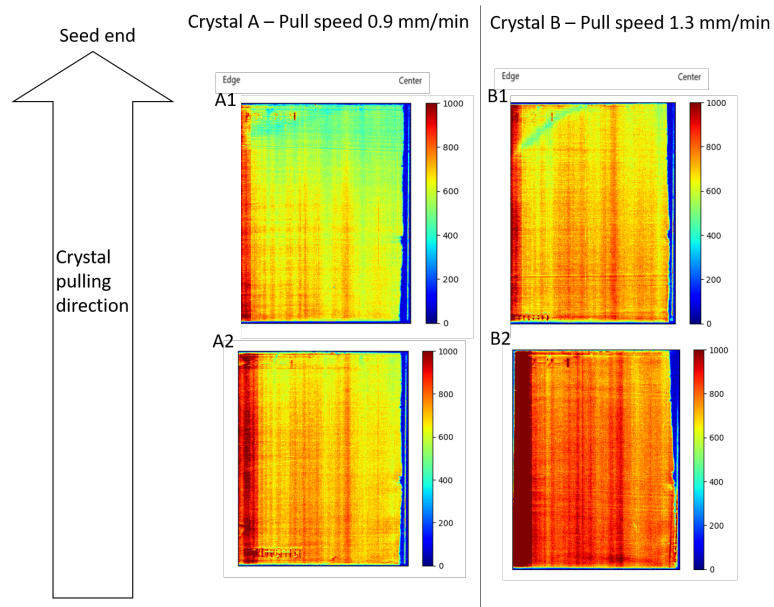


Figure 6.10: Etched TD-dominated condition: Spatial distribution of the band-to-band signal.
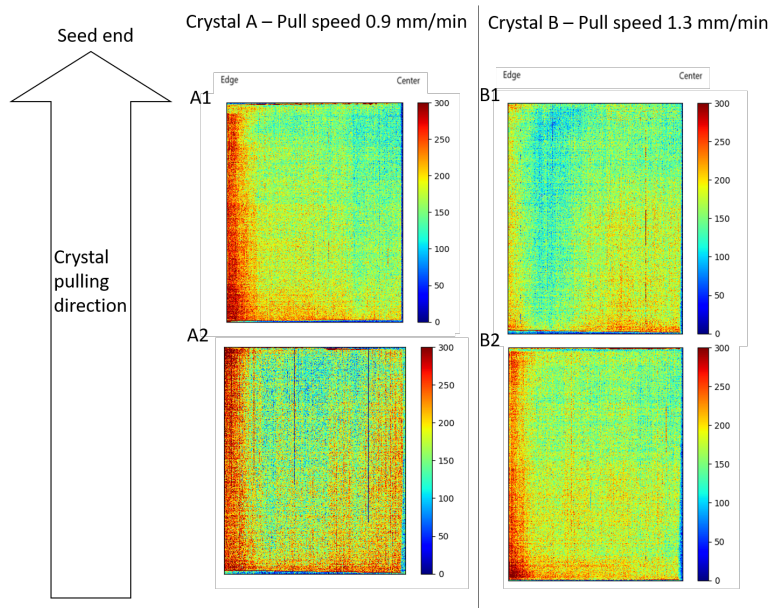
Figure 6.11: Unetched TD-dominated condition: Spatial distribution of the band-to-band signal.

The same trends for etched and unetched samples are found, but the unetched samples have such low BB signals, thereby difficult to state some characteristics only based on these samples. Therefore, the etched samples are in focus of the analysis. After 450 °C annealing, the BB signal is more evenly distributed on the etched samples. Crystal A is more affected by radiative recombination through traps near the surface, causing the BB signal to be reduced across the whole sample. The largest BB signal is found in the outer edge of all four samples shown in Fig. 6.10.

Since all samples are exposed to the same heat treatment for the same period of time, the oxygen atoms in the interstitial positions have probably reacted in the same way in the two crystals when going through the heat treatment. The difference in oxygen level is probably still there given the higher BB signal for block B2.

Across the height of crystal B, the BB signal increases with the distance from the seed end. Accordingly, Nakanishi et al. [39] showed in 1983 that by cooling a crystal faster will lead to less supersaturated oxygen precipitates after heat treatment. The top of the crystal will rest in the cold zone of the CZ process during a shorter time of period. Crystal B, with a higher pull rate, stays in the cold zone for a shorter time than crystal A. Block B2 is therefore assumed to be the cleanest sample of all four.

Block A1 showed highest BB signal values towards the bottom and edge, whereas block B2 had the highest values at the top, although retaining small variations across the height of crystal. When the material is being annealed, the vacancies react with the interstitial oxygen and other defects in the material. This leads to larger defects than usual. It has been stated

already that the chemical compounds added unintentionally into the crystal growth do not have a uniform distribution within the crystal ([13], [31]), in contrast to the doping which melts with the silica in the crucible. This is probably why the differences between the spatially distributed images between the crystals differ to a large extent.

### 6.2.5 Thermal donor-free condition

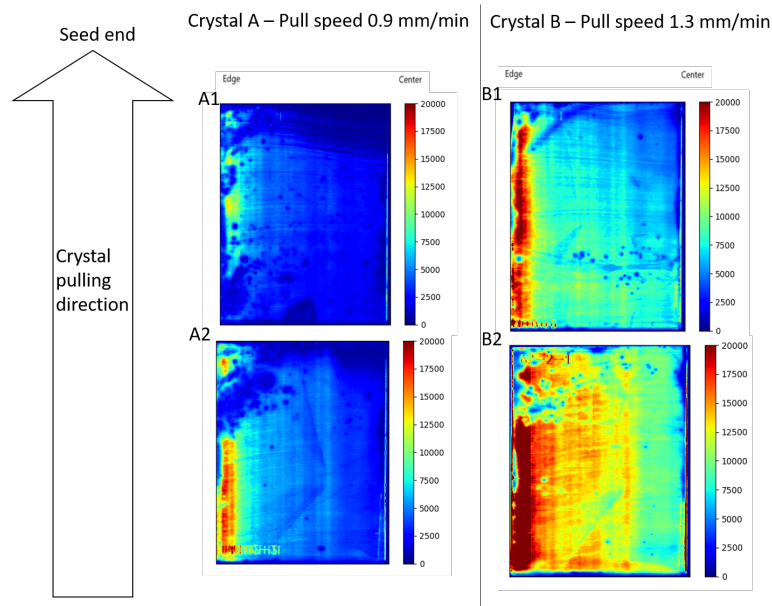Fig. 6.12 shows the spatial distribution of the BB signal for etched TD-free samples scanned at 90 K.



Figure 6.12: TD-free condition: Spatial distribution of the 0.767 eV signal.

After 650 °C annealing at TD-free condition, the BB signal is enhanced for the etched samples. The distribution of the BB signal in Fig. 6.12 looks like the before annealed samples in Fig. 6.9. However, the color bar to the right of every image goes up to 20 000. This makes sense because the interstitial oxygen should, in theory, agglomerate to larger clusters after the donor killing process. When the temperature exceeds 650 °C, the oxygen clusters may be too big to donate electrons to the conduction band. This will, in turn, decrease the electrical conductivity and thereby cause the minority charge carrier lifetime to increase, in the form of an enhancement of the BB signal. The HSPL images for the unetched TD-free samples appear as noise and can be found in Appendix D.

### 6.2.6 Comparison between photoluminescence measurements for two different detectors

In Figure 6.13 and 6.14, PL images from TD-dominated and TD-free conditions are compared between two different cameras at IFE and at NMBU.
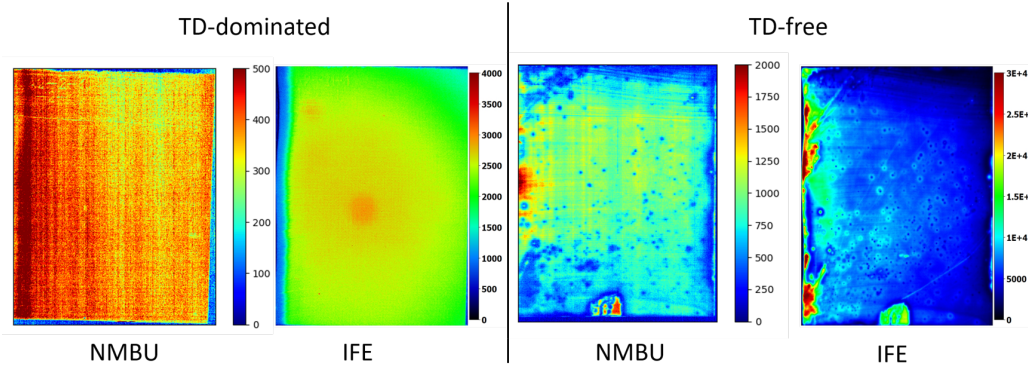


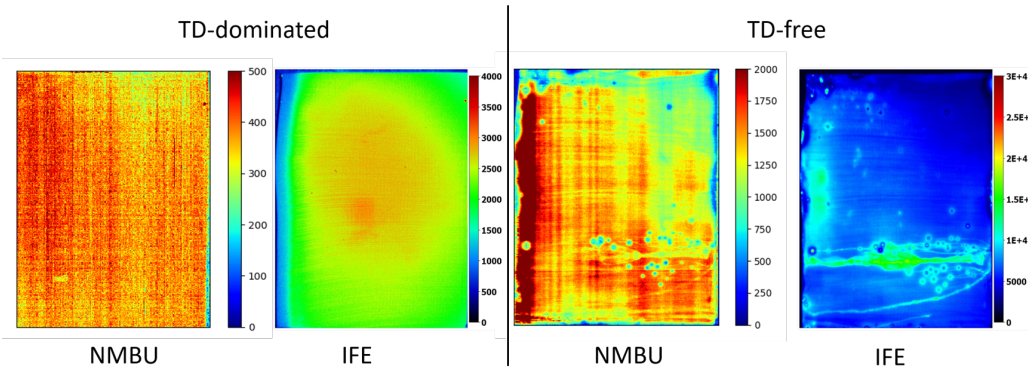Figure 6.13: A1 – Pull speed 0.9 mm/min.



Figure 6.14: B1 – Pull speed 1.3 mm/min.

The main reason why the images are so different is that the whole sample is illumined at the same time at IFE, while the camera at NMBU captures one line of pixels at a time. This may enhance the difference in the diffusion of charge carriers. For the camera at NMBU, there may be diffusion of charge carriers towards areas not illuminated.

The images are taken with two different detectors at IFE and at NMBU, for detailed information see chapter 4. The Si-CCD at IFE divides many light-sensitive areas, i.e. pixels, which together build up an image of the scene in interest. When a photon strikes the sample and falls in the pixel range, the photon intensity is converted into a number of electrons. The BB signal

for silicon at 1097 nm to 1118 nm may not be detected in the same way the NMBU detector captures the BB signal, due to the difference in wavelength ranges.

Further, the images are taken at room temperature 295 K. This causes the noise performance of a Si-CCD detector to increase, such as dark current (thermally generated noise). The noise can come up to thousands of electrons per pixel per second at room temperature. Hence, the best capacity of each pixel will be reached in a few seconds and from this point hereon, the CCD will be saturated. The noise can be reduced by cooling the samples down to cryogenic conditions, but this was not done when scanning the images with the Si-CCD detector. Another type of noise that can appear in the images is read-out noise. This originates from the conversion of the electrons to a voltage in the CCD output node. It applies for each pixel in the resulting image, and the noise value determines the dynamic range of the CCD detector, and should, therefore, be kept as low as possible.

In this study, the penetration depth of the laser at $12.5\,\mu m$ for room temperature has not been large in comparison to the thickness of the sample at 2.5 mm, but is believed to be at same size as the surface roughness. Sopori et al. [52] discovered in 2016 that the saw damage has a thickness of $6.5\,\mu m$, which means that there is a possibility that the detectors capture the irregularities in the surface caused by the sawing. The detector at NMBU has a higher wavelength absorption than the detector at IFE. If a sample has a rough surface, and the laser has high wavelength absorption, the surface will seem flat and the laser will scatter significantly less, as can be seen in comparison plots in Figs. 6.13 and 6.14.

The images taken at NMBU and at IFE are more similar at TD-free condition. The PL intensity is also enhanced for both cameras. However, in Fig. 6.14, the BB signal for the images taken at NMBU are reversed for the images taken at IFE. There might have been some liquid flowing down the sample because of too little drying with the $N_2$ gun after cleaning. This may cause confusion to the camera absorbing the BB signal. It will instead absorb what is left of the chemical solution, which may have other photon emission ranges.

### 6.2.7   Summarizing discussion of section results

The spatially distributed images of the band-to-band signal showed large differences for the two crystals between processing steps, such as etching and heat treatments. The crystals had BB signal variations as a function of crystal height, and from the crystal center towards the edge.

In subsection 6.2.1, the HSPL images had a frame-like pattern. It was concluded that this was a result of the first wet-chemical etching process of the samples. The second etching removed the frame pattern on the raw image, and the BB signal for the etched samples was distributed as expected; the strongest signal at the edge of crystal and lower towards the middle. The BB signal is highest for block B2, which means that this block has the highest minority charge carrier lifetime and the longest diffusion length of charge carriers.

In subsection 6.2.2, the results from the HSPL imaging of etched/unetched samples was compared to the oxygen concentration. The etched samples have large differences in BB signal for the two crystals. This is due to the fact that the pull speed of crystal differs and, thereby,

the oxygen atoms are probably not aligned the same way in both crystals. When the crystal cools down after crystal growth, the vacancies cluster together and make voids in the lattice. Not all vacancies manage to make larger empty spaces, and this leads to some vacancies left in the silicon material, assumed to be dominated in crystal B.

The resistivity values were compared to the BB signal raw images in subsection 6.2.3. Block A1 and B1 are concluded to be the most contaminated blocks, situated closest to the seed end.

For the TD-dominated samples in subsection 6.2.4, the BB signal did not have the same variation along with the crystal height for all samples. The TD-dominated samples do not have large variations as a function of crystal height, but the strongest BB signal appeared at the edge of all samples. For block A1, the BB signal increased towards the tail end, but block B2 had the largest BB signal at the top. This may be caused by the phenomenon where the exposure to higher temperature leads to atoms moving more freely within the lattice and initiates bulk defects in different ways for the blocks.

In subsection 6.2.5, the HSPL images after donor killing at 650 °C are presented. The spatially distributed images for the BB signal range have a large PL intensity for the etched samples, while for the unetched samples, the BB signal appears as noise (see Appendix D). The unetched samples are influenced by surface recombination due to interruption of the periodicity of the crystal lattice at the surface of the samples. There may have been non-radiative surface recombination from the samples which was not captured by the laser as well [17]. Though, the non-radiative recombination paths are not taken into account in this study.

The comparison between different photoluminescence detectors in subsection 6.2.6 shows the large difference between a filter wheel camera and a line scan camera. The calibration, scan temperature and sensitivity of the detector are also crucial parameters. This makes the measurements difficult to compare. The PL imaging should have been performed a third and fourth time in order to compare the two detectors properly.

# 6.3 Spatial distribution of the 0.767 eV signal as a function of crystal height

In this section, the P-line signal for etched samples at 90 K during processing steps is compared for the two crystals pulled at different velocities. The spatially distributed raw images for emission line 0.72 eV and 0.68 eV can be found in Appendix C. The distribution of the DRL signals is the same for all three signals, but the intensity values are understandably different. Therefore, this section generalizes for the spatial distribution of the whole TD range 0.68 eV to 0.79 eV.

Firstly, the etched/unetched samples are compared with the variation in interstitial oxygen content and resistivity. Secondly, vertical line scans of different sites at the samples are compared directly to the interstitial oxygen concentration. Next, the vacancy-interstitial P-band is investigated by a horizontal line scan through the denuded area. Further, spatially distributed

images will be studied for the TD-dominated and the TD-free condition. A summarizing discussion part is made at the end of this section.

## 6.3.1 Etched/unetched condition compared with the oxygen level

In Figs. 6.15 and 6.16, the spatial distribution of 0.767 eV signal for etched/unetched samples is shown. The integration range of the P-line for plotting the spatially distributed images can be found in the table in Fig. 5.2. The interstitial oxygen concentration is placed to the left of the respective spatially integrated image. $[O_i]$ measurements are taken 10 mm, 20 mm and 90 mm from the crystal center of crystal A. For crystal B, oxygen measurements are done 10 mm and 90 mm from the crystal center. Moreover, images from crystal A with pull speed 0.9 mm/min are placed to the left of images from crystal B with pull speed 1.3 mm/min. The spatial distribution as a function of crystal height can directly be seen, as block A2 is placed beneath A1, and block B2 beneath B1. The arrow to the left shows in which direction the crystal is being pulled, with the seed end on the top.
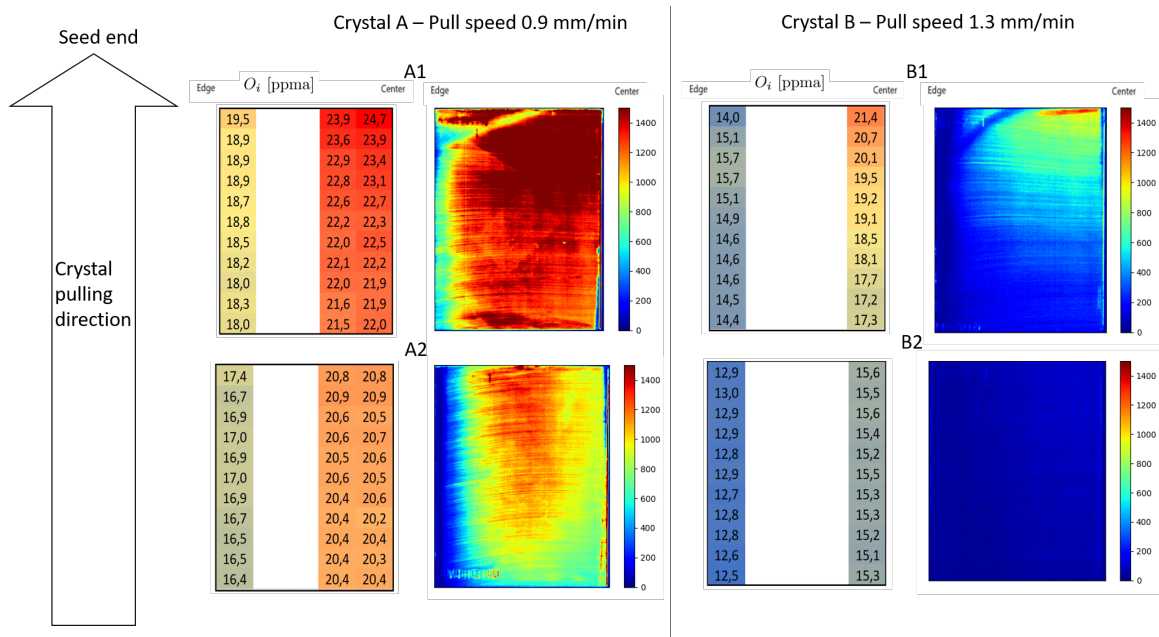


Figure 6.15: Etched condition: Spatial distribution of the 0.767 eV signal compared with the interstitial oxygen concentration.
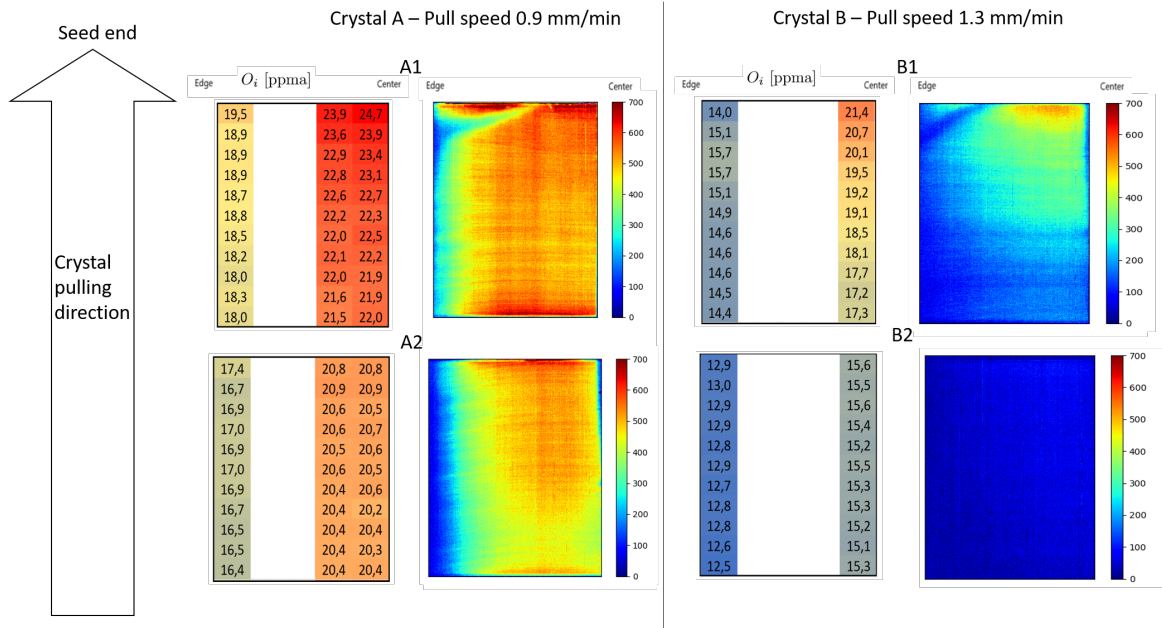
65

Figure 6.16: Unetched condition: Spatial distribution of the 0.767 eV signal compared with the interstitial oxygen concentration.

Firstly, block A1 has a strong P-line signal in the upper right corner (center of the crystal, closest to seed end), along with the highest $[O_i]$ at 23 ppma. It may be due to the SiO evaporation during crystal growth, allowing the oxygen to be mainly situated closes to the seed end [43]. It is assumed that the strong signals of block A1 also are due to the contact with quartz crucible walls, due to the tendency of prominent P-line signal. The influence of impurities mostly increases along the growth direction of a crystal due to the cold zone appearance, as stated by Kaiser et al. [26]. Accordingly, in Fig. 6.15, block A1 show a considerably stronger P-line signal than block A2. It may be proposed that $O_i$ clusters has formed TDs in the silicon material at elevated temperatures during CZ growth.

Crystal A has the lowest pull speed, resulting in the contact with the crucible walls over a longer period of time than crystal B. Further, block A2 has lower DRL signals, which makes sense according to the decreasing $[O_i]$. In order to choose the same PL intensity range for the images of A1 and B2, the spatial distribution image of B2 show almost no DRL signals. Therefore, it could be assumed that block B2 is a clean block with almost no defects. This finding accords with the study by Lin et al. [31] from 1994, who stated that when the crucible rotates, fluid flow is created in the same way as the thermal convection effect. Hence, the diffusion boundary is found to be thinner in the center than at the edge of the crystal. This results in more oxygen incorporated in the center of the crystal. Lin et al. [31] stated that sometimes, the oxygen is added intentionally to the material, as already explained in chapter 2. The interstitial oxygen can actually strengthen the physics of the bonds between atoms in the silicon lattice. Hence, additional non-luminescence detectable defects may have been avoided,

especially for block A1.

As oxygen enters the silicon melt via dissolution of the quartz, it is incorporated during crystal growth, and subsequently staying in the lattice during crystallization. When the crystal cools down, it has been shown that interstitial oxygen, self-interstitials, and vacancies diffuse into the lattice, recombine and agglomerate to form defects [13]. Thereafter, it is formed a high oxygen concentration at the top of the crystal, which respects the results of this study. Matsushita et al. [34] and Lin et al. [31] established that the thermal history of the crystal growth played an important role in defect content in the material, which can be observed in this work's results as well.

The model that relates $[O_i]$ with ratio crystal cross-section area and crucible cross-section area [31] suits well with the results of this study. In 1994, Lin et al. stated that the concentration of oxygen is not homogeneous in the silicon melt. Block A2 has values of $[O_i]=$ 20 ppma. The strongest DRL signals are found in the middle of the sample for block A2. This differs from the distribution for the other samples. A possible explanation for this surprising result can be that the oxygen level is more homogeneous as a function of the width of block A2 in comparison to the other blocks. Block A1 and B1 have the highest differences in oxygen level from the center to edge of the crystal, 5 ppma to 7 ppma, while block A2 and B2 only differs in 3 ppma from the center to edge. Therefore, the strongest DRL signals can be found in the middle of the sample. These results correspond well with a study by Braun et al. [3].

Søndenå et al. [50] reported that towards the tail end and edge of the crystal, the lifetime of silicon material is found to increase. Accordingly, the DRL signals in this work are observed to be lowest towards the edge and decreasing towards the tail end of the crystal.

Minaev et al. [37] established the connection between the P-line and TDs from oxygen. Tajima et al. [57] concluded, based on the previous study, that an oxygen concentration higher than $5 \times 10^{17} \, \text{cm}^{-3}$ generates the PL signal at 0.767 eV. In this study, oxygen concentrations from $1.6 \times 10^{17} \, \text{cm}^{-3}$ to $10.8 \times 10^{17} \, \text{cm}^{-3}$ are measured in the silicon crystals, which explains why the P-line is enhanced in all spectrum plots. As a comparison to Fig. 6.7 showing the etched images for BB signal in section 6.2, the DRL signals in Fig. 6.15 appear where BB signal is absent. The saw damage can be seen in the images as horizontal lines, which separates the differences in DRL signals from line to line.

## 6.3.2 Etched condition compared with the resistivity values

In Fig. 6.17, the spatial distribution of the BB signal for etched samples is shown. See subsection 6.2.3 for an explanation of the figure.
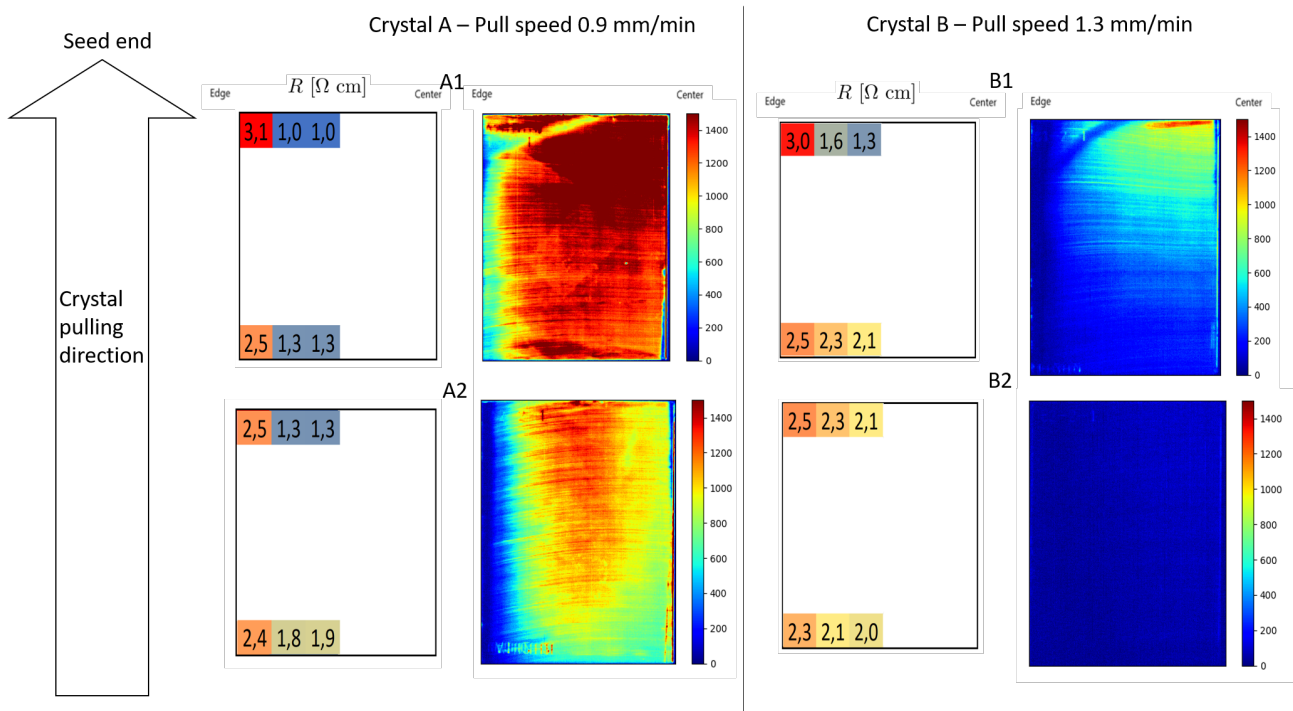


Figure 6.17: Etched condition: Spatial distribution of the 0.767 eV signal compared with the resistivity values.

As Stefani et al. [53] stated in 1988, the variations in resistivity may be due to eddy currents under crystal growth. The surface will become hotter than the bulk material, and this will decrease the conductivity at the surface. The highest resistivity values are found in the outer edge of the crystal, with decreasing values towards the center. The enhanced conductivity is a preliminary positive effect for the silicon material, but often the additional energy levels in the bandgap lead to an increased recombination rate. Block A1 has the lowest resistivity, which makes sense given the highest DRL signals.

Previous studies have mainly focused on comparing the resistivity values between processing steps such as thermal annealing, where the lowest resistivity have been found after donor generation and concluded to be due to the oxygen precipitation from the SiO clusters [7]. In this study, resistivity measurements are not done for the TD-dominated samples. Tajima et al. [55] stated that TDs distorts the known resistivity values. They did not see any 0.767 eV trap-related transition emission lines before thermal annealing, whereas, in this study, the DRL signals were present in etched samples as well. This can be due to the temperature in which the

HSPL images are taken. Therefore, the resistivity distribution across the samples is assumed to be the same for etched and TD-dominated condition. The DRL signals are only enhanced after TD generation, but not distorted like Tajima et al. stated in 1990.

### 6.3.3 Vacancy-interstitial dominated transition

In Fig. 6.18, a horizontal line scan of the denuded gap appearing in blocks A1 and B1 are shown. To the left, the black line in the spatially integrated image shows which area is chosen for the horizontal line scan. To the right, the horizontal line scans of the P-line signal for blocks A1 and B1 are shown for the denuded area 50 mm to 90 mm from the crystal center.
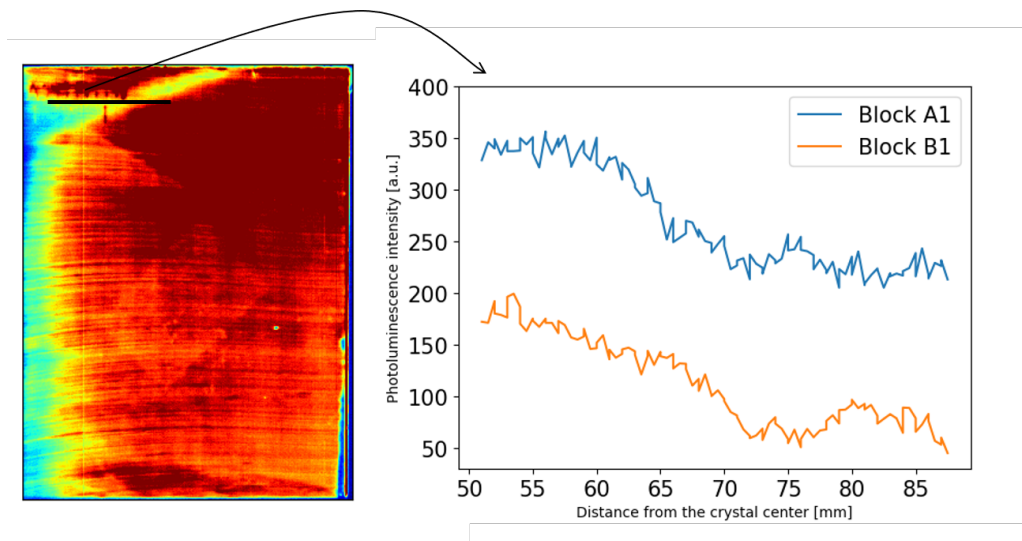


Figure 6.18: The radial distribution of the denuded vacancy-interstitial dominated transition.

There is a clear decreasing curve both for block A1 and block B1 towards the edge of the crystal. The PL intensity is low, which means that the area chosen is clean, and contain few impurities. Voronkov et al. [66] [67] described a spatial transition called the P-band (must not be confused with the P-line). The transition goes between vacancy ($V$) and self-interstitial ($I$) dominating area ($V/I$ boundary), which leads to a cleaner zone solely in the transition zone. Only the area closest to the seed end is dominated by vacancies, the rest of the crystal is assumed to be interstitial-dominated. The $V/I$ boundary results in a low defect concentration because the atoms in that area lack the ability to produce detectable agglomerates of impurity atoms in the silicon lattice. The P-band is left as a denuded transition area, with a little amount of interstitials and vacancies. The findings of Voronkov et al. suits well with the present results.

Fujimori [18] explained in 1997 that the oxygen in the denuded zone is not dependent on annealing temperature, which demonstrates the important impact on the silicon material from oxygen. In this area, the supersaturation due to out-diffusion of oxygen is small, whereas the

oxygen precipitates in bulk material are strongly dependent on annealing temperature [18]. This corresponds well with the present findings, where the HSPL images in the coming subsections 6.3.5 and 6.3.6 also show low-level of DRL signals in the denuded area.

## 6.3.4 Vertical line scans compared with the oxygen level

In further comparison between the two crystals pulled at different velocities, vertical line scans have been made. The plots enable the possibility of comparing the P-line signal at 0.767 eV of etched samples, directly to the FTIR measurements as a function of the crystal height. An indication of which plots represent which areas of the samples is shown in Figure 6.19.
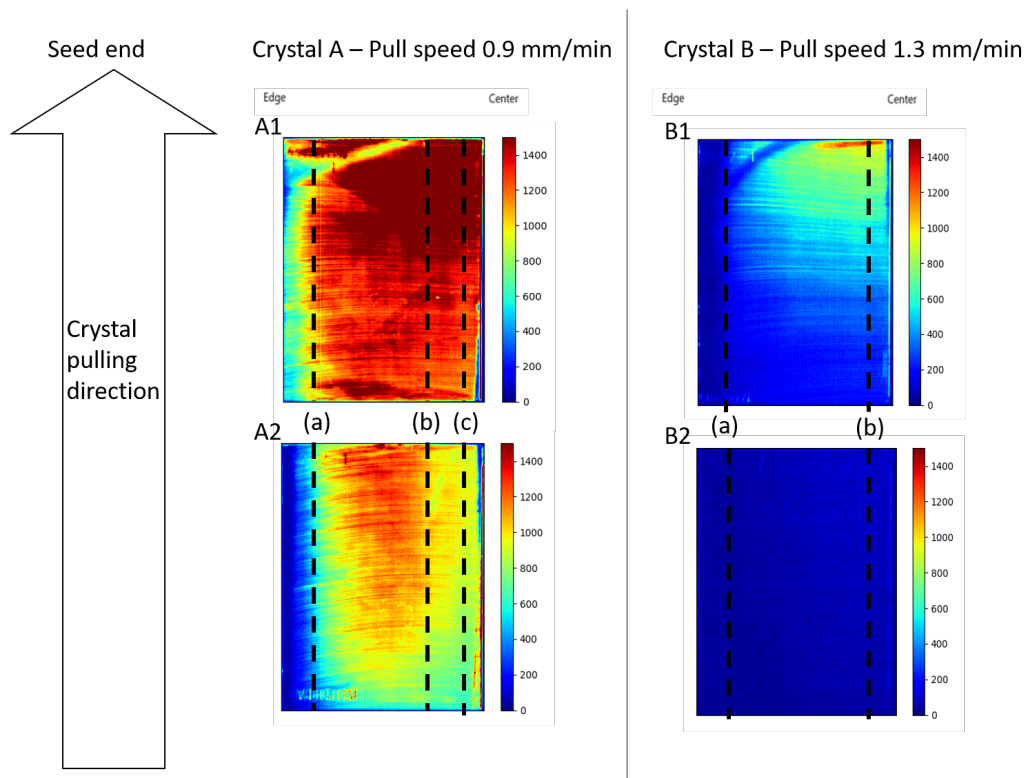


Figure 6.19: An indication of which areas of each crystal the vertical line scans represent.

Three plots from each of the blocks A1 and A2 are presented 10 mm, 20 mm and 90 mm from the crystal center, see Figs. 6.20 and 6.21. Two plots are done for the blocks B1 and B2, with oxygen measurements 10 mm and 90 mm from the crystal center, see see Figs. 6.22 and 6.23. The blue curve in Figures 6.20, 6.21, 6.22 and 6.23 represent the oxygen concentration [ppma], while the green curve represent the P-line at 0.767 eV. The FTIR measurements are collected from 10 mm to 110 mm along the crystal height, and the remaining values in order to get a smooth curve are found by interpolating between the FTIR values.
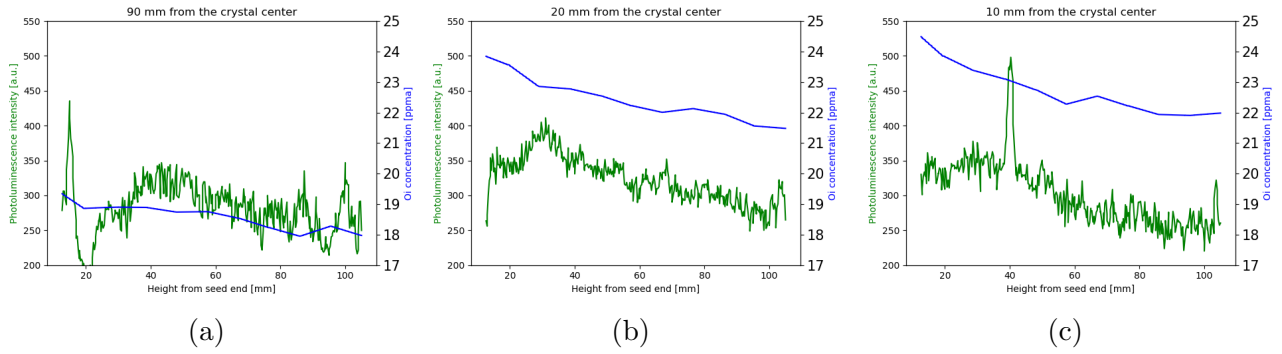
Figure 6.20: A1 – Pull speed 0.9 mm/min.

In Fig. 6.20, the trend with decreasing DRL signals and the $[O_i]$ is found in all three plots for block A1. The outer edges of the samples show some noise signals, which can be disregarded for the present study. In Fig. 6.20c, there is a noise signal in the middle of the sample, which also can be disregarded. The $[O_i]$ and P-line signal is largest closest to the seed end, and closest to the crystal center. Accordingly, Niewelt et al. [40] have shown that the defects created by interstitial oxygen and other impurities are distributed in a swirl, circle pattern. This was confirmed by Haunschild in 2011 [21]. It can be seen from the vertical line scan as a function of crystal height for block A1 that the relation between PL intensity of the 0.767 eV emission line and the oxygen level is linearly proportional.

For block A1 from the crystal with a low pull speed, the P-line ranged from 530 a.u. to 250 a.u. from the middle to the edge of the crystal. The oxygen level ranged over the same length from 24 ppma to 18 ppma. Both the oxygen and the P-line signal decreased with the distance from the seed end, reaching, 10 mm from the crystal center, values of $[O_i]$=22 ppma and P-line intensity = 300 a.u.



Figure 6.21: A2 – Pull speed 0.9 mm/min.

In Fig. 6.21, the vertical line scan for block A2 is presented. Near the crystal center, the dominant P-line signal is found. This can be seen in Fig. 6.21c, where the largest P-line signal

71

intensity (green curve) is found. The oxygen level decreases with the increasing distance from the seed end, with a minimum value at 175 mm. Figs. 6.21b and 6.21c have almost the same oxygen values, which was not the case for block A1.

Since the oxygen level is differently distributed for block A2 compared to block A1, it is natural to observe that the P-line signal also differs from each other. Block A2 have less decrease in both oxygen level and P-line signal from the seed end. In Fig. 6.21c, the P-line signal appears to be strongest furthest away from the seed end, but as can be seen in Fig. 6.19, the detector may have detected something from the edge of the sample. This is probably due to some frost beneath the sample at cryogenic conditions. Block A2 had significantly lower values of PL signals, ranging from 700 a.u. to 180 a.u. (the noise in Fig. 6.21c neglected).

Block B1 in Fig. 6.22 shows a clear correlation between the 0.767 eV emission line and the oxygen level.
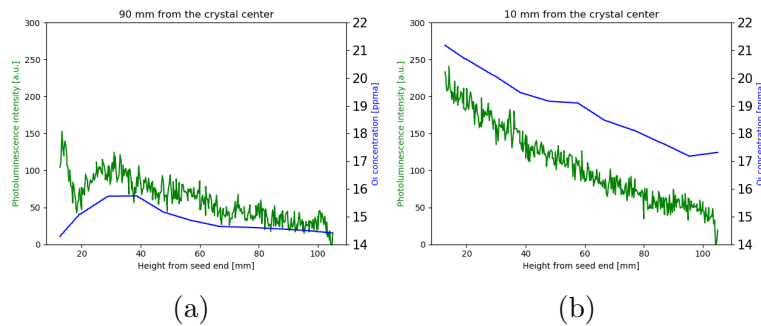


Figure 6.22: B1 – Pull speed 1.3 mm/min.

Fig. 6.22 is similar to Fig. 6.20 due to the same placement near the seed end of the crystals. Fig. 6.23 for block B2 shows the same trend as Fig. 6.21 for block A2, for same reasons discussed above.
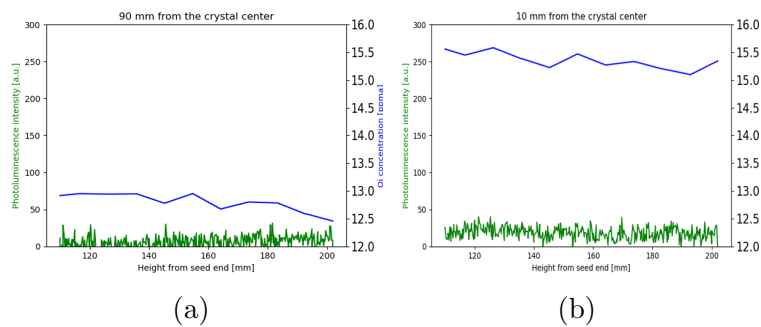


Figure 6.23: B2 – Pull speed 1.3 mm/min.

72

## 6.3.5 Thermal donor-dominated condition

In Figs. 6.24 and 6.25, the P-line signal at TD-dominated condition is shown for the two crystals A and B.
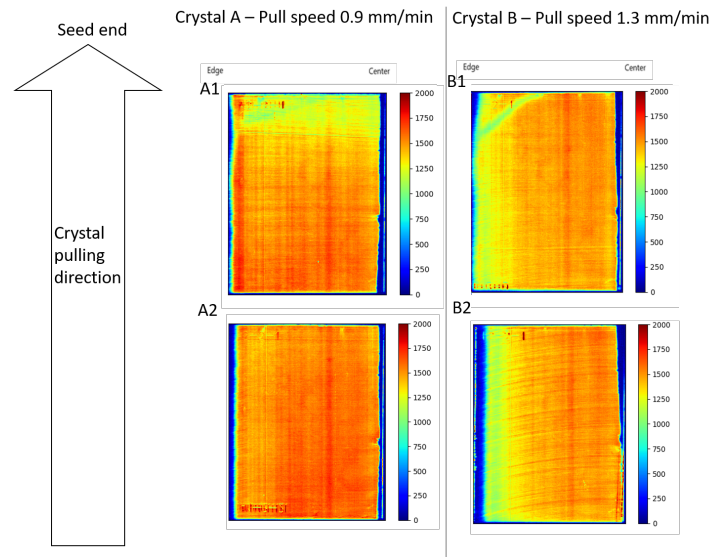


Figure 6.24: Etched TD-dominated condition: Spatial distribution of the 0.767 eV signal.
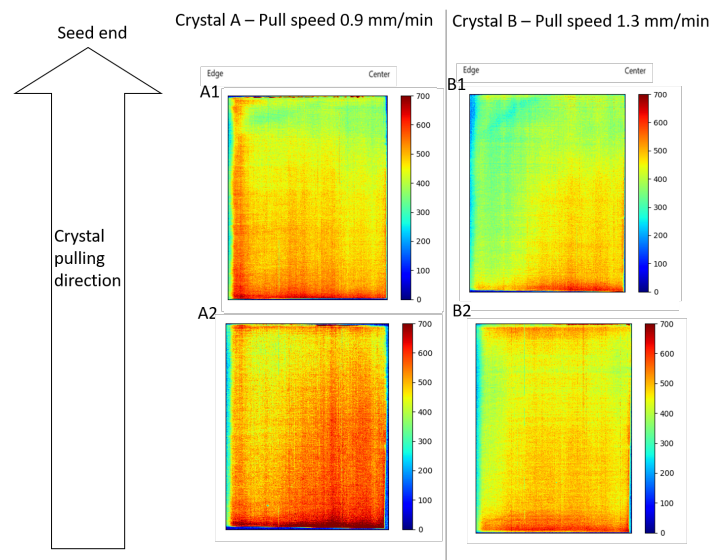


Figure 6.25: Unetched TD-dominated condition: Spatial distribution of the 0.767 eV signal.

As can be seen in the plots for the unetched samples in Fig. 6.25, the DRL emission lines

appear to dominate at the top and bottom of the sample, both for block A2 and B2. The blocks A1 and B1 have the strongest 0.767 eV signal in the bottom of the sample, which is not the case for the etched samples in crystal B.

During annealing at 450 °C, the oxygen reacts with the vacancies present in the silicon material, in addition to forming larger clusters. Maddalon-Vinante et al [33] established the relation between TDs and interstitial agglomerates, and enhancement of oxygen precipitation at thermal annealing between 400 °C to 500 °C. This suits well with the results of this study, where the P-line signal at 0.767 eV is enhanced in comparison to the etched stage. The distributed oxygen in the silicon lattice is removed to a certain extent, leaving clusters of a handful of oxygen atoms together in the interstitial positions.

It is clear that the TD-dominated images contain stronger DRL signals in crystal A than in crystal B, just as for the etched condition. This is concluded to be due to the higher pull speed of crystal B. Further, the seed end part of the crystal has higher oxygen concentration at the etched stage. This seems to have changed for the TD-dominated samples, where block A2 have stronger P-line signals than block A1, see Fig. 6.24. The oxygen distribution has clearly changed since the atoms have clustered together and formed TDs. Previous studies have not focused on the spatial distribution of PL signals related to TDs, but it may seem that the highest TD concentration appears at the bottom of the TD-dominated crystal A. For crystal B, the vertical variation in the P-line signal is not large, but this can be due to the cleaner etched samples. The distribution of the P-line signal for crystal B at TD-dominated stage reminds about the etched stage, even though the signal is more evenly distributed over blocks B1 and B2 at TD-dominated stage. The strongest signal still appears near the center of the crystal but is not enhanced towards the seed end.

The saw damage for crystal B (horizontal lines in the HSPL image) is more detectable than for crystal A. The laser may not have detected the P-line signal well enough for crystal A, which may be due to frost on top of the sample or the lack of cooling before scanning the sample.

It has been shown in extensive studies [48], [23] that TD formation also is a strong function of doping amount and -type. Detailed information about this is not given in this study. However, it can be stated that because of the n-type material where the Fermi level lies close to the CB (see subsection 2.1.3, the low conductivity is found where the material is cleanest. In a later study by Wyller [70], there were no differences between n- and p-type in DRL line emissions, only the contaminants were stated as a possible reason for the increase in recombination activity. In this study, both crystals were of n-type material, and the difference between p- and n-type cannot be made.

### 6.3.6 Thermal donor-free condition

Figure 6.26 shows the TD-free images, spatially integrated over the P-line energy range presented in Fig. 5.2.
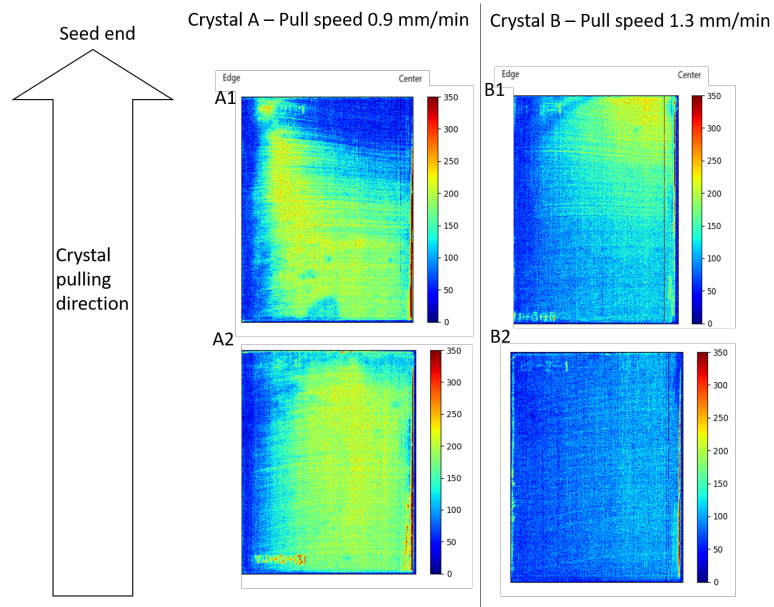


Figure 6.26: Etched TD-free condition: Spatial distribution of the 0.767 eV signal.

When performing donor killing at 650 °C, the P-line signal of TD-free samples is reduced compared to TD-dominated and etched condition. Wijarankula and Matlock [68] showed in 1990 that the thermal annealing above 600 °C eliminated most of the oxygen clusters of TDs, which can be observed in this study as well. However, they discovered new donors together with the reduction of interstitial oxygen concentration. The P-line still occurs at TD-free stage, which means that the effective recombination centers in the form of traps are still present. Block A2 contain uniformly distributed P-line signal as a function of crystal height. This is not the case for block A1, where the enhanced P-line signal is found towards the bottom of the sample. Block B1 have the strongest P-line signal where the same signal is absent for block A1. The differences in the spatial distribution of P-line is concluded to be due to the behavior of oxygen and other compounds incorporated are different depending on the initial concentration. The unetched TD-free samples can be found in Appendix D.

### 6.3.7 Summarizing discussion of section results

In this section, the results of the 0.767 eV emission line for the two crystals are shown. The differences in the spatial distribution of the processing steps for the etched cross-section samples are remarkable and interesting to study for further commercial use of mono c-Si. All the samples studied show a high degree of similarity in the distribution of PL signals. It is evident that all samples evolve in the same matter at TD-dominated and TD-free conditions. The difference between the two stages is the level of PL intensity for the various emission line signals.

In subsection 6.3.1, it was observed that even though block A2 contains less $O_i$ than block B1 closest to the upper right corner (near center of the crystal), the DRL signals are stronger. This may be explained by the lower pull speed at $0.9\,\mathrm{mm/min}$ for crystal A instead of $1.3\,\mathrm{mm/min}$ for crystal B, and that there are other chemical compounds such as iron and carbon in the crystal. Moreover, Fig. 6.15 shows that, in the samples of the present work, the impact of oxygen in-diffusion in the silicon lattice from the crucible decreases towards the crystal bottom. This means that when approaching the crystal bottom, the two blocks seem to get gradually more similar values of PL intensity, as well as the same $[O_i]$ values.

In subsection 6.3.2, it was shown that the resistivity increases with the decreasing P-line signal. By having less variation of oxygen level and resistivity in block B2, the spatially distributed image integrated over a range peaking at $0.767\,\mathrm{eV}$ shows no strong signals in comparison to the other blocks. The results from the work of Emtsev et al. [12] also showed that TDs introduce an extra energy level in the silicon bandgap and act as an electron donor to the conduction band. This leads to an increase in the conductivity, which is found here by studying the variations in resistivity values compared with interstitial oxygen content. Lipchin et al. [32] stated in 1999 that the surface of the crystal will become hotter and therefore have elevated electrical conductivity in the middle of the crystal, due to the strong dependence on temperature. This suits well with the results of this study, where it is evident that the conductivity changes through the resulting crystal, with the highest values of resistivity through the middle of the crystal.

In subsection 6.3.3, the spatial transition area of $V/I$ boundary is investigated. The largest variations of oxygen content and resistivity are found in the top block of each crystal; A1 and B1. This may be explained by the transition P-band marked in the samples in the upper left corner, where there is a clearly more clean area, stated by Voronkov et al. [66]. The less clean area of block A1 and B1 may be explained by the findings of Lin et al. [31] where the fluid flow as a result of a rotating crucible is created in the same way as the thermal convection effect. Blocks A1 and B1 have the largest span in resistivity values, concluded to be due to the P-band vacancy-oxygen dominated transition area. Block A2 and B2 are situated further down from the seed end, meaning they are cleaner. The outer edge of the samples has been found to have the highest lifetime of minority charge carriers, where the dominating BB signal is found.

In subsections 6.3.4, the vertical line scans of the P-line signal and oxygen level was shown. The vertical line scans showed that the P-line signal and the oxygen level was linearly proportional as a function of crystal height. Blocks A1 and B1 showed the closest similarities between the oxygen level and the P-line signal. This may be due to the longer time spent in the cold

zone during CZ crystal growth. The P-line signal in blocks A2 and B2 is more dominated by other defects, with unknown origin.

In subsection 6.3.5, the relation between the P-line, $[O_i]$, thermal annealing reached $450\,°C$ and TDs have been established, mainly based on present findings correlating with extensive studies [26], [19], [37], [57], [36]. Due to a high oxygen concentration in crystal A, the TD-related signals are enhanced at TD-dominated stage. However, even though crystal A has a higher oxygen concentration, it does not mean that the PL intensity is increased for the DRL energy range. Block B2 has a low P-line signal, but the amount of This depends on how the oxygen behaves and how large clusters are made interstitially in the silicon lattice.

The different peaks in the DRL area could be due to phonon replica, but given the continuous results, the energy levels are concluded to be caused by TDs with different oxygen-silicon complexes, as also proposed in work by Mehl et al. [36]. The PL intensity signal was, however, a lot weaker for these samples. Since block B2 still show a significant presence of the impurity introduced by oxygen, it confirms a clear dependency on the thermal annealing at $450\,°C$. It is thus natural to propose that the growth rate of PL intensity after thermal annealing at $450\,°C$ is caused by the interstitial oxygen forming TDs. The greatest TD-related signals appear for crystal A, with initial oxygen content at $23.45\,\mathrm{ppma}$.

In subsection 6.3.6, it was shown that the $650\,°C$ heat treatment did not eliminate the P-line. The P-line has changed the distribution as a function of crystal height for crystal A due to out-diffusion of TDs from the clusters. In crystal B, the spatial distribution of the P-line is the same as for TD-dominated. This may be caused by the higher pull speed, thereby different outcomes from crystal A. The $0.767$ eV emission line had previously been connected to TDs. It could be the case in this study as well, but the annealing for only one hour was not enough to kill the TDs. It is therefore suggested that the P-line emission could be associated with the TDs, i.e. the presence of frustrating oxygen agglomerates.

FTIR spectroscopy measurements of interstitial oxygen content, along with information about varying resistivity values and crystal pull speed, making it possible to build upon the hypothesis that interstitial oxygen and TDs show a strong relation to DRL signals $0.68$ eV to $0.79$ eV in Cz-Si material. It can, therefore, be concluded that crystal A contains more defects than crystal B overall, hence more DRL signals in the spatially integrated HSPL images. This is mainly due to high interstitial oxygen level incorporated in the silicon lattice during crystal growth. Defects will be created in the silicon lattice when in the cold zone of the CZ process. The crystal has the time to react with the quartz crucible walls, the carbon furnace, and with the feedstock of silicon. This is due to the diffusion of $O_i$, self-interstitials and the creation of vacancies, subsequently recombined and agglomerated in the silicon lattice. The analysis made here applies to the raw images. It remains to be seen in the next section whether or not the findings in this section correlates well with the multivariate image analysis results.

## 6.4  Multivariate image analysis

Multivariate Curve Resolution (MCR) is a multivariate image analysis method. It is a practical way of extracting as much information as possible from the hyperspectral images. In chapter 5, the working principle of MCR analysis was explained. The results from the method can visually be viewed by looking at the loading plot and the respective score plots. Each score plot corresponds to the loading component with the same numerical value. The loadings show visually the PL intensity at the corresponding energy state detected. The score plots show the spatial distribution of PL intensity in a sample.

### 6.4.1  Multivariate curve resolution analysis of etched samples

In Fig. 6.27, the scores and loadings from the MCR analysis are shown for CZ-Si etched samples scanned at 90 K.
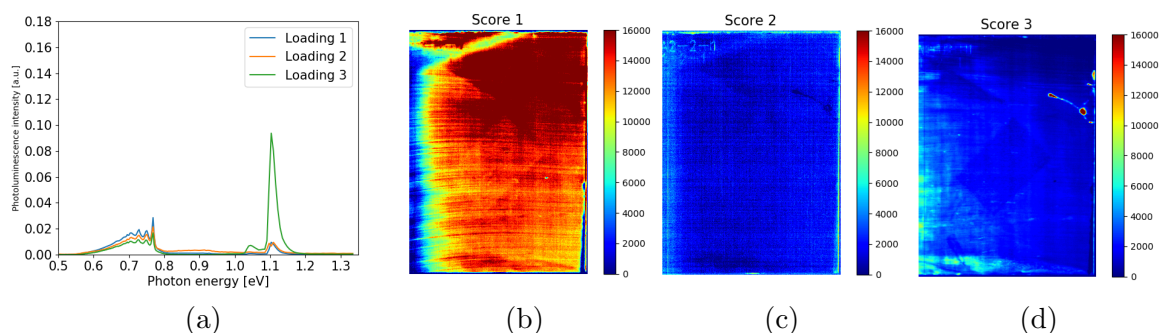


Figure 6.27: The scores and loadings from MCR analysis at 90 K with three components for a CZ-Si sample.

The challenges related to saturation in an image and to spectral overlapping signals are usually avoided by the use of MCR. The algorithm takes the spectral and the spatial dimension simultaneously into account, in contrast to raw integrated images and the pure mean spectrum. However, as can be seen in Figs. 6.27, there is some overlapping in the spectral signals. This leads to uncertainty of what the scores are showing, and the raw images in sections 6.2 and 6.3 have been concluded to be more reliable.

In Fig. 6.27, the emission lines ranging from 0.68 eV to 0.79 eV are not divided into separate loadings. Adding more components to the MCR analysis does lead to a separation of the DRL emission lines, shown in chapter 5. The MCR analysis can, therefore, be understood as somewhat non-physical, since it does not divide all the signals.

## 6.4.2 Comparison between spatially resolved images taken at 295 K and at 90 K

Fig. 6.28 shows the loadings of the MCR analysis based on three components. The CZ-Si sample are scanned at 295 K in Fig. 6.28a and at 90 K in Fig. 6.28b.
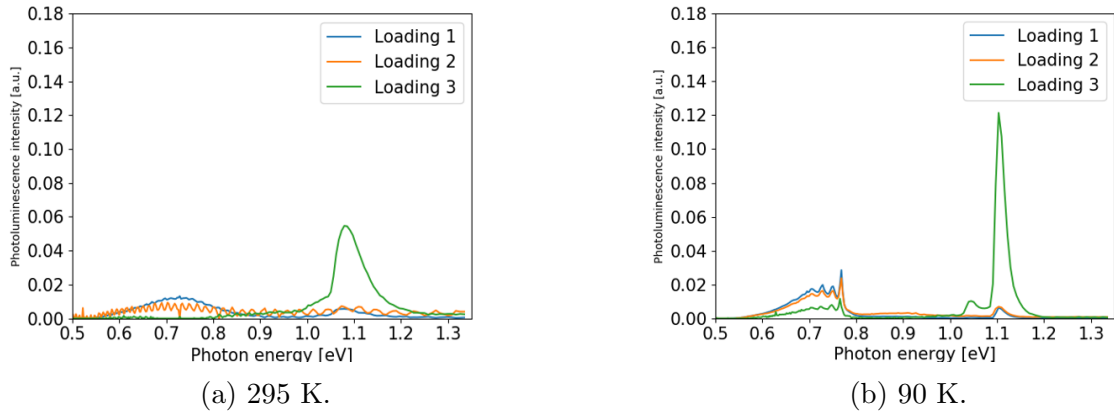


(a) 295 K.　　　　　　　　　　　　　(b) 90 K.

Figure 6.28: The loadings from MCR analysis with three components for a CZ-Si sample.

The same trends are found for the spectral response plots of raw images in section 6.1. The loadings in Fig. 6.28a for the samples scanned at room temperature clearly separates the DRL signals (loading 1), the noise (loading 2) and the BB signal (loading 3). However, all three loadings in Fig. 6.28b have peaks at emission lines between $0.68\,\text{eV}$ to $0.79\,\text{eV}$. This means that the score plots will all show DRL signals, and the MCR analysis may, therefore, be not suitable to use for the physical interpretation.

Fig. 6.29 shows the three scores corresponding to the loadings in Figure 6.28a. The plots can be understood as the DRL signals in score 1, noise in score 2, and the BB signal in score 3.
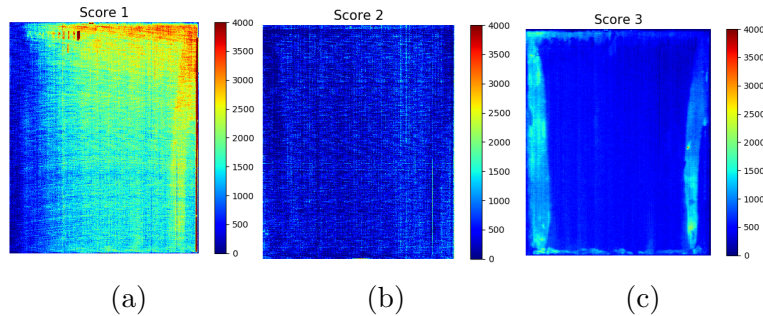


(a)　　　　　　　　　(b)　　　　　　　　　(c)

Figure 6.29: The three scores from MCR analysis with three components at $295\,\text{K}$ for a CZ-Si sample.

Fig. 6.30 shows the three scores from a CZ-Si sample scanned at 90 K, with a difference in values of the color bars. They show considerably higher signals than in Fig. 6.29 at room temperature, due to the higher penetration depth of the laser at cryogenic conditions. This can be viewed by the color bars next to the images. The distribution of the three signals found by the MCR method is, however, the same for the two temperatures.
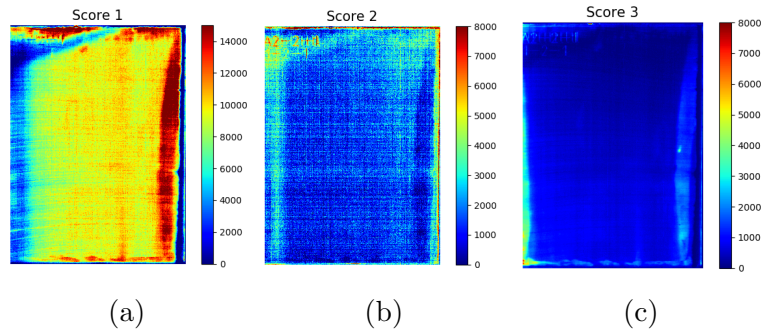


Figure 6.30: The three scores from MCR analysis with three components at 90 K for a CZ-Si sample.

The scores at 90 K all contain signals from the DRL emission line range, which means that the plots cannot be physically interpreted as the raw images. However, the plots look like the raw images presented in section 6.3, even though they cannot be directly compared.

### 6.4.3 Summarizing discussion of section results

The MCR analysis was performed to aid in separating the spectral signals, as well as confirming that there are no other distinct signals to investigate for mono c-Si cross-section samples. If there were signals overlooked when investigating the raw spectrum plots and the raw spatially integrated images, the MCR method would detect these signals. As it appears here, it looks like there are no other DRL signals to investigate. Hence, the raw images may be trusted for drawing conclusions regarding the topics in question.

## 6.5   General discussion

Characteristics and behavior of thermal donors are found based on all analyzed methods used in this work. The first method was to plot the spectral response during thermal annealing steps of the cross-section samples. The second method looked at the variation of BB and DRL signals as a function of crystal height, connected to the interstitial oxygen concentration and resistivity values. Vertical line scans were investigated for comparing the oxygen level directly to the P-line signal. Lastly, multivariate curve resolution analysis was used to support the results obtained. It has been shown through chapter 6 that the results from HSPL imaging can relate thermal annealing at $450\,^\circ\text{C}$ to interstitial oxygen and TDs. The vertical CZ-Si cross-section samples were especially interesting to study because the variation of PL signals as a function of crystal height could directly be extracted from the HSPL images.

In section 6.1, it was shown that HSPL imaging at $295\,\text{K}$ may have been a too elevated temperature to discourage activation of charge carriers out of traps in the silicon bandgap. This led to the dominant BB signal, and a weaker DRL signal. At $90\,\text{K}$, there is less phonon-electron interaction in the silicon sample, thereby causing the thermal activation of charge carriers to send out a photon at the inter-bandgap traps. There were detectable inter-bandgap PL signals due to the radiative activation of energy levels. The distinct signals for TD-dominated samples were $0.704\,\text{eV}$, $0.725\,\text{eV}$, $0.749\,\text{eV}$ and $0.767\,\text{eV}$, and emission shoulders at $0.667\,\text{eV}$, $0.685\,\text{eV}$, $0.789\,\text{eV}$ and $0.925\,\text{eV}$. After $650\,^\circ\text{C}$, the signals related to defects were considerably lower, which led to an extraordinarily high-intensity enhancement of the BB range signal for fast pulled crystal B. This may be due to the out-diffusion of TDs from the clusters, and the oxygen atoms have diffused into one large cluster of $SiO_2$. Further, the etched samples emitted a lot of stronger signals than the unetched samples. The smooth surface and a reduced amount of surface recombination for the etched samples made it easier for the line laser to absorb signals.

In section 6.2, clear trends were found between $[O_i]$ and the BB signal as a function of the crystal height. It was evident from the results that the highest oxygen level kept place closest to the seed end, and towards the middle of the cylindrical crystal, with the absence of BB signal. Crystal A with the lowest pull speed exhibited weaker BB signals, especially for TD-dominated samples. Further, the use of different PL detectors showed large differences in BB signal, which are probably due to the differences in properties of the detector and in calibration. It would, in this case, be optimal to do a third and fourth measurement in order to investigate which images to disregard.

Section 6.3 show that together with resistivity and interstitial oxygen measurements, the P-line at $0.767\,\text{eV}$ for etched samples is concluded to be due to elevated $[O_i]$. The recombination activity for etched samples due to the point defects is more important in crystal A than in crystal B, because the lifetime of crystal B is not as much limited by the defects. It may be assumed from the results of this work that the higher pull speed will result in a cleaner crystal, especially in the middle of the crystal, not too close to the edges or seed end. Based on an extensive study by Søndenå et al. [51], it may be assumed that crystal B contains more vacancies than crystal A due to the higher pull speed. However, in order to ensure this

for the present study, other crystals with varying pull speed should be taken into account. Crystal B does not generate other or stronger DRL signals than crystal A. Either the vacancies are not luminescence defects, or crystal B does not have more vacancies than crystal A. The vacancy-interstitial transition area was found in blocks A1 and B1, nearest to the seed end. The $V/I$ boundary was left as a denuded area, free of impurities, in accordance with a previous study [66]. The vertical line scans for the P-line signal and the oxygen level showed a linear proportionality between the two.

At TD-dominated stage, the distribution of P-line signal in the crystal was changed, and the P-line appeared with the same intensity in crystal A and B. It is assumed that the oxygen distribution has changed, due to mobilization and clustering of the atoms in the silicon lattice. The long donor generation annealing time of 66 h was found by Helander [22] would maximize the donor generation, and can be confirmed by this work. Pizzini et al. [44] showed that the DRL emission bands are undetectable even at long annealing time, thereby different periods of thermal annealing are not chosen to be investigated in this study. Finally, the TD-free samples showed an even bigger difference in P-line signal from near the seed end and towards the tail end. The strongest signals were found at the bottom of each sample, and block A2 contained the most DRL signals.

The presentation of MCR analysis in section 6.4 deviates from the raw images due to the lack of ability to divide the important signals from each other. After trying a different number of components, it was decided to use three components; one for BB signal, one for DRL signals, and the last for noise. Considering the MCR analysis is performed on three estimates from the images, it may lead to uncertainties of the representation of the whole image, due to inhomogeneity in the samples. Therefore, it can be stated that studying and comparing the spectra (loadings) and spatially distributed images (scores) from small regions versus the whole image is not considered to be reliable.

As a last thought, some uncertainties regarding the experimental setup is presented. The setup for the HSPL measurements in this study is calibrated by hand, causing decreased accuracy and laser uniformity over the sample. An error source of the HSPL setup is related to cooling of the samples and frost on top may affect the resulting signal for the image.

# Chapter 7

# Conclusions and outlook

This work has enabled interesting findings regarding the connection between defect-related luminescence (DRL) signals and oxygen-related thermal donors (TDs), as well as the spatial distribution of TDs as a function of crystal height. Two main conclusions can be drawn from the study of CZ-Si cross-section samples from two crystals pulled at different velocities.

The first main conclusion is that hyperspectral photoluminescence (HSPL) imaging has again been confirmed to be a qualified, fast and non-destructive method for studying DRL signals caused by radiative Shockley Read Hall recombination in silicon material [16], [22], [35], [5], [15], [4]. The second main conclusion is that a fast pull speed of 1.3 mm/min is recommended to use instead of 0.9 mm/min for CZ-Si crystals.

The HSPL method showed that the etched samples gave much higher PL intensity signals than the unetched due to their smooth surface and hence reduced recombination rate. The images taken at room temperature showed weaker signals due to the low penetration depth of the laser. Thus, the etched samples scanned at 90 K were in focus on drawing conclusions in this study. The HSPL images at etched condition showed that the DRL signals appear towards the crystal center and seed end, together with the enhanced interstitial oxygen level and the reduced resistivity values. The defects thus enhance the electrical conductivity of the silicon material but add traps in the inter-bandgap. The reason for the oxygen incorporated in the center of the crystal may be due to the thin diffusion boundary compared to the edge, and the interstitials diffuse into the lattice, recombine and agglomerate to form defects [31]. The appearance of the P-line signal at etched condition, prior to thermal annealing, indicates that the cross-section samples contained oxygen clusters of TDs from the crystal growth process.

The HSPL measurements support the hypothesis that over-coordinated oxygen in the meta-stable condition is correlated with the generation of the trap states in the silicon bandgap. Through thermal annealing at $450\,°C$ of the samples, it can be concluded that the trap states are responsible for the DRL emission lines of oxide precipitation and TDs in the electron energy range $0.68\,eV$ to $0.79\,eV$. Thermal annealing of the CZ-Si samples causes the atoms to move more freely in the lattice, which initiates bulk defects like oxygen precipitates, in accordance with [18], [26]. The main DRL emission lines detected were $0.704\,eV$, $0.725\,eV$, $0.749\,eV$ and

0.767 eV (P-line), and emission shoulders at 0.667 eV, 0.685 eV, 0.789 eV (C-line) and 0.925 eV (H-line). Mehl et al. [36] have also confirmed that the 0.72 eV-line and the P-line are related to TDs. In line with other works (e.g. [40], [22]), it has been found by HSPL imaging that the donor generation process causes the oxygen to be distributed differently in the silicon material. The TDs were uniformly distributed as a function of crystal height for TD-dominated samples, with a slight increase towards the top and bottom of the samples.

In agreement with the study by Helander [22], the heat treatment at 650 °C eliminated the TDs to a certain extent. The TD-free samples had a peak at 0.767 eV for the etched samples, and one peak at 0.789 eV for unetched samples. The presence of the DRL emission lines for TD-free samples can be concluded to be due to a too short annealing time for eliminating all donors. The remaining broadband emission is concluded to be due to oxygen diffusion into a large $SiO_2$ cluster.

As a result of HSPL imaging, a spatial transition area has been observed for samples near the seed end. By investigation through a horizontal line scan, the DRL signals have been shown to be reduced in this area. Voronkov et al. [66] named this area the P-band and defined it as the boundary between interstitial and vacancy dominated area. Accordingly, with this study, the P-band is left as a denuded area, free of impurities.

Higher crystal pull speed may increase the performance of CZ-Si material due to the lowered amount of impurities. Crystal A has the poorest quality in comparison to crystal B, due to the lower pull speed of crystal A, which resulted in elevated interstitial oxygen concentration. The enhanced $[O_i]$ in crystal A is due to the contact with the quartz crucible in the cold zone of CZ process for a longer time than crystal B, in accordance with [54], [13], [34], [31], [50], [43].

Throughout the work, the BB signal at 1.12 eV has been dominating for the oxygen-poor samples, with the highest concentration at the bottom of the sample (closest to the tail end) and towards the edge. Block B2 has got the highest BB signal, i.e. concluded to be the cleanest and have best outlooks for further use in solar cells, accordingly with Flø et al. [16].

Multivariate curve resolution (MCR) analysis confirmed that there were no signals overlooked when investigating the raw images for the CZ-Si cross-section samples. The results of the MCR algorithm deviate a bit from the raw images. Especially the spatially distributed images were unreliable, since several scores and loadings contained the same the DRL emission lines.

This study is the first attempt to use HSPL imaging for examining how vertical cross-sections could give information about TDs as a function of crystal height. The results are promising and it can be used as a method of studying CZ-Si crystals in further work.

## 7.1 Further work

For further study of the TDs related to DRL emission lines, it would be an advantage to do FTIR measurements of the interstitial oxygen and resistivity measurements after every heat treatment. It can be challenging to estimate how the oxygen behaves after heat treatment, solely based on the HSPL images. It is speculated that the FTIR measurements for TD-dominated samples will give lower $[O_i]$ values. This is because of the $O_i$ clusters together and participates in the creation of TDs. At TD-free stage, the FTIR measurements should give the same signals as the etched samples. Oxygen agglomerates should increase size after thermal annealing, but an assurance of this statement remains to be confirmed.

Further investigation about the P-line at $0.767\,\text{eV}$ and the C-line at $0.789\,\text{eV}$ would be a natural next step to take, since it is not certain why these signals appear after $650\,°\text{C}$ heat treatment. This could lead to a more accurate and quantitative analysis of how the P-line behaves and what affects the unwanted trap states in the silicon bandgap. If there were some more quantitative data regarding this, the link between TDs and the P-line could be directly made.

As already mentioned, the etched samples should be in focus for further investigation. Due to the unpassivated samples, high surface recombination has an impact on the HSPL measurements. Non-radiative recombination mechanisms could probably have an impact on the defects, but in what way and in which amount is not accounted for in this study.

It would also be interesting to study the whole crystal, not only the two blocks closest to the seed end. Moreover, by having more samples from the crystals, the results would be more reliable. Several crystals with different pull speeds could have been investigated, to falsify or support the theory about the higher pull speed results in cleaner crystals.

With more information about the doping amount in the samples, several conclusions could be drawn in relation to the study by Simoen et al [48]. Alternatively, a p-doped crystal would be interesting to look at, since previous studies have shown contradictory results regarding the differences in n- and p-type [48], [22].

Carbon is another chemical compound affecting the properties of the silicon material. It would be interesting to study the carbon level in the crystal and to compare with the oxygen level and DRL signals as a function of crystal height.

Further improvements of the HSPL method could be done regarding the cooling of the samples to $90\,\text{K}$. With enough variation in the thickness of samples and the number of experiments, an empirical equation for calculating the time it takes for a sample to be cooled off could probably be made. Further, the calibration of the laser and the setup is a time demanding process, which may be reduced if the setup was mounted on a rotating wheel. It would be possible to find the exact correct position regarding the angle towards the wall and the elevation of the setup. The camera resolution could be increased by moving the sample closer to the camera.

# Bibliography

[1] I.V. Antonova et al. "Thermal donor and oxygen precipitate formation in silicon during 450° C treatments under atmospheric and enhanced pressure". In: *Journal of the Electrochemical Society* 146.4 (1999), pp. 1575–1578.

[2] Olindo Isabella René van Swaaij Miro Zeman Arno Smets Klaus Jäger. *Solar Energy, The Physics and Engineering of Photovoltaic conversion, technologies and systems.* UiT Cambridge Ltd, 2016.

[3] Oleg M Braun and Yuri S Kivshar. *The Frenkel-Kontorova model: concepts, methods, and applications.* Springer Science & Business Media, 2013.

[4] I Burud, AS Flø, and E Olsen. "On the origin of inter band gap radiative emission in crystalline silicon". In: *AIP Advances* 2.4 (2012).

[5] Ingunn Burud et al. "Hyperspectral photoluminescence imaging of defects in solar cells". In: *AIP Advances* (2016).

[6] William D Callister, David G Rethwisch, et al. *Materials science and engineering: an introduction.* Vol. 7. John wiley & sons New York, 2007.

[7] V Cazcarra and P Zunino. "Influence of oxygen on silicon resistivity". In: *Journal of applied physics* 51.8 (1980), pp. 4206–4211.

[8] Coherent. *Lasiris Magnum II -Product sheet.* 2010.

[9] A Wallace Copeland, Otis D Black, and AB Garrett. *The Photovoltaic Effect.* Vol. 31. 1. ACS Publications, 1942, pp. 177–226.

[10] Paul Adrien Maurice Dirac. "On the theory of quantum mechanics". In: *Proceedings of the Royal Society of London. Series A, Containing Papers of a Mathematical and Physical Character* 112.762 (1926), pp. 661–677.

[11] NA Drozdov, AA Patrin, and VD Tkachev. "Recombination radiation on dislocations in silicon". In: *Jetp Lett* 23.11 (1976), pp. 597–599.

[12] VV Emtsev et al. "Stress-induced changes of thermal donor formation in heat-treated Czochralski-grown silicon". In: *Physica B: Condensed Matter* 340 (2003), pp. 769–772.

[13] Golla Eranna. *Crystal Growth and Evaluation of Silicon for VLSI and ULSI.* CRC Press, 2014.

[14] Enrico Fermi and A Zannoni. *On the quantization of the monoatomic ideal gas.* 1999.

[15] A Flø et al. "Distribution of radiative crystal imperfections through a silicon ingot". In: *Aip Advances* 3.11 (2013), p. 112120.

[16] Andreas Svarstad Flø. "Hyperspectral imaging as a tool for characterization of multicrystalline silicon wafers". PhD thesis. Norwegian University of Life Sciences, Ås, 2014.

[17] Astrid Kristine Fremme. "Hyperspectral photoluminescence scans of mc-Si wafers analysed through Multivariate Curve Resolution (MCR)". MA thesis. Norwegian University of Life Sciences, Ås, 2014.

[18] Hiroyuki Fujimori. "Dependence on morphology of oxygen precipitates upon oxygen supersaturation in Czochralski silicon crystals". In: *Journal of The Electrochemical Society* 144.9 (1997), pp. 3180–3184.

[19] CS Fuller and RA Logan. "Effect of heat treatment upon the electrical properties of silicon crystals". In: *Journal of Applied Physics* 28.12 (1957), pp. 1427–1436.

[20] Martin A Green. "Solar cells: operating principles, technology, and system applications". In: *Englewood Cliffs, NJ, Prentice-Hall, Inc., 1982. 288 p.* (1982).

[21] Jonas Haunschild et al. "Detecting efficiency-limiting defects in Czochralski-grown silicon wafers in solar cell production using photoluminescence imaging". In: *physica status solidi –Rapid Research Letters* 5.5-6 (2011), pp. 199–201.

[22] Malin Helander. "Thermal Donors in Czochralski Silicon Wafers Investigated by Spectral Imaging". MA thesis. Norwegian University of Life Sciences, 2018.

[23] V Higgs et al. "Characterization of epitaxial and oxidation-induced stacking faults in silicon: The influence of transition-metal contamination". In: *Applied physics letters* 60.11 (1992), pp. 1369–1371.

[24] Lena-Marie Jerpetjøn. "Detection of inter band gap luminiscence in multicrystalline silicon wafer". MA thesis. Norwegian University of Life Sciences, 2011.

[25] R Jones. *Early stages of oxygen precipitation in silicon.* Vol. 17. Springer Science & Business Media, 2013.

[26] W Kaiser, HL Frisch, and H Reiss. "Mechanism of the formation of donor states in heat-treated silicon". In: *Physical Review* 112.5 (1958), p. 1546.

[27] Kleverman et al. "Further evidence for the C-line pseudodonor model in irradiated Czochralski-grown silicon". eng. In: *Physical review. B, Condensed matter* 37.17 (1988). ISSN: 0163-1829.

[28] D Lausch et al. "Classification of crystal defects in multicrystalline silicon solar cells and wafer using spectrally and spatially resolved photoluminescence". In: *Journal of Applied Physics* 119.5 (2016), p. 054501.

[29] Jeremy M Lerner, Nahum Gat, and Elliot Wachman. "Approaches to spectral imaging hardware". In: *Current protocols in cytometry* 53.1 (2010), pp. 12–20.

[30] Markku Leskelä. "Rare earths in electroluminescent and field emission display phosphors". In: *Journal of alloys and Compounds* 275 (1998), pp. 702–708.

[31] Wen Lin. *The incorporation of oxygen into silicon crystals.* Vol. 42. Academic Press Inc., 1994, pp. 9–9.

[32] Aleksey Lipchin and Robert A Brown. "Comparison of three turbulence models for simulation of melt convection in Czochralski crystal growth of silicon". In: *Journal of Crystal Growth* 205.1-2 (1999), pp. 71–91.

[33] C Maddalon-Vinante, JP Vallard, and D Barbier. "Infrared study of the effect of rapid thermal annealing, thermal donor formation, and hydrogen on the precipitation of oxygen". In: *Journal of The Electrochemical Society* 142.6 (1995), pp. 2071–2076.

[34] Yoshiaki Matsushita. "Thermally induced microdefects in Czochralski-grown silicon crystals". In: *Journal of Crystal Growth* 56.2 (1982), pp. 516–525.

[35] Torbjorn Mehl. "Hyperspectral Photoluminescence Imaging of Silicon Wafers and Solar Cells". PhD thesis. Norwegian University of Life Sciences, 2018.

[36] Torbjørn Mehl et al. "Oxygen-related defects in n-type Czochralski silicon wafers studied by hyperspectral photoluminescence imaging". In: *Energy Procedia* 124 (2017), pp. 107–112.

[37] NS Minaev and AV Mudryi. "Thermally-induced defects in silicon containing oxygen and carbon". In: *physica status solidi* 68.2 (1981), pp. 561–565.

[38] AV Mudryi et al. "Impurities and defects in multicrystalline silicon for solar cells: low-temperature photoluminescence investigations". In: *Solar energy materials and solar cells* 72.1-4 (2002), pp. 503–508.

[39] Hideo Nakanishi, Hiroki Kohda, and Keigo Hoshikawa. "Influence of annealing during growth on defect formation in Czochralski silicon". In: *Journal of Crystal Growth* 61.1 (1983), pp. 80–84.

[40] T Niewelt et al. "Interstitial oxygen imaging from thermal donor growth—A fast photoluminescence based method". In: *Solar Energy Materials and Solar Cells* 131 (2014), pp. 117–123.

[41] *Nofima Data Modelling.* https://nofimamodeling.org/software-downloads/. Accessed: 2019-04-29.

[42] S Ostapenko et al. "Defect monitoring using scanning photoluminescence spectroscopy in multicrystalline silicon wafers". In: *Semiconductor science and technology* 15.8 (2000), p. 840.

[43] ZW Pan et al. "Temperature-controlled growth of silicon-based nanostructures by thermal evaporation of SiO powders". In: *The Journal of Physical Chemistry B* 105.13 (2001), pp. 2507–2514.

[44] S Pizzini et al. "The photoluminescence emission in the 0.7-0.9 eV range from oxygen precipitates, thermal donors and dislocations in silicon". In: *journal of physics: condensed matter* 12.49 (2000), p. 10131.

[45] Stefan Rein. *Lifetime spectroscopy: a method of defect characterization in silicon for photovoltaic applications.* Vol. 85. Springer Science & Business Media, 2006.

[46] R Sauer et al. "Dislocation-related photoluminescence in silicon". In: *Applied Physics A* 36.1 (1985), pp. 1–13.

[47] We Shockley and WT Read Jr. "Statistics of the recombinations of holes and electrons". In: *Physical review* 87.5 (1952), p. 835.

[48] Eddy Simoen et al. "What do we know about hydrogen-induced thermal donors in silicon?" In: *Journal of The Electrochemical Society* 156.6 (2009), H434–H442.

[49] Randall B Smith. *Introduction to hyperspectral imaging.* Vol. 30. 2006, p. 2008.

[50] Rune Søndenå, Birgit Ryningen, and Mari Juel. "Minority carrier lifetimes in Cz-Si wafers with intentional VI transitions". In: *Energy Procedia* 124 (2017), pp. 786–793.

[51] Rune Søndenå et al. "Characterization of the OSF-band structure in n-type Cz-Si using photoluminescence-imaging and visual inspection". In: *Journal of Crystal Growth* 367 (2013), pp. 68–72.

[52] Bhushan Sopori, Srinivas Devayajanam, and Prakash Basnyat. "Surface characteristics and damage distributions of diamond wire sawn wafers for silicon solar cells". In: *AIMS Materials Science* 3.2 (2016), pp. 669–685.

[53] JA Stefani et al. "Eddy current monitoring system and data reduction protocol for Czochralski silicon crystal growth". In: *Journal of crystal growth* 88.1 (1988), pp. 30–38.

[54] Kōji Sumino. *Defect control in semiconductors.* Elsevier, 2012.

[55] Michio Tajima. "Characterization of semiconductors by photoluminescence mapping at room temperature". In: *Journal of Crystal growth* 103.1-4 (1990), pp. 1–7.

[56] Michio Tajima and Yoshiaki Matsushita. "Photoluminescence related to dislocations in annealed Czochralski-grown Si crystals". In: *Japanese Journal of Applied Physics* 22.9A (1983), p. L589.

[57] Michio Tajima, P Stallhofer, and D Huber. "Deep level luminescence ralated to thermal donors in silicon". In: *Japanese Journal of Applied Physics* 22.9A (1983), p. L586.

[58] Michio Tajima et al. "Origin of room-temperature photoluminescence around C-line in electron-irradiated Si and its applicability for quantification of carbon". In: *Applied Physics Express* 11.4 (2018), p. 041301.

[59] Michio Tajima et al. "Quantification of C in Si by photoluminescence at liquid N temperature after electron irradiation". In: *Applied Physics Express* 10.4 (2017), p. 046602.

[60] HC Theuerer. "Floating Zone Method". In: *Trans. AIME* 206 (1956), p. 1316.

[61] Paul A Tipler and Gene Mosca. *Physics for scientists and engineers.* Macmillan, 2007.

[62] M Tomassini et al. "Recombination activity associated with thermal donor generation in monocrystalline silicon and effect on the conversion efficiency of heterojunction solar cells". In: *Journal of Applied Physics* 119.8 (2016), p. 084508.

[63] Paweł E Tomaszewski. "Jan Czochralski—father of the Czochralski method". In: *Journal of Crystal Growth* 236.1-3 (2002), pp. 1–4.

[64] Bart Van Zeghbroeck. *Principles of semiconductor devices.* Vol. 34. 2004.

[65] Wilfried Von Ammon et al. *Method for pulling a silicon single crystal.* US Patent 5,487,354. 1996.

[66] VV Voronkov. "Grown-in defects in silicon produced by agglomeration of vacancies and self-interstitials". In: *Journal of Crystal Growth* 310.7-9 (2008), pp. 1307–1314.

[67] VV Voronkov and R Falster. "Vacancy-type microdefect formation in Czochralski silicon". In: *Journal of Crystal Growth* 194.1 (1998), pp. 76–88.

[68] W Wijaranakula and JH Matlock. "A formation mechanism of the thermal donors related to carbon in silicon after an extended isochronal anneal". In: *Journal of The Electrochemical Society* 137.6 (1990), pp. 1964–1969.

[69] Peter Wurfel. *Physics of solar cells; from basic principles to advanced concepts.* Book News, Inc., 2010.

[70] Guro Marie Wyller et al. "Correlation of Defect Luminescence and Recombination in Multicrystalline Silicon". In: *IEEE Journal of Photovoltaics* 9.1 (2019), pp. 55–63.

# Appendices

# A  Diffusion length of minority charge carriers

The derivation of the diffusion length of minority carriers is adapted from Wurfel et al. *Physics of Solar cells* [69]. To calculate how far a particle can travel by diffusion before it annihilates by recombination, an example with electrons injected with a current density $j_e$ in a p-type material is used. Electrons are thus the minority charge carriers and assumed to be moving in the $x$-direction, since $y$- and $z$-direction are homogeneous. The charge of the injected electrons is removed when they meet a rearrangement of holes in the p-semiconductor. The steady-state distribution of the injected electrons moving in the $x$-direction is given by the continuity equation.

$$\frac{\partial n_e}{\partial t} = G_e - R_e - \text{div} j_e = 0. \tag{1}$$

The particle current density is expressed as

$$j_e = -D_e \frac{dn_e}{dx}, \tag{2}$$

$$\text{div} j_e = -D_e \frac{d^2 n_e}{dx^2}. \tag{3}$$

In the p-type material, the generation rate can be expressed as

$$G_e = G_e^0 = \frac{n_e^0}{\tau_e}. \tag{4}$$

Therefore, the recombination rate is expressed as in the following equation.

$$R_e = \frac{n_e(x)}{\tau_e} = \frac{n_e^0}{\tau_e} + \frac{\Delta n_e(x)}{\tau_e}. \tag{5}$$

From Eq. 1 it then follows that

$$-\frac{\Delta n_e(x)}{\tau_e} + D_e \frac{d^2 \Delta n_e(x)}{dx^2} = 0. \tag{6}$$

The solution of the differential equation is

$$\Delta n_e(x) = \Delta n_e(0) \exp\left(-\frac{x}{L_e}\right). \tag{7}$$

Here, $L_e$ is the diffusion length, in this case for electrons in the p-type material. Substituting Eqs. 6 and 7, an equation is obtained, like expressed in the thesis.

$$L_e = \sqrt{D_e \tau_e}. \tag{8}$$

In pure silicon, diffusion lengths normally take a value around a few millimeters for electrons.

# B  Minority charge carrier concentration in doped semi-conductors

The following derivation is adapted from Smets et al. [2]. Given the assumptions that the semiconductor is uniformly doped and in equilibrium, an equation that relates the carrier and dopant concentrations can be derived. At room temperature the dopant atoms are ionized and inside the semiconductor, and the local density is expressed as

$$\rho = q(p + N_D^+ - n - N_A^-), \tag{9}$$

where $q$ is the elementary charge given at $1.602 \times 10^{-19}$ C. $N_D^+$ and $N_A^-$ are the density of ionized donor and acceptor atoms, respectively. They express the concentration of electrons and holes due to doping, given that every ionized atom corresponds to a free electron or hole, respectively. In equilibrium, the local charge density $\rho$ is zero and the semiconductor is charge-neutral.

$$p + N_D^+ - n - N_A^- = 0. \tag{10}$$

Assuming that the thermal energy available is sufficient to ionize all the dopant atoms, the doping concentrations can be approximated as follows.

$$N_D^+ \approx N_D, \tag{11}$$

$$N_A^- \approx N_A, \tag{12}$$

and hence the charge neutrality equation can be expressed.

$$p + N_D - n - N_A = 0. \tag{13}$$

For n-type material, all acceptor atoms have vanished $N_A = 0$. Almost all donor atoms $N_D$ are ionized and donate an electron to the CB. Eq. 13 then becomes

$$p + N_D - n = 0 \tag{14}$$

Assuming that $N_D \approx n$, $p$ takes a very small value close to zero. In n-type material, the concentration of holes becomes very low when $N_D$ becomes large. Hence, $p$ can be expressed as

$$p = \frac{n_i^2}{n} \approx \frac{n_i}{N_D} \ll n. \tag{15}$$

For p-type material, the minority charge carrier concentration $n$ can be expressed as

$$n = \frac{n_i^2}{p} \approx \frac{n_i}{N_A} \ll p. \tag{16}$$

# C    Spatial distribution of 0.72 eV and 0.68 eV signals
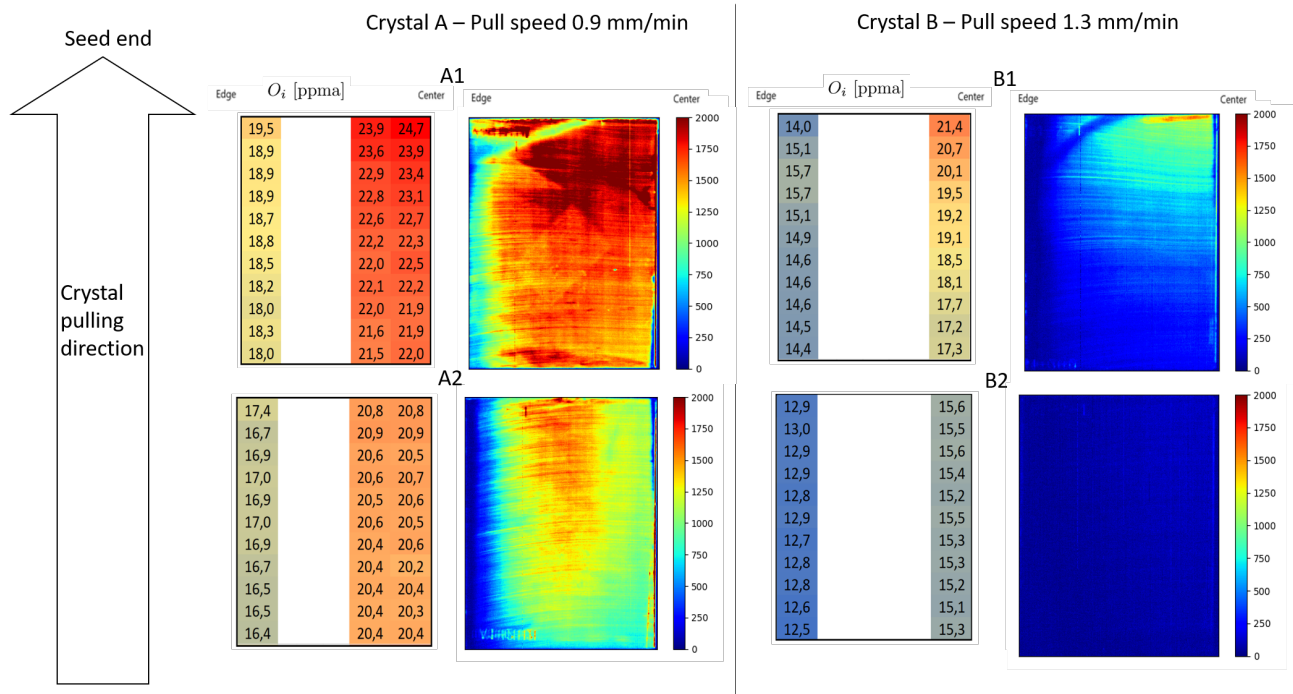
Firstly, the 0.72 eV emission line is presented.



Figure 1: Etched samples scanned at 90 K: Spatial distribution of the interstitial oxygen level and the 0.72 eV emission line.
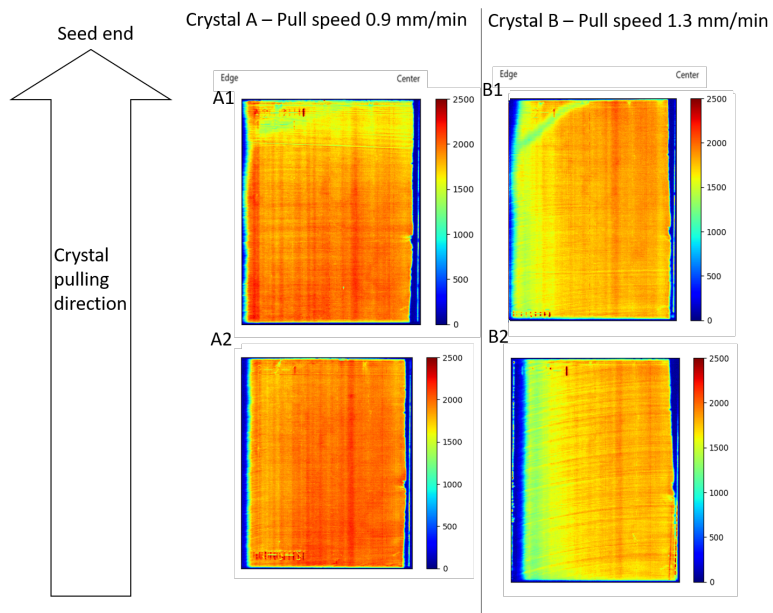
Figure 2: TD-dominated etched samples scanned at 90 K: Spatial distribution of the 0.72 eV emission line.
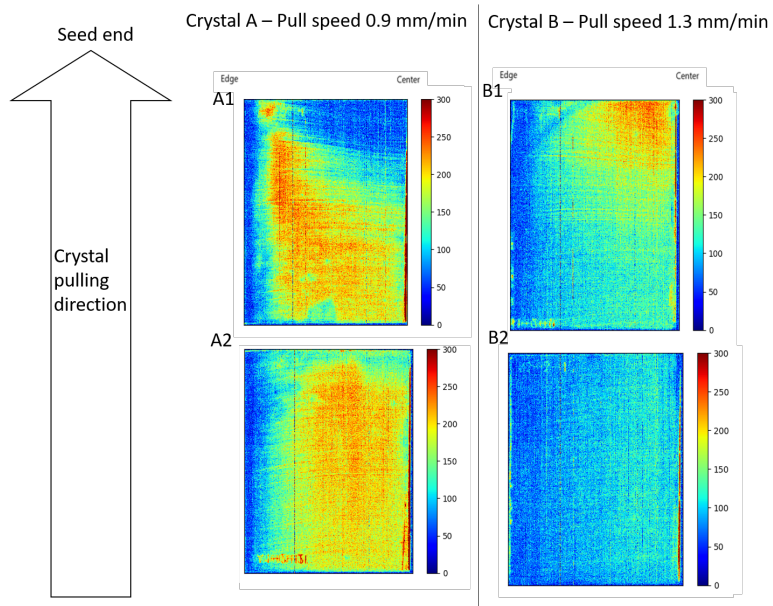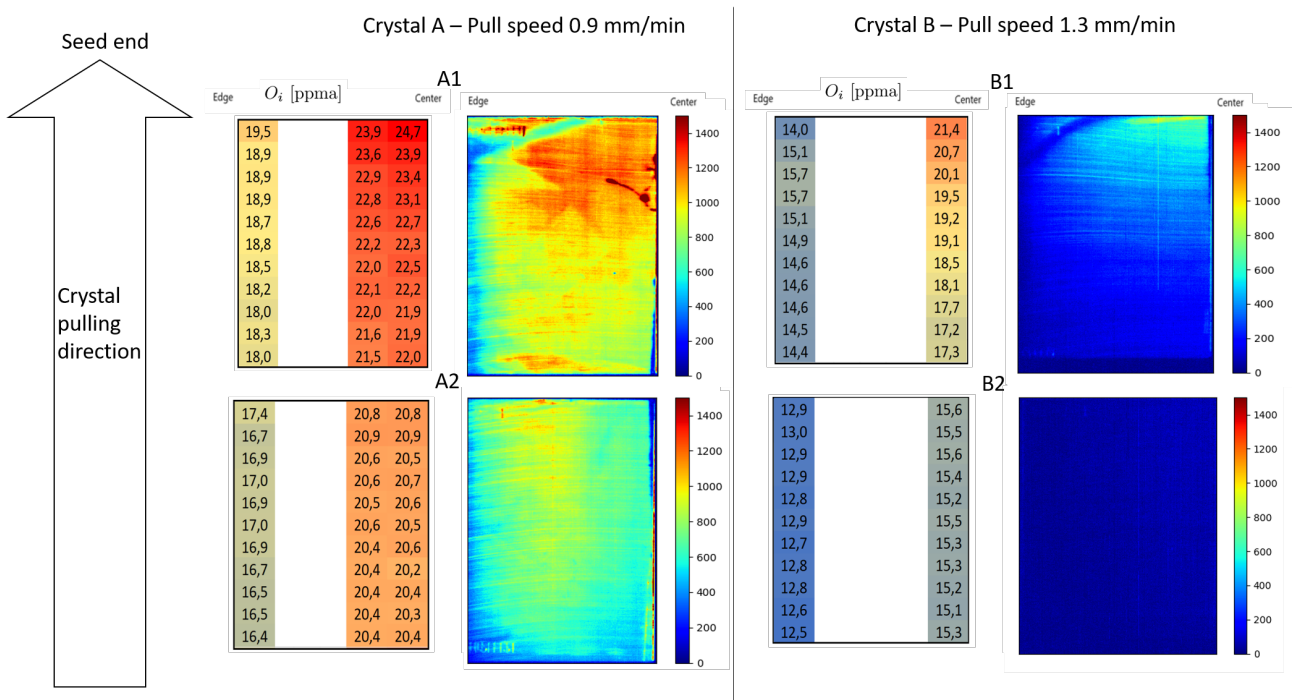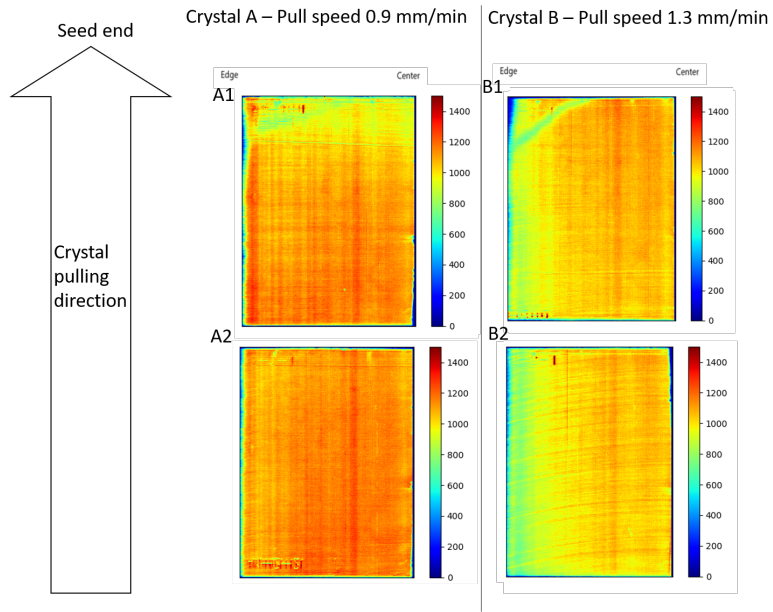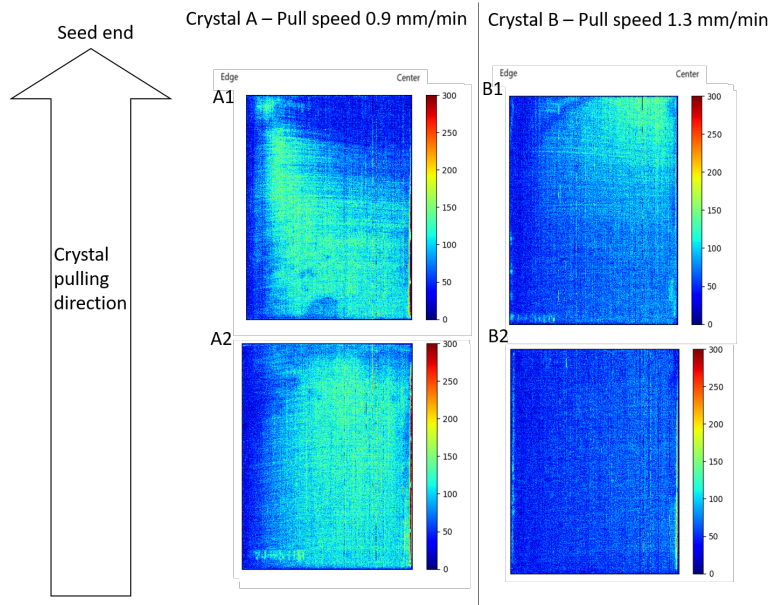


Figure 3: TD-free etched samples scanned at 90 K: Spatial distribution of the 0.72 eV emission line.

95

The 0.68 eV shoulder emission line is presented below.



Figure 4: Etched samples scanned at 90 K: Spatial distribution of the interstitial oxygen level and the 0.68 eV emission line.

Figure 5: TD-dominated etched samples scanned at 90 K: Spatial distribution of the 0.68 eV emission line.



Figure 6: TD-free etched samples scanned at 90 K: Spatial distribution of the 0.68 eV emission line.

# D   Spatial distribution of 1.12 eV and 0.767 eV signals for unetched thermal donor-free samples

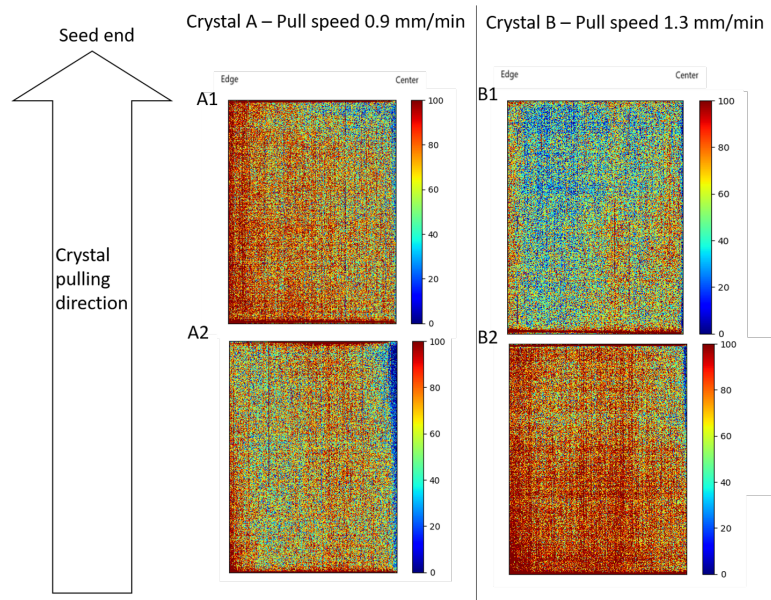The TD-free unetched samples scanned at 90 K are shown for the BB and the P-line signals.



Figure 7: TD-free unetched samples scanned at 90 K: 1.12 eV signal.
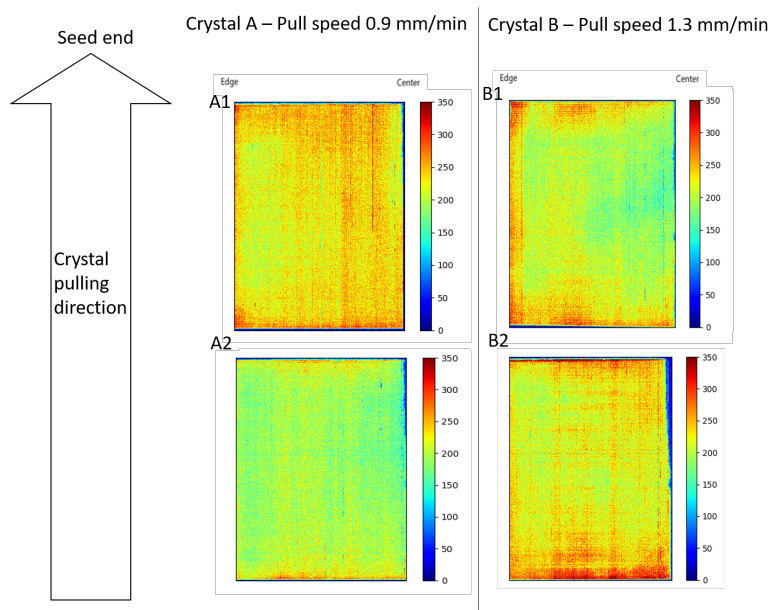
Figure 8: TD-free unetched samples scanned at 90 K: 0.767 eV signal.